

## Review

# Fundamentals, materials, and machine learning of polymer electrolyte membrane fuel cell technology

Yun Wang<sup>a,\*</sup>, Bongjin Seo<sup>a</sup>, Bowen Wang<sup>b</sup>, Nada Zamel<sup>c,\*</sup>, Kui Jiao<sup>b,\*</sup>,  
Xavier Cordobes Adroher<sup>d</sup>

<sup>a</sup> Renewable Energy Resources Laboratory (RERL), Department of Mechanical and Aerospace Engineering, The University of California, Irvine, CA 92697-3975, United States

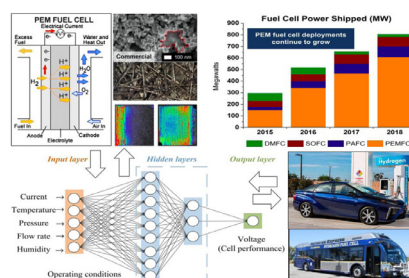
<sup>b</sup> State key Laboratory of Engines, Tianjin University, 135 Yaguan Road, Tianjin 300350, China

<sup>c</sup> Fraunhofer Institute for Solar Energy Systems ISE, Freiburg, Germany, Heidenhofstrasse 2, 79110

<sup>d</sup> General Motors Japan Ltd., Higashi-Shinagawa-ku, Tokyo, 140-8687, Japan



## GRAPHICAL ABSTRACT



## ARTICLE INFO

### Article history:

Received 15 May 2020

Received in revised form 19 June 2020

Accepted 19 June 2020

Available online 29 June 2020

### Keywords:

Pem  
Fuel cell  
Fundamental  
Material  
Machine learning  
Artificial intelligence  
Physics-informed

## ABSTRACT

Polymer electrolyte membrane (PEM) fuel cells are electrochemical devices that directly convert the chemical energy stored in fuel into electrical energy with a practical conversion efficiency as high as 65%. In the past years, significant progress has been made in PEM fuel cell commercialization. By 2019, there were over 19,000 fuel cell electric vehicles (FCEV) and 340 hydrogen refueling stations (HRF) in the U.S. (~8,000 and 44, respectively), Japan (~3,600 and 112, respectively), South Korea (~5,000 and 34, respectively), Europe (~2,500 and 140, respectively), and China (~110 and 12, respectively). Japan, South Korea, and China plan to build approximately 3,000 HRF stations by 2030. In 2019, Hyundai Nexa and Toyota Mirai accounted for approximately 63% and 32% of the total sales, with a driving range of 380 and 312 miles and a mile per gallon (MPGe) of 65 and 67, respectively. Fundamentals of PEM fuel cells play a crucial role in the technological advancement to improve fuel cell performance/durability and reduce cost. Several key aspects for fuel cell design, operational control, and material development, such as durability, electrocatalyst materials, water and thermal management, dynamic operation, and cold start, are briefly explained in this work. Machine learning and artificial intelligence (AI) have received increasing attention in material/energy development. This review also discusses their applications and potential in the development of fundamental knowledge and correlations, material selection and improvement, cell design and optimization, system control, power management, and monitoring of operation health for PEM fuel cells, along with main physics in PEM fuel cells for physics-informed machine learning. The objective of this review is three fold: (1) to present the most recent status of PEM fuel cell applications in the portable, stationary, and transportation sectors; (2) to describe the important fundamentals for the further advancement of fuel cell technology in terms of design and control optimization, cost reduction, and durability improvement; and (3) to explain machine learning, physics-informed deep learning, and AI methods and describe their significant potentials in PEM fuel cell research and development (R&D).

\* Corresponding authors.

E-mail addresses: [yunw@uci.edu](mailto:yunw@uci.edu) (Y. Wang), [nada.zamel@ise.fraunhofer.de](mailto:nada.zamel@ise.fraunhofer.de) (N. Zamel), [kjiao@tju.edu.cn](mailto:kjiao@tju.edu.cn) (K. Jiao).

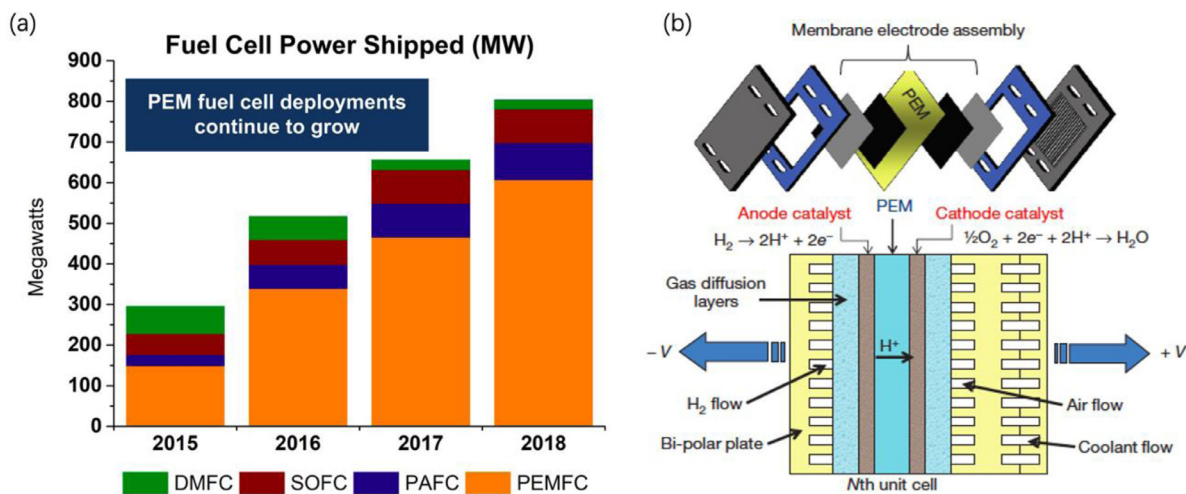


Fig. 1. (a). Fuel cell power shipped in the U.S. department of energy (DOE) report [1]; and (b) PEM fuel cell structure [2].

1. Introduction

Fuel cells, which electrochemically convert the chemical energy stored in fuels directly to electricity, are widely regarded as next-generation power devices because of their high efficiency and low emissions. Fuel cells are categorized by their electrolyte membrane into polymer electrolyte membrane (PEM) fuel cells (PEMFCs), solid oxide fuel cells (SOFCs), molten carbonate fuel cells (MCFCs), and alkaline fuel cells (AFCs).

Table 1 shows the major features and the production status as of 2019 of each type of fuel cell. Among them, PEM fuel cells operate under a low temperature, ranging from -40 to 120 °C, and are currently considered for portable, transportation, and small stationary applications. They have also received the most research and development (R&D) effort, as shown in Table 1 and Fig. 1(a).

1.1. PEM fuel cell

PEM fuel cells use polymer electrolyte membranes (notably Nafion®) to conduct protons and separate gaseous reactants on the anode and cathode sides. Fig. 1(b) depicts a schematic diagram of the PEM fuel cell structure. Such fuel cells require expensive electrocatalyst (usually platinum-based materials) to catalyze the electrochemical reactions under a low temperature. Their noteworthy features include low operating temperature, high power density, and easy scale-up, making PEM fuel cells most suitable replacements for the internal combustion engines (ICEs) of automobiles. In the transportation sector, various PEM fuel cell electric vehicles (FCEVs) have been developed, including Honda Clarity, Toyota Mirai, and Hyundai Nexa. The U.S. currently has over 8000 FCEVs and over 40 hydrogen fueling stations. The distributed PEM fuel cell power system primarily focuses on small-scale power demands

(50–250 kW for decentralized use and <10 kW for households). Backup power solutions for data centers, banks, hospitals, and telecommunication companies have received increasing attention recently because of the stringent regulations on ICE-based backup systems. For portables, PEM fuel cells can provide power to laptops, chargers, wearable electric units, and military radio/communication devices.

1.2. Current status and technical barriers

Two major barriers to the worldwide deployment of PEM fuel cells are durability and cost. In state-of-the-art fuel cells, durability decreases as loading of the costly electrocatalyst is reduced, making it challenging to meet the durability and cost targets of the U.S. department of energy (DOE) at the same time. The current price of Toyota Mirai FCEV is approximately \$60,000 even after incentives, which is higher than that of gasoline vehicles, and a fuel cell electric bus (FCEB) costs approximately \$1 M. From the viewpoint of durability, DOE testing showed that the Toyota Mirai passed the 3000 h real-world driving tests but failed largely in the DOE accelerated stress test (AST) protocols. The performance was significantly reduced after 5000 cycles with the thickness of the cathode catalyst layer (CL) decreasing from ~10 to 3 μm for 1.0–1.5 V cycle AST [11]. The lifetime target is ultimately 8000 h for FCEVs, and 25,000 h for FCEBs. From the viewpoint of cost, the current status is \$50/kW and \$45/kW for 100 and 500 thousand per year product volume, respectively. The ultimate DOE target is \$30/kW for FCEVs and the 2020 target is \$600,000 for each FCEB. In the stationary sector, Ballard commercializes backup power systems with 7000 h of operating lifetime, which falls short of the 10,000 h objective [12,13]. Moreover, data from various fuel cell developers suggest that equipment cost is ~6 times higher than the aimed \$1000/kW [12,14]. Considering micro combined heat and power (mCHP) applications, Panasonic’s

Table 1 Major types of fuel cells [3-5].

	PEMFCs	AFCs [6]	PAFCs [7]	MCFCs [8]	SOFCs [9]
Electrolyte	Polymeric membrane	Potassium hydroxide	Phosphoric acid	Molten carbonate	Ceramics
Charge carrier	H <sup>+</sup>	OH <sup>-</sup>	H <sup>+</sup>	CO <sub>3</sub> <sup>2-</sup>	O <sup>2-</sup>
Operating temperature	-40–120 °C (150–180 °C in high temp PEMFCs)	50–200 °C	150–220 °C	600–700 °C	500–1000 °C
Electrical efficiency	Up to 65–72%	Up to 70%	Up to 45%	Up to 60%	Up to 65%
Primary fuel	H <sub>2</sub> , reformed H <sub>2</sub> , methanol in direct methanol fuel cells	H <sub>2</sub> or cracked ammonia	H <sub>2</sub> or reformed H <sub>2</sub>	H <sub>2</sub> , biogas, or methane	H <sub>2</sub> , biogas, or methane
Primary applications	Portable, transportation, and small-scale stationary	Portable and stationary	Stationary	Stationary	Stationary
Shipments in 2019 [10]	934.2 MW	0 MW	106.7 MW	10.2 MW	78.1 MW

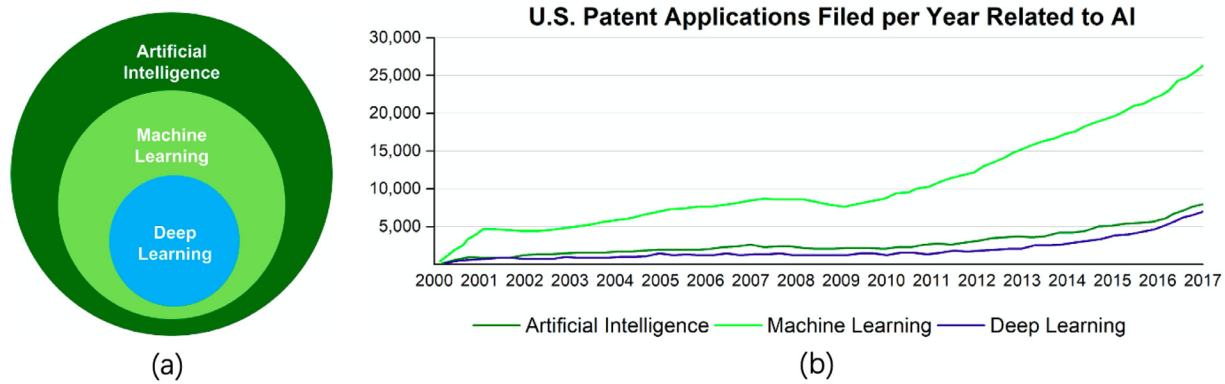


Fig. 2. (a) Relationship of AI, machine learning, and deep learning, and (b) number of US patent applications per year related to AI, machine learning, and deep learning in a U.S. DOE report [20].

highly successful 700 W units feature 90,000 h of lifetime (higher than the DOE 2020 target of 60,000 h [15]) and meet the Japanese government's intended price of JPY 800,000 [16,17]. For portables, German SFC Energy's direct methanol fuel cell (DMFC) products are warranted for up to 4500 h, whereas deployments within the sector incur a cost of up to 15\$/W [18,19]. The ultimate DOE durability and cost targets are 5000 h and 5\$/W, respectively [19].

### 1.3. Role of fundamentals, materials, and machine learning

Although commercial PEMFC systems are now available in various applications, a few more years is anticipated prior to their worldwide deployment to reduce cost and improve durability, and after that, the technology will be further advanced like the ICEs in the past hundreds of years. Advancements in materials, operational control, and design are crucially important to cost reduction and durability/performance enhancement. In operation, multiple interrelated and complex phenomena occur in fuel cell operation, including mass/heat transport, electrochemical reactions, and ionic/electronic conduction, which govern energy conversion and efficiency. Breakthroughs in material development, acquisition of fundamental knowledge, and development of analytical models and experimental tools are highly needed at the current stage of fuel cell R&D. For example, non-platinum metal group (non-PMG) catalysts, new membrane materials, platinum (Pt) loading reduction, and high current operation are critical for cost reduction. Advanced strategies for water/thermal management and system health monitoring ensure high performance and durability in operation. Machine learning and artificial intelligence (AI), a powerful tool for data analysis/classification, system control/monitoring, and design/performance optimization, have received increasing attention in material and energy development, as shown in Fig. 2, which plots the numbers of patents related to AI, machine learning, and deep learning in the energy field in the period of 2000–2017. Machine learning, physics-informed deep learning, and AI can facilitate the development of fundamental knowledge and correlations, material selection and advancement, fuel cell design and optimization, system control, power management, and monitoring of operation health, showing great potential to advance PEMFC technology. This review focuses on the discussion of fundamental principles, material challenges, and machine learning applications in PEMFCs. Although the review attempts to cover most literature on this topic, there are undoubtedly some that may have been left out.

## 2. PEM fuel cell technology status

Portable, transportation, and small stationary power generation are three primary areas for PEMFC applications. The power of portable fuel cells usually ranges from 5 to 50 W. That of electric passenger cars, utility vehicles, buses, and heavy-duty trucks ranges from 20 to

250 kW. Stationary PEMFCs are usually targeted for 100 kW to 2 MW of power for backup or data center power solution. Some small-scale stationary PEMFCs, e.g. for remote telecommunication and residential applications, have a power level of approximately 100 W to 1 kW [21].

### 2.1. Portables

Portable power has a small share within the fuel cell market, and the number of units shipped has been decreasing in the last decade back to the levels in 2008, as shown in Fig. 3. During 2012–2014, shipments of portable fuel cell systems increased more than three folds because of the introduction of micro fuel cell chargers for consumer electronics [22]. Nevertheless, such sales have become negligible due to the competitiveness and performance improvement of battery technology, and most players have exited the consumer electronics fuel cell market. In 2019, Swedish myFC announced the discontinuity of the company's consumer products including its JAQ Hybrid power bank [25]. In 2015, British Intelligent Energy stopped developing its UPP fuel cell charger to focus on the integration of fuel cells in smartphones and drones [24,26].

Currently, portable PEMFC applications include small-size off-grid and backup power, non-automotive auxiliary power units (APUs), and military applications. The main player in the sector is Germany SFC Energy. In addition to its original DMFC systems up to 500 W, in 2018, the company entered the hydrogen fuel cell market after signing a development partnership and licensing agreement with adKor [18]. SFC Energy provides off-grid energy systems for the oil and gas industry at remote locations, backup or uninterruptible supply for industrial equipment, APUs for special or recreational vehicles, and portable power supply for defense and security. Danish SerEnergy capitalizes on high temperature PEMFC technology to deliver compact methanol-powered systems with a power capacity of up to 5 kW for off-grid and backup power applications [27]. Using the same concept, German Siqens developed 500 W units for off-grid utilization [28]. British BOC, a member of Linde Group, commercialized 175 W fuel cell modules together with H<sub>2</sub> cylinders for customers requiring long off-grid operation [10,29].

Portable PEMFCs have also been developed as a promising power source for military applications. They showed promise in increasing the flight time of unmanned aerial vehicles (UAV) to approximately 8 h and reduced the refueling time to a few minutes. Less maintenance and zero lubricants are required because of the absence of moving parts in fuel cells. They can be used as wearable power supply devices and can replace batteries to reduce the carry-on weight for soldiers. Several R&D efforts were recently summarized by Wang et al. [11].

### 2.2. Transportation

The transportation sector is the primary application of PEMFCs because of their zero emission, high efficiency (as high as 65% in practice),

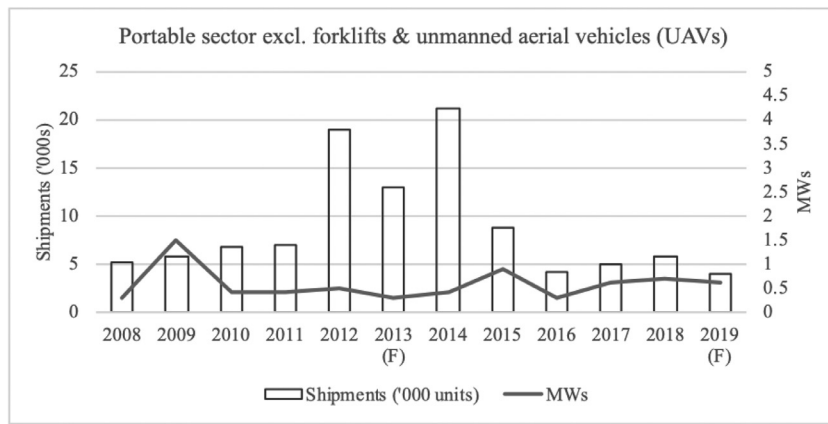


Fig. 3. Fuel cell shipment and power generation in the portable power sector [10,22-24].

**Table 2**  
Numbers of FCEVs sold by 2019 and roadmaps of 2020–2040 in USA, South Korea, Japan, Europe, and China.

	FCEV sold by Dec 2019 [30]	FCEV milestones		
		2020s	2030	2040
USA [31]	8089	200 K by 2025*	5.3M*	-
South Korea [32-34]	5068	67 K by 2022	~850K	2.9M
Japan [35]	3611	200 K by 2025	~800K	-
Europe [36]	2485	800 K by 2025*	4.2M*	21.3M*
China [37,38]	112	50 K by 2025	1M	-

\* Ambitious scenarios by private sector representatives.

and high power density. Major motor companies have been extensively involved in FCEV development to overcome the major barriers to commercialization, including cost, durability, and cold-start capability.

More than 19,000 FCEVs were sold worldwide by the end of 2019 [30]. Approximately, 7500 units were delivered in 2019 alone (90% increase with respect to the previous year), and more than half of them were delivered in South Korea [39,40]. In addition, 86% of the all-time sales were concentrated in California, South Korea, and Japan because of the strong policy support in these regions [32,35,41-43]. As of 2019, the U.S. currently has over 8000 FCEVs and 44 hydrogen refueling stations. In Europe, ~2500 FCEVs have been deployed. In Asia, there were over 3000 FCEVs in Japan and South Korea by 2019, and they are expected to be over 200 K and 1.6 M by 2025 and 2040, respectively, according to the 2020–2040 roadmaps. Although China has only about 112 currently, its ambitious plan reveals that 50 K and 1 M FCEVs will be deployed by 2025 and 2030, respectively. Table 2 summarizes the numbers of FCEVs in these major counties, along with future milestones in their hydrogen roadmaps. Significantly, the South Korean [32], Japanese [35,44], and Chinese [37] hydrogen roadmaps were released by the government or governmental agencies, while in the U.S. [31] and Europe [36], they were created by private sectors. Leveraging on the current momentum in the fuel cell and hydrogen industry, policy support is necessary to enable operational scale-up and accelerate the wide deployment of the technology [45,46].

As of 2020, Hyundai, Toyota, and Honda have launched high-volume FCEVs. Table 3 summarizes their fuel cell stack and hydrogen tank configurations, driving range, and MPGe. In 2019, ~63% of the total sales came from Hyundai Nexo, 32% from Toyota Mirai, and less than 5% from Honda Clarity Fuel Cell [39]. Launched in 2018, Hyundai Nexo features a more efficient stack, lighter and more compact powertrain, and 40% more range up to the world’s highest 380 miles (EPA [47]) than its predecessor Tucson FCEV [48]. According to Hyundai’s ‘FCEV Vision 2030’, the aim is to produce 700,000 fuel cell systems annually by 2030, including 500,000 for FCEVs [49]. Cumulatively, Toyota Mirai is the most sold FCEV with over 10,000 units sold since its introduction in 2014. The adoption of a 3D fine-mesh porous media flow field and thinner membrane (~10 μm thick) significantly improved the reactant

and water management with respect to the company’s previous 2008 model, leading to higher efficiency and enabling the removal of external humidification [50,51]. The first generation FCEV Mirai is equipped with a 114-kW (153-HP) PEMFC stack with a 3.1-kW/L power density. In the 2019 Tokyo Motor Show, Toyota unveiled its second generation Mirai concept, scheduled for launch in 2020, with a 30% increase of the current 312-mile (EPA [47]) range [52]. From 2020, the automaker expects to ramp up sales and production capacity ten-fold up to 30,000 per year [53]. Despite its availability on lease since late 2016, the deliveries of Honda Clarity Fuel Cell are far behind those of Hyundai and Toyota [39,54]. Besides, since 2013, Honda and General Motors have been co-developing their next-generation PEMFC systems and hydrogen storage technologies [55]. In 2017, both companies established the auto industry’s first manufacturing joint venture to mass-produce advanced PEMFC systems starting around 2020 [56].

FCEBs are one of the best early transportation applications for PEMFC technology. In general, transit buses run at a lower speed and are subject to less dynamic operation than FCEVs. They operate in congested areas, such as big cities where pollution concerns are more urgent and are centrally located and fueled. Furthermore, buses also permit larger space and better mechanical protection for hydrogen tanks. In the U.S., more than 30 FVEBs are operated in the state of California, serving approximately 17 million passengers by 2017 [64]. Most of them have achieved or almost met the ultimate target of 25,000 h. The capital cost in 2016 was ~\$1.8 million per bus, and analysis showed a cost of ~\$1 million each on an order for 40 buses [65]. Europe has been particularly active in the development, demonstration, and deployment of FCEBs, leveraging on strong EU support through a series of public-private projects. By the end of 2019, approximately 100 FCEB demonstrations were completed across the continent [66]. Significant milestones include the achievement of 35,000 h by a Ballard fuel cell stack integrated on a Wrightbus in London [10,67], and the ‘Bus of the Year 2019’ award by Van Hool’s FCEB Exqui.City18 [68,69]. Currently, a total of 12 European bus OEMs are pursuing fuel cell activities, and ~1300 FCEB deployments are planned within the next few years [30,66]. The largest-scale deployment projects are the Joint Initiatives for hydrogen Vehicles across Europe (JIVE and JIVE 2) and the H2Bus Europe. The



**Table 3**  
PEM fuel cell electric vehicles (FCEVs) [11,57-62].

Vehicle Model	Stack Max Power	Fuel Economy MPGe (City/Highway/Comb)	Stack Power Density	Fuel Pressure (MPa)	Fuel Tank Capacity (kg) (wt%)	Range (EPA [47])
Hyundai Nexso [63]	95 kW	65/58/61	3.1 kW/L	70	6.33 (7.18 wt%)	380 miles
Honda FCX Clarity Fuel Cell	103 kW	69/67/68	3.12 kW/L	70	5.46 (6.23 wt%)	366 miles
Toyota FCEV Mirai	114 kW	67/67/67	3.10 kW/L	70	5.0 (5.70 wt%)	312 miles (122.4 L H <sub>2</sub> /70 MPa)
Hyundai Tucson Fuel Cell	100 kW	49/51/50	1.65 kW/L	70	5.64 (6.43 wt%)	265 miles
Daimler GLC F-CELL Hybrid SUV Plug-in	~155 kW for car total power output	Combined hydrogen consumption: 0.34 kg/100 km	-	-	-	~430 km (4.4 kg H <sub>2</sub> @700 bar)+51 km (Battery)
Saic MAXUS FCV80	115 kW	-	3.10 kW/L	35	6	312 miles

**Table 4**  
PEM fuel cell electric buses (FCEBs) in Europe and the U.S.

ID	Fuel Cell System	Max Stack Power (kW)	Battery Capacity (kWh)	H <sub>2</sub> Storage Capacity (kg)	Range (mile)	OEM
ACT ZEBA	UTC Power	120	EnerDel/17.4	40	204	Van Hool [65]
SL AFCB	Ballard	150	A123/11	50	260	ElDorado National [65]
UC Irvine AFCB	Ballard	150	A123/11	50	244	ElDorado National [65]
A330 Fuel Cell	Ballard	85	24 or 36	38	220-250	Van Hool (Belgium) [71-74]
Businova	Symbio H2Motiv	30	132	28	190	Safra (France) [75,76]
Streetdeck FCEV (double-decker)	Ballard	85	48	30	200-265 with increasing H <sub>2</sub> storage	Wrightbus (UK) [77-80]
H2.City Gold	Toyota	60	29-44	37.5	250	CaetanoBus (Portugal) [81,82]
Urbino 12 hydrogen	Ballard FCmove-HD	70	30	37.5	220	Solari (Poland) [83-85]

former aims to deliver almost 300 FCEBs in 22 cities of 10 countries by the early 2020s, with a maximum price of €650k each [66]. The latter intends to scale-up production and deploy 1000 FCEBs at commercially competitive prices, including 600 units in Denmark, Latvia and the UK by 2023 [70]. Table 4 summarizes FCEBs and their configurations in Europe and US.

PEMFCs have also been developed for airplane, airship, railway (and light railway), and marine applications. The technology has advantages of high energy and power density, which is ideal as airplane power for the main power plant of the UAV or APU for large aircrafts. Some developments were also reported or are ongoing to install PEMFCs in boats and ships to reduce the emissions of CO<sub>2</sub> and pollutants and the usage of fossil fuels [11].

### 2.3. Stationaries

The stationary application generally considers PEM fuel cells as primary power, backup power, and combined heat and power (CHP). In 2019, the worldwide market for stationary fuel cells was ~2.98 billion USD, and it is still rapidly growing [86]. The notable manufacturers include Plug Power, Fuel Cell Energy, UTC Power, and Fuji Electric [87]. As reported by the U.S. DOE, more than 235 MW stationary fuel cell power supply has been installed with about 8000 backup power units deployed or on order in the U.S. [88].

For primary power, stationary PEMFCs can not only serve as a supplementary of the grid, but can also act as distributed power sources when the grid is unavailable. The efficiency of conventional ICE-based power plants is ~30-40%, whereas that of a PEMFC power plant is up to 65% [11,88]. Additionally, the electricity demand considerably varies from on- to off-peak hours in cities. PEM fuel cells usually have excellent dynamic response and flexibility in output power adjustment. Thus, using PEM fuel cells as a supplementary solution for on-peak hours significantly improves the efficiency and dynamic characteristics. Moreover, the grid construction cost is high in the vast territory with a sparse population. A considerable amount of generated wind power and hydropower is not fully utilized because of the lack of large-scale energy storage in-

frastructure. A PEMFC power plant can be co-located with electrolyzers to efficiently utilize renewable resources for power supply. In California, more than 400 stationary fuel cell systems have been installed since 2001, supported by the Public Utilities Commission's Self-Generation Incentive Program, with 135 MW of electric-only and more than 40 MW of CHP fuel cell systems. The total installed capacity is expected to be 175 MW [89]. Furthermore, PEM fuel cells have also been developed as emergency backup solutions for core infrastructures that require uninterrupted power, such as factories, hospitals, signal towers, and banks. The DOE target for a PEMFC backup power of 1-10 kW is 15 years and 10,000 h with a mean time between failures of less than 5 years by 2020 [12]. PEM fuel cells provided emergency backup power to signal towers operating for hundreds of hours in both Bahamas and Northeast United States after Hurricane Sandy [88]. Additionally, PEM fuel cells are suitable to provide both power and thermal energy to residences or offices, which usually require a power level of 200-1000 W [17]. The overall efficiency of a fuel cell CHP system could be up to 80-95% [88]. In Japan, Panasonic and Toshiba Fuel Cell Power Systems (Toshiba FCP) began the sales of commercial products of ENEFARM fuel cell CHP units from 2009 [17]. Nearly 265,000 ENEFARM units were installed as of 2018 with a power capability of up to 5 kW. Japan plans to deploy 5.3 million of these units by 2030 [90].

### 2.4. Hydrogen refueling stations

Since December 2019, the U.S. has 44 hydrogen refueling (HRF) stations, almost all of which are located in the state of California. In Europe, there were 139 HRF stations in 2019, and ~1500 stations will be available by 2025 according to their roadmap. In Asia, the governments of China, Japan, and South Korea are supportive of PEMFC technology and HRF infrastructure development. Japan already had 112 HRF stations in 2019 and plans to open 320 and 900 hydrogen retailers by the end of 2025 and 2030, respectively. Although China and South Korea have a relatively small number of HRF stations at present, their ambitious plans show that more than 1000 stations will be developed by 2030. Table 5

**Table 5**  
Status and plan of hydrogen refueling (HRF) stations of USA, South Korea, Japan, Europe, and China.

	HRF stations installed by Dec 2019 [30]	HRF milestones		
		2020s	2030	2040
USA [31]	44	~580 by 2025*	5600*	-
South Korea [32-34]	34	310 by 2022	1200	1200
Japan [35]	112	320 by 2024	900	-
Europe [36]	139	~1500 by 2025*	~3700*	~15,000*
China [37,38]	12	300 by 2025	1000	-

\* Ambitious scenarios by private sector representatives.

lists the numbers of HRF stations installed till 2019 and milestones in the HRF roadmap for these counties.

### 3. Fundamentals and materials

For the hydrogen oxidation reaction (HOR) and oxygen reduction reaction (ORR) to proceed efficiently, the materials used in fuel cells must be chosen so that a high beginning of life performance and durability are ensured. For example, to improve the activation and reduce transport losses, various issues as discussed earlier need to be addressed, including durable electrocatalyst and its loading reduction [2], reactant/membrane contamination [91,92], water management [93,94], and degradation [95,96]. Material advance and improvement are therefore important for fuel cell R&D, and fundamentals that establish the material properties and fuel cell performance under various operation conditions are highly needed.

#### 3.1. Materials

##### 3.1.1. Membrane

The PEM is located between the anode and cathode CLs. Its main functions are two-fold: (i) it acts as a separator between the anode and the cathode reactant gasses and electrons, and (ii) it conducts protons from the anode to cathode CLs. Therefore, as a separator it must be impermeable to gasses (i.e., it should not allow the crossover of hydrogen and oxygen) and must be electrically insulating. In addition, the membrane material must withstand the harsh operating conditions of PEM fuel cells, and thus possess high chemical and mechanical stability [97].

Perfluorosulfonic acid (PFSA) is typically used as a PEM material for PEM fuel cells. The main chain is Teflon-like and highly hydrophobic. The sulfonic acid group as an end group of the side chain is highly hydrophilic; thus, it allows the adsorption of water for proton conduction. The membrane hydration is thus of importance and must have an optimal value to ensure that sufficient water is present for proton conduction without the risk of flooding the CLs and gas diffusion layers (GDLs). The length of the side chain is also an important factor in determining the stability and performance of the membrane. For PEMFC applications, the two types of PFSA membranes usually used are classified as long side chain (LSC), such as Nafion®, and short side chain (SSC), e.g. Aquiviun®, membranes. Their main difference is the number of CF<sub>2</sub> units and the structure of the side chain [98] (Fig. 4(a)). The physical structure of a Nafion XL membrane (LSC) is shown in Fig. 4(b).

Though PFSA is the state-of-the-art material used in PEM fuel cells, there are main drawbacks to this type of membrane that can hinder durability enhancement and cost reduction, summarized as follows:

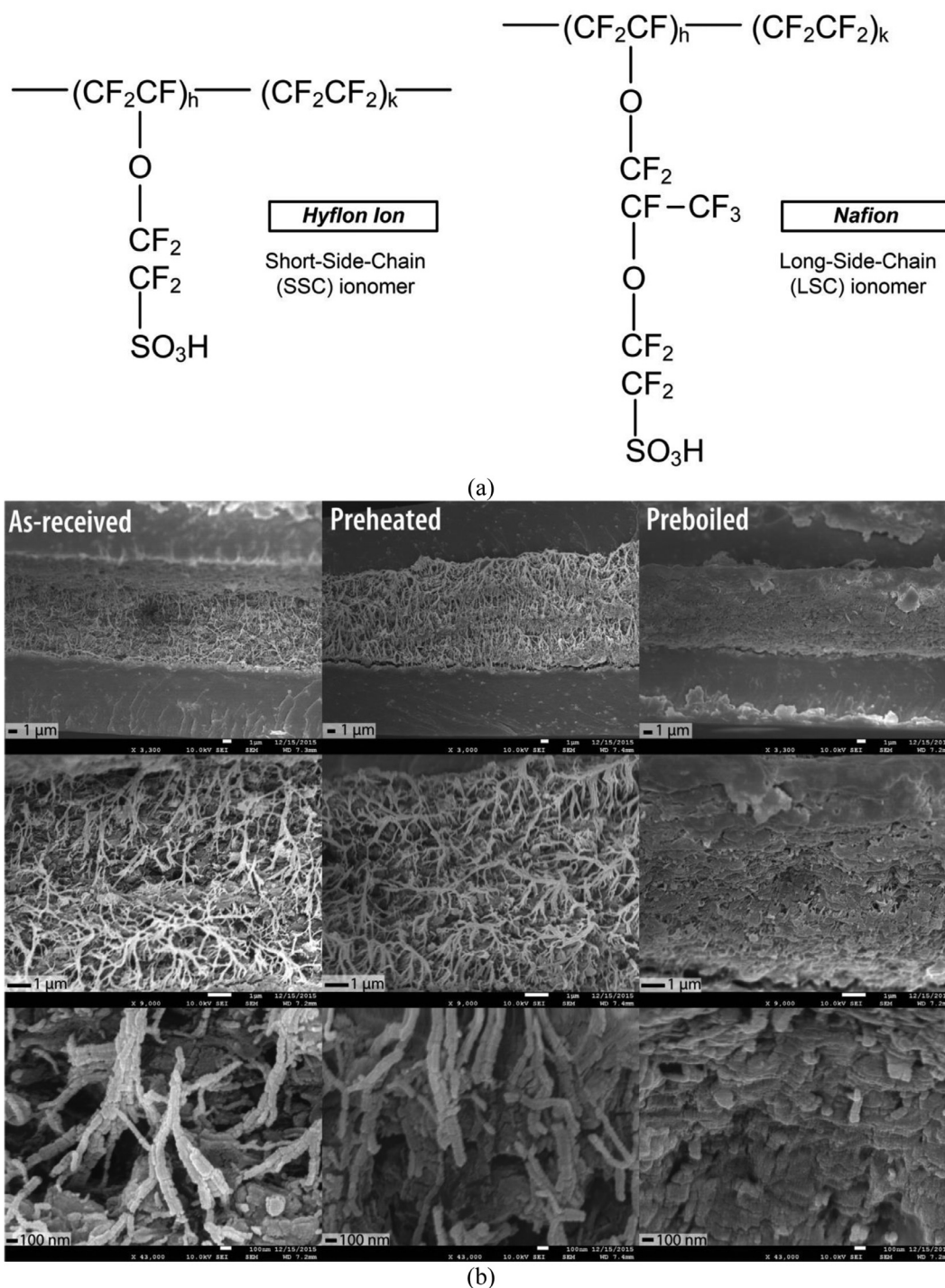
1. High proton conductivity occurs under its full hydration state and thus it is essential to humidify the reactant gasses, which raises cost and complication of a PEMFC system.
2. Its structure is susceptible to attack by metallic cations and consequent decomposition of the polymer chain. This will reduce its mechanical integrity and proton conductivity.
3. Cyclic changes in its hydration during PEMFC operation can result in membrane failure due to the associated structural swell/shrinking.

This can be mitigated by using reinforcement and appropriate fillers to improve polymer structure, which increases cost.

In addition, it was reported that the polymer backbone (-CF<sub>2</sub>-) may react with hydrogen through: -CF<sub>2</sub>- + 2H<sub>2</sub> → -CH<sub>2</sub>- + 2HF, causing membrane degradation [95]. Consequently, for the past years, polymer research in PEM fuel cells has focused on finding alternative membrane materials that are not only cost-competitive but also exhibit high durability and stability over a wide range of operating conditions, particularly under the extreme conditions of low humidity (e.g. 0%RH) and high (e.g. >120 °C) and sub-zero temperatures, which have been extensively reviewed in the literature [100,101]. Some alternative solid polymer electrolyte materials offer the advantage of low cost while eliminating the need for humidification. However, their conductivity and stability during the fuel cell lifetime suffer. A summary of major alternative membrane materials is presented in Table 6. Machine learning and AI can play an important role in membrane material development. Durable, cost-effective membranes with high ionic conductivity and minimal hydration requirement are highly desirable for PEM fuel cells. In addition, proton-conducting polymer membranes are extensively studied in other fields, such as water electrolysis, chlor-alkali production, metal-ion recovery, flow battery, and gas drying/humidification. Machine learning will be very valuable to analyze the large set of material data available in the literature, such as ionic conductivity, material structure, function groups, hybrid configuration, and subfreezing performance, for material selection and optimization. In fuel cell operation, ion transport, species cross-over, water diffusion/permeation, and material degradation occur in the membrane, which can be incorporated into machine learning and AI through their fundamental mechanisms and equations for control optimization, degradation mitigation, and real-time diagnostics.

##### 3.1.2. Catalyst layers

Catalyst layers (CLs) are the component where the electrochemical reactions occur. The CL material must provide continuous pathways for various reactant species; primarily, (i) a path for proton transport, (ii) a pore network for gaseous reactant supply and water removal, and (iii) a passage for electron conduction between the CL and the current collector. The CL material is a major factor affecting fuel cell performance and durability. Conventional CLs are composed of electrocatalyst, carbon support, ionomer, and void space. Optimization of the CL ink preparation has been the main driver in PEMFC development [21,102]. This breakthrough highlights the importance of the so-called triple-phase boundaries of the ionomer, Pt/C, and void space so that all reactants could access for the reactions. Conventional CLs are prepared based on the dispersion of a catalyst ink comprising a Pt/C catalyst, ionomer, and solvent. Ink composition is important for aggregation of the ionomer and agglomeration of carbon particles, and the dispersion medium governs the ink's properties, such as the aggregation dimension of the catalyst/ionomer particles, viscosity, and rate of solidification, and ultimately, the electrochemical and transport properties of the CLs [103-105]. The ionomer not only acts as a binder for the Pt/C particles but also proton conductor. Imbalance in the ionomer loading increases the transport or ohmic loss, with a small amount of ionomer reducing



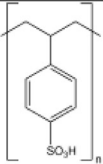
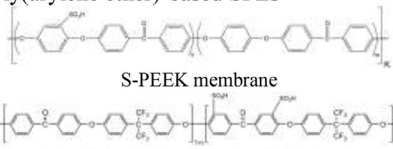
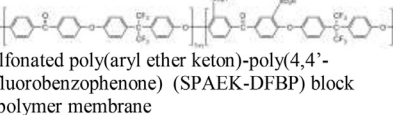
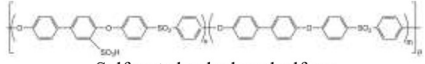
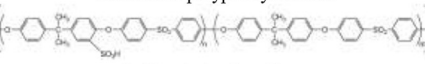
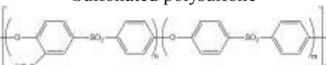
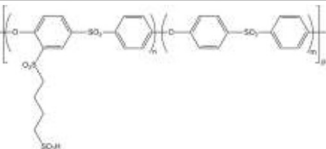
**Fig. 4.** (a) Polymer structures of Hyflon Ion/Dow and Nafion [98], (b) SEM images of Nafion XL membrane in the as-received form (AsR) after being pretreated in water. Rows from top to bottom show low ( $\times 3000$ ), medium ( $\times 9000$ ), and high ( $\times 43,000$ ) magnification [99].

the proton conductivity and a large amount increasing the transport resistance of gaseous reactants.

In contrast, non-conventional CLs are structured such that one of the major ingredients in their conventional counterparts is eliminated [2,102]. Nanostructured thin film (NSTF) CLs from 3 M are the most successful non-conventional CL. They consist of whiskers where the catalyst is deposited without ionomer for proton conduction. Over the years, they have proven to provide a higher activity than conventional CLs, as seen in Fig. 5. In addition, similar to conventional CLs, annealing can be used to change the CL structure and ultimately change its activity.

Carbon is the most commonly used support material for catalyst because of its low cost, chemical stability, high surface area, and affinity for metallic nanoparticles. The surface area of the support varies depending on its graphitization process and is reported to range from 10 to 2000  $\text{m}^2/\text{g}$  [107]. Ketjen Black and Vulcan XC-72 are popular carbons with a surface area of 890  $\text{m}^2/\text{g}$  and 228  $\text{m}^2/\text{g}$ , respectively [108]. Carbon tends to aggregate, forming carbon particle agglomerates with a bimodal pore size distribution (PSD). This PSD is usually composed of the primary pores of typically 2–20 nm in size and secondary pores larger than 20 nm. The primary pores are located between

**Table 6**  
Summary of alternative membrane materials to PFSA [100].

Material	Comments
Polystyrene-sulfonic acid (PSSA)	They are relatively inexpensive compared to Nafion with a main disadvantage of their instability. Specifically, styrene sulfonic acid fragments are lost at high rates, reducing ion exchange capacity and conductivity. Tertiary benzylic hydrogen and the aromatic ring protons in the polymer chain form these weak points.
	Strengthening these chains is vital.
Sulfonated polyimide (SPI)-based membranes	Their main advantages are the high mechanical and thermal properties along with durability against aggressive chemicals and heat because of their thermostability. Sulfonation of polyimides has been used to increase proton conductivity. Their main drawback originates from their instability under hydrated states due to hydrolytic, oxidative, and swelling-stress stability.
	Polybenzimidazole (PBI)-based membranes
Sulfonated aromatic main-chain polymers I: Poly(arylene ether)-based SPEs	They are tailored for operation at 160-220 °C, and thus are suitable for PAFCs. The main challenges are: (i) electrolyte leakage, (ii) presence of a liquid electrolyte and hence possible GDL flooding, and (iii) unsuitability for portable and transport applications. R&D also uses them in a new class of membranes with improved matrix for H <sub>3</sub> PO <sub>4</sub> .
Sulfonated aromatic main-chain polymers II: Polysulfone-, polysulfone-ether-, and polyphenylsulfone-based SPEs	They comprise sulfonated aromatic main-chain polymers and are cost-competitive with high mechanical strength and chemical/thermal stability. The SPEAKs and SPEEKs are most studied. Various combinations are also possible [102]. The main disadvantage is durability due to the scission of their main chain. Structural improvement of their backbone is vital.
 <p>S-PEEK membrane</p>  <p>Sulfonated poly(arylene ether ketone)-poly(4,4'-difluorobenzophenone) (SPAEEK-DFBP) block copolymer membrane</p>  <p>Sulfonated polyphenylsulfone</p>  <p>Sulfonated polysulfone</p>  <p>Sulfonated polyethersulfone</p>  <p>Sulfobutylated polyethersulfone</p>	



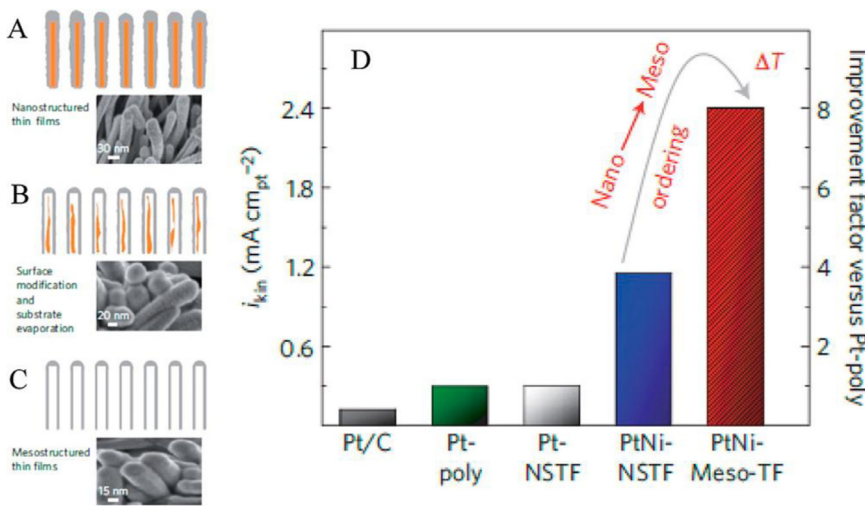


Fig. 5. Schematic illustration and corresponding HRTEM images of the mesoscale ordering during annealing and formation of the mesostructured thin film starting from the as-deposited Pt-Ni on whiskers (A), annealed at 300 °C (B) and 400 °C (C). Specific activities of Pt-Ni NSTF as compared to those of polycrystalline Pt and Pt-NSTF at 0.9 V (D) [106].

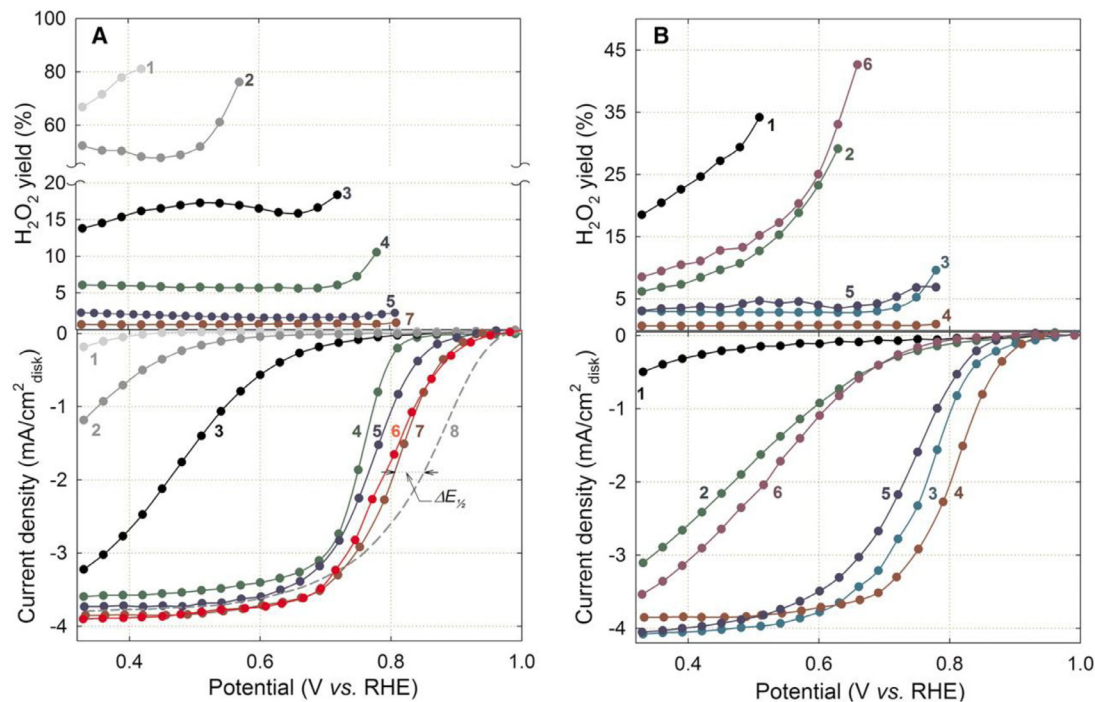


Fig. 6. (A) Steady-state ORR polarization plots (bottom) and H<sub>2</sub>O<sub>2</sub> yield plots (top) measured with different PANI-derived catalysts and reference materials: 1, as-received carbon black (Ketjenblack EC-300 J); 2, heat-treated carbon black; 3, heat-treated PANI-C; 4, PANI-Co-C; 5, PANI-FeCo-C(1); 6, PANI-FeCo-C(2); 7, PANI-Fe-C; and 8, E-TEK Pt/C (20 μgPt/cm<sup>2</sup>). Electrolyte: O<sub>2</sub>-saturated 0.5 M H<sub>2</sub>SO<sub>4</sub> [0.1 M HClO<sub>4</sub> in an experiment involving Pt catalysts (dashed lines)]; temperature, 25 °C. RRDE experiments were performed at a constant ring potential of 1.2 V versus RHE. RDE/RRDE rotating speed, 900 rpm; non-precious metal catalyst loading, 0.6 mg/cm<sup>2</sup>. (B) Steady-state ORR polarization plots (bottom) and H<sub>2</sub>O<sub>2</sub> yield plots (top) measured with a PANI-Fe-C catalyst in 0.5 M H<sub>2</sub>SO<sub>4</sub> electrolyte as a function of the heat treatment temperature: 1, 400 °C; 2, 600 °C; 3, 850 °C; 4, 900 °C; 5, 950 °C; and 6, 1000 °C [111].

carbon particles in an agglomerate, while the secondary pores are between agglomerates. Depending on the Pt distribution and utilization within an agglomerate, the primary pores play a key role in determining the electrochemical kinetics, while the secondary pores are important for reactant transport across a CL. The portion of the primary and secondary pores is largely determined by the surface area of the carbon support [108]. Hence, it has been reported that carbon supports also determine the optimal ionomer content and the Pt distribution in CLs [109,110]. Additionally, the anode overpotential is usually considered negligible in comparison with its cathode counterpart because of the sluggish ORR. Thus, most work in the literature is focused on cathode CLs. CL optimization is focused on not only enhanced durability but also reduction of the Pt loading. For this purpose, it is crucial to

determine the optimal combination of the carbon support and catalyst for loading reduction. An example is highlighted in Fig. 6, where different carbons are heat-treated to induce the catalytic activities of PANI-derived catalysts and to ensure their performance and stability. Rotating Ring-Disk Electrode (RDE) measurements were conducted to study the ORR activity of various heat-treated PANI-C catalysts as a function of temperature.

The durability and stability of CL material are a major subject in R&D, which is related to multiple factors, mainly including (i) operating and environmental conditions, (ii) oxidant and fuel impurities, and (iii) contaminants and corrosion in cell components. For instance, operation under high voltages (above 1.35 V), which may occur during fuel cell startup and shut-down, can lead to Pt dissolution [112]. Operation

further above this voltage will cause degradation of the carbon support, known as carbon corrosion. In addition, any traces of a contaminant in the fuel or oxidant feeds can lead to a decrease in fuel cell performance by poisoning CL materials [113,114]. Some contaminants cover the Pt catalyst and then reduce the electrochemical surface area (ECSA) available for the reaction. This catalytic contamination is usually reversible upon removal of the contaminants. In certain instances, contaminants such as ammonia will cause irreversible degradation under adequate exposure time and concentration [44]. Further, cell components, such as CLs and BPs, may contain contaminants, from their manufacturing process and/or material used, which eventually leach out and cause poisoning of the MEA. This may include membrane poisoning by metallic cations [91].

Up to date, Pt is the electrocatalyst of choice for the ORR in PEM fuel cells because of its high activity. However, Pt has a high cost associated with it and is currently mined in mainly several countries, such as South Africa and Russia. Furthermore, high Pt loading is required to reach the target lifetime without major efficiency loss. Using state-of-the-art methods, Pt catalyst is distributed in a way that does not allow its full utilization in CLs [115,116]. Alternative catalysts that are either Pt free or Pt alloys are under research. Two excellent review papers on the topic are provided by Ref. [117,118]. A summary of some of these catalysts, their current status, and remaining challenges is provided in Fig. 7.

Machine learning and AI are extremely helpful and highly demanding for CL development providing that CLs have been extensively studied for not only PEM fuel cells, but also many other systems, such as electrolyzers and sensors with Pt-catalyst electrodes. The species transport equations, ORR reaction kinetics, two-phase flow, and degradation mechanisms can be encoded into the neural networks for effective physics-informed deep learning to understand the impacts of catalyst materials on fuel cell performance/durability and optimize the pore size, PSD, PTFE loading, ionomer content, and carbon and electrocatalyst loading. In the mass production phase, machine learning and AI can assist the quality control of CL composition in signal processing and element analysis when integrated with detection techniques such as Laser Induced Breakdown Spectroscopy (LIBS) [119].

### 3.1.3. Microporous and gas diffusion layers

Gas diffusion layers (GDL) and microporous layer (MPL), together called diffusion media (DM), are placed between a bipolar plate (BP) and the CL. Their main function is to provide mechanical support for MEAs, a passage for reactant supply and product removal, and a pathway for electron conduction between CLs and BPs. Both GDL and MPL are porous materials, with carbon paper being the option for commercial GDLs and carbon powder for MPLs.

Carbon paper is a carbon-fiber composite with fibers of  $\sim 7 \mu\text{m}$  in diameter. The fibers are held together by binder, which usually accounts for 5–15% of the final paper weight [120]. Carbon paper GDLs must be hydrophobic to improve water removal and avoid electrode flooding. Polytetrafluoroethylene (PTFE; brand name Teflon) is often added to carbon paper for hydrophobicity treatment. Additionally, carbon paper GDLs are anisotropic in their structure, as shown in Fig. 8.

As depicted in Fig. 8(c) and (d), at low loading, PTFE is usually concentrated at the surface region and penetrates deeper into the GDL as its loading increases. Another observation is that the binder structure of PTFE is changed in that it is no longer smooth but exhibits a web-like porous shape. A high PTFE loading will block the GDL pores, resulting in mass transport limitation. The PTFE loading also affects the PSD [121], and reduces overall pore volume. For a pore radius  $\leq 3 \mu\text{m}$ , no PSD change was observed, implying that PTFE does not penetrate the pores in this size range. Pores larger than  $5 \mu\text{m}$  were found to be the most affected with a significant decrease in volume as the PTFE loading increases from 5% to 20%. Hence, it is crucial to balance the GDL hydrophobicity and pore space for liquid removal and gaseous reactant supply, respectively.

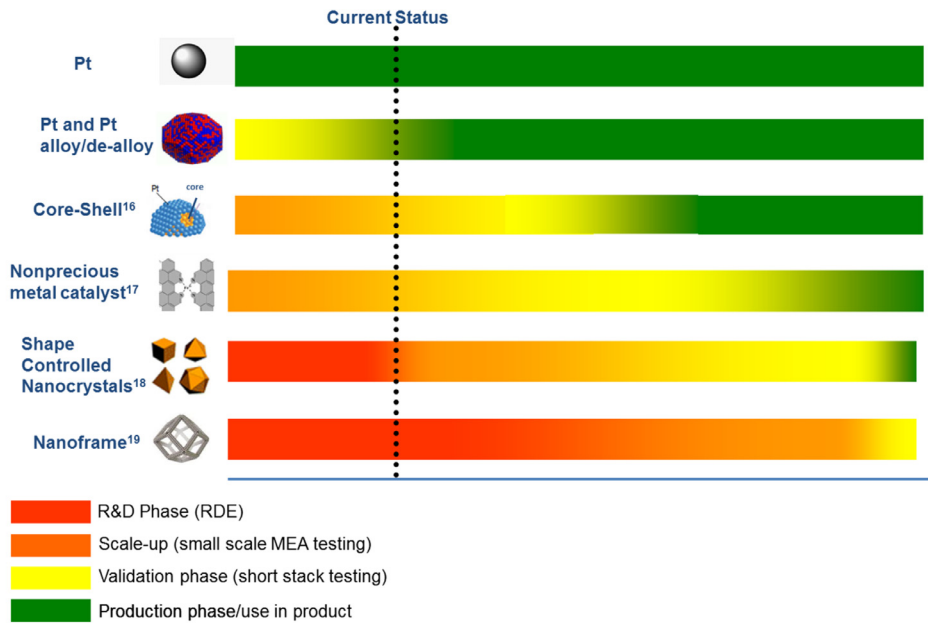
To improve the GDL-CL physical contact, a MPL is often introduced between the two layers. It usually has a pore size between those of GDLs and CLs and has been reported to enhance fuel cell performance in some occasions because of the improved water management in the cathode [122]. Its pores are primarily less than  $0.5 \mu\text{m}$  with a mean size of  $0.320 \mu\text{m}$  [123], while those in GDLs and CLs are mostly around  $6\text{--}20 \mu\text{m}$  [121] and less than  $0.02 \mu\text{m}$  [124], respectively. MPLs are composed of tightly packed carbon black particles (see Fig. 9), bound together by PTFE, which also makes MPLs hydrophobic. The MPL ink is usually coated onto the GDL surface during fabrication. Their main purpose is to provide a smooth, continuous interface between a GDL and a CL, thereby reducing the interfacial resistance. Other MPL benefits include (i) reduced overall ohmic loss mainly due to membrane hydration increase; (ii) electrode flooding mitigation; and (iii) enhancement of the MEA chemical and mechanical stability [125–134].

Machine learning and AI can be applied to optimize the design of both GDLs and MPLs, including their pore sizes, PSD, PTFE loading, permeability, and physical dimensions. The species transport equation, heat transfer and electric current conduction equations, Darcy's law, and two-phase flow model need to be encoded into the neural networks for effective physics-informed machine learning.


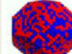
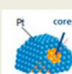


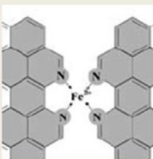
### 3.1.4. Bipolar plate and gas flow channel

BPs have multiple roles, including electric current collection, heat removal, gaseous reactant distribution, and water removal via their embedded gas flow channel (GFC) networks, and mechanical support. In addition to these functions, BP materials need to be corrosion resistant in the fuel cell environment. In the early stages of fuel cell development, graphite is a popular BP material because of its high corrosion resistance and electrical conductivity. However, graphite is brittle, making its mass production difficult, and may subject to leakage owing to its gas permeability. In commercial PEM fuel cells, carbon composites and metals with proper protective coating, including aluminum, stainless steel, or titanium, have been explored as potential BP materials.

Carbon composites consist of a polymer binder and conductive carbon fillers with the former providing mechanical strength and gas impermeability and the latter offering electron and heat conductive pathways. Increasing the filler loading or combining multiple types of fillers, such as carbon black, carbon fibers, graphite particles, and carbon nanotubes, may enhance the composite conductivity through improving carbon cluster connection. However, overloading fillers will reduce BP mechanical strength, causing cracks or material failure. The geometry or morphology and loading of carbon fillers are key factors determining the composite BP's properties. Metal BPs are advantageous in multiple aspects, such as easy machining, high electric and thermal conductivities, low gas permeability, and mechanical robustness. A major challenge is corrosion resistance in the acidic environment of fuel cells. To prevent corrosion, proper coating needs to be applied to protect the metal substrates. For aluminum, metallic nitrides, carbon, and composite coatings are popular coating materials. For stainless steels, a graphene-Ni layer, nitrides, and chromium carbide have been investigated as potential coating materials. Although pure titanium has a higher corrosion resistance to stainless steel, pure titanium may be subject to the formation of an oxide layer on its surface in fuel cell environment [135]. Gao et al. [135] proposed a carbon/PTFE/TiN composite coating using a two-step hydrothermal and impregnation process and found that it significantly improves the corrosion resistance and surface hydrophobicity. Toyota Mirai adopted a carbon-coated Ti plate as its cathode and anode BPs. In coatings, surface defects may occur, leading to pinhole formation and pathways for corrosives to reach the metal substrate. Multi-layered coatings offer an engineering solution to resolve this issue. Furthermore, physical vapor deposition (PVD) techniques may cause surface defects, such as craters and droplets. Surface defect mitigation is an important issue in metal BP development [11]. de Oliveira et al. [136] proposed a trade-off strategy to screen BP materials based on evaluation of the corresponding Ashby charts. They examined graphite-polymer compos-



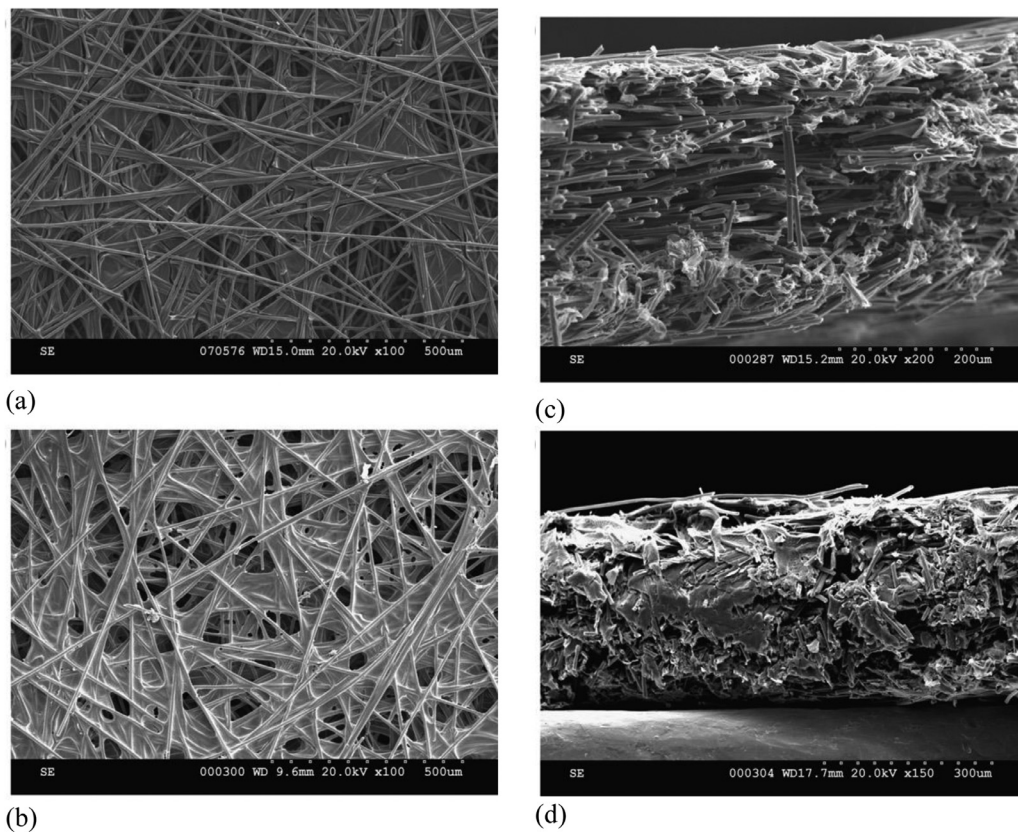
(a)

Catalyst Type	Benefit	Remaining Challenges
Pt 	1) Mature technology	1) Unable to meet long term automotive Pt loading and catalyst layer durability targets
Pt alloy/de-alloy 	1) Mature technology 2) Improved performance over Pt/C 3) Enhanced membrane/MEA durability	1) Difficult to meet long term automotive Pt loading target
Core-shell <sup>16</sup> 	1) Improved mass activity over Pt alloy 2) Improved durability over Pt/C 3) Highest reported ECSA	1) Difficult to maintain quality of 'shell' 2) Dissolution of 'core' still a concern
Shape controlled nanocrystal <sup>18</sup> 	1) Significantly higher mass activity (~15 x) over Pt 2) Chemical synthesis (vs. electrochemical) may allow for easier scale up vs. core-shell	1) Scale up is at an early stage 2) Conflicting data on stability 3) MEA performance has not been demonstrated yet
Nanoframe/nanocage <sup>19</sup> 	1) Significantly higher mass activity (> 20 x) over Pt 2) Highly stable (improved durability over Pt/C)	1) Scale up is at an early stage 2) Ionomer penetration into nanocage will likely be difficult 3) MEA performance at high current density may be challenging
Non-precious metal catalyst <sup>17</sup> 	1) Potentially offer the largest benefit (significant cost reduction) 2) Tolerant to common contaminants	1) Close to meeting targets for non-automotive applications (e.g. backup power) but far from meeting automotive targets. 2) At current volumes, PGM loading is not a major concern for non-automotive applications.

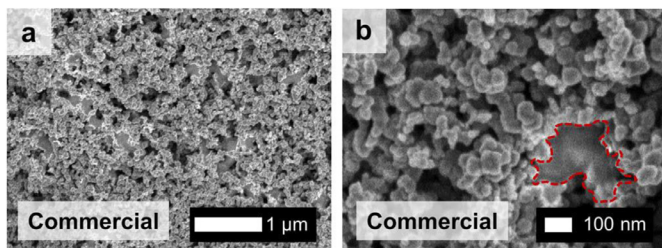
(b)

Fig. 7. (a) Development timelines for Pt, Pt alloy/dealloy, core-shell, nonprecious metal, shape-controlled and nanoframe ORR electrocatalysts, (b) benefits and remaining challenges for each of the primary categories of electrocatalysts [117].





**Fig. 8.** SEM images of (a) TORAY-TPGH-120 with 0% PTFE and (b) TORAY TPGH-120 with 50% PTFE; (c) cross-section image of TORAY-TPGH-120 with 20% PTFE; and (d) cross-sectional image of TORAY-TPGH-120 with 50% PTFE—the in-plane direction is defined as the plane perpendicular to the carbon fibers (a and b showing the xy plane, c and d showing the xz plane—the in-plane direction is perpendicular to the xz plane) [121].



**Fig. 9.** SEM top-view images of a commercial MPL (Freudenberg) [133].

ites and metals using literature data and recommended multiwall carbon nanotubes (MWNT) and carbon fibers as minor fillers in addition to graphite. They also indicated that pack chromization, nitridation, and multi-layered PVD films yield the best performance for metallic BPs. Similar approaches can be developed using machine learning and AI to screen BPs and coating materials based on the abundant data available in the literature.

GFCs are embedded in BPs to distribute gaseous reactants and remove byproduct water. A desirable GFC design evenly distributes reactants and effectively removes water product with a minimal demand for pumping power. Several GFC designs have been widely investigated, including parallel, serpentine, pin-type, interdigitated, and porous media flow fields. Additionally, cross-sectional geometry, GDL intrusion, and surface properties are important factors affecting GFC performance. At the GDL surface, droplets may emerge and block reactant flow in the

GFC and diffusion to the CL. Thus, proper droplet removal strategy is needed, which can be developed through analyzing the force balance and its relevance to the gas velocity, surface roughness and wettability, and droplet size [137,138]. Moreover, two-phase flow in GFCs is crucial to reactant distribution and water removal. To ensure the GDL surface is free of liquid flow, other channel surfaces should be more hydrophilic. Furthermore, bypass flow between two neighboring channels may occur, driven by their pressure difference, causing reactant leakage and local reactant starvation. This bypass flow is determined by the GDL permeability, land dimension, and assembly pressure on BPs. A novel design of porous medium GFCs was proposed by Wang [139-142], in which GFCs provide additional functions of heat removal and electron conductance via their solid matrix. This concept enables a flexible GFC design, including the cross-sectional dimensions, material structure (e.g., random and regular structures), novel fabrication (e.g., metal foam or plate manufacturing), and material selection (e.g., solid matrix and coating materials). Toyota Mirai FCEVs adopted carbon-coated Ti porous medium GFCs on the cathode. Other porous media have also been investigated as potential GFC materials, including carbon/graphite/graphene foams, metal (aluminum, nickel, and stainless steel) foams, and metal porous plates, as presented in Table 7. Metal materials usually need a proper protective coating to survive fuel cell conditions, such as titanium and aluminum. Machine learning and AI are extremely helpful in the optimization of GFC design, including flow-field arrangement, cross-sectional shapes, counter/co-flow configuration, and material and pore networks of porous media GFCs. The flow equations, Darcy's law, species transport equation, and heat transfer and electric current flow equations, need to be encoded into the neural networks for effective physics-informed deep learning.



**Table 7**  
 Porous media flow field materials for PEM fuel cell [143].

Porous media materials	Microstructure	Features
Metal/alloy foam (e.g., Al, Ni, and Cu foams)		High porosity (e.g., 95–98% before compression and ~80–95% after compression and PTFE treatment); Pore size range (0.230–1.59 mm) Good mechanical strength; Poor corrosion resistance; thus, coating is required.
Carbon/graphite foam		Porosity (64–99%, usually cannot be compressed); Pore size range (0.03–1.27 mm); Good thermal and electrical conductivity; Good corrosion resistance, Large surface area; Low density.
Graphene foam		High porosity (can be compressed, left: before compression; right: after compression); Pore size range (similar to that of metal foam); Good thermal and electrical conductivity; Good corrosion resistance; Good hydrophobicity; Slightly poor mechanical strength.
Carbon felt/cloth		Porosity (40–95%); Pore size range (0.001–0.08 mm); Good corrosion resistance.
3D Ti fine mesh (Toyota)		Enhanced convection for gas into porous electrodes; Good mechanical strength; Good corrosion resistance; Good liquid water removal capacity.
3D porous plate using stainless steel (Poss470FC) (Hyundai)		Good mechanical strength; Good corrosion resistance; Good electrical conductivity.

The technical targets set by the DOE for various fuel cell components are summarized in Table 8.

### 3.2. Two-phase flow

Two-phase flow, originated from water production by the ORR, is an important phenomenon in PEMFCs, where the two phases refer to the reactant gasses and liquid water. Excessive liquid water will hinder reactant delivery to the reaction sites, thereby increasing the concentration polarization. This “flooding” issue leads to multiple concerns, including material degradation, performance reduction, operation stability, and local reactant starvation that causes material degradation.

In porous components such as CLs, MPLs, and GDLs, liquid water flow is mainly driven by the capillary pressure ( $P_c$ ) defined as the pressure difference between the liquid and gas phases. A common  $P_c$  correlation is the Leverett  $J$ -function, which expresses it as a function of liquid saturation ( $s$ ) and material properties, such as porosity ( $\theta_c$ ), contact angle ( $\theta_c$ ), surface tension ( $\sigma$ ), and permeability ( $K$ ) [145,146]:

$$P_g - P_l = P_c = \sigma \cos(\theta_c) \left( \frac{\epsilon}{K} \right)^{1/2} J(s), \quad (1)$$

where  $\sigma$  is the surface tension and the Leverett  $J$ -function  $J(s)$  is expressed for hydrophobic and hydrophilic media as follows:

$$J(s) = \begin{cases} 1.417(1 - s) - 2.120(1 - s)^2 + 1.263(1 - s)^3 & \text{for } \theta_c < 90^\circ \\ 1.417s - 2.120s^2 + 1.263s^3 & \text{for } \theta_c > 90^\circ \end{cases} \quad (2)$$

**Table 8**  
2025 DOE technical targets of PEM fuel cells [144]. \*Some statuses are based on specific material performance.

Characteristic	Units	Status*	2025 Target
<i>MEA and Catalysts</i>			
Pt group meta (PGM) total content	g kW <sup>-1</sup> rated	0.125:1.05 (150, 250 kPa)	≤0.10
Durability with cycling	Hours	4100	8000
Performance @ 0.8 V	mW cm <sup>-2</sup>	306	300
Performance @ rated power guideline	mW cm <sup>-2</sup>	890; 1190 (150,250 kPa)	1800
Loss in catalytic (mass) activity	%	40	≤40% loss of initial
Loss in performance @ 0.8 A cm <sup>-2</sup>	mV	20	≤30
Electrocatalyst support stability	% mass activity loss	Not tested	≤40
Loss in performance @ 1.5 A cm <sup>-2</sup>	mV	>500	≤30
Mass activity	A mg <sub>pgm</sub> <sup>-1</sup> @ 900 mV <sub>IR-free</sub>	0.6	0.44
PGM-free catalyst activity	A cm <sup>-2</sup> @900 mV <sub>IR-free</sub> A	0.021	0.044
<i>Membranes</i>			
P referred maximum operating temperature	°C	120	120
Area specific proton resistance at: 120 °C and water partial pressure of 40 kPa	Ω cm <sup>2</sup>	0.054 (40 kPa) 0.019 (80 kPa)	0.02
95 °C and water partial pressure of 25 kPa	Ω cm <sup>2</sup>	0.027 (25 kPa) (at 80 °C 0.02 at 25 kPa, 0.008 at 45 kPa)	0.02
30 °C and water partial pressure of 4 kPa	Ω cm <sup>2</sup>	0.018	0.03
-20 °C	Ω cm <sup>2</sup>	0.2	0.2
Maximum oxygen crossover	mA cm <sup>-2</sup>	0.6	2
Maximum hydrogen crossover	mA cm <sup>-2</sup>	1.9	2
Minimum electrical resistance	Ω cm <sup>2</sup>	1635	1000
<i>Durability</i>			
Mechanical	Cycles w/<10 sccm crossover	24,000	20,000
Chemical	Hours with <5 mA cm <sup>-2</sup> crossover or <20% loss in OCV	614	500
Combined chemical/mechanical	Cycles until <5 mA cm <sup>-2</sup> crossover or <20% loss in OCV	Not tested	20,000
<i>Bipolar Plates</i>			
Plate weight	Kg kW <sup>-1</sup>	<0.4	0.18
Plate H <sub>2</sub> permeation	Std cm <sup>3</sup> s <sup>-1</sup> cm <sup>-2</sup> Pa <sup>-1</sup> @80 °C, 3 atm 100% relative humidity (RH)	<2 × 10 <sup>-6</sup>	2 × 10 <sup>-6</sup>
Corrosion anode	μA cm <sup>-2</sup>	No active peak	<1 and no active peak
Corrosion cathode	μA cm <sup>-2</sup>	<0.1	<1
Electrical conductivity	S cm <sup>-1</sup>	>100	>100
Flexural strength	MPa	>34 (carbon plate)	>40
Forming elongation	%	20–40	40

Note that the Leverett J-function was originally developed for two-phase flow in soils. Thus, new  $P_c$ -s correlations need to be developed for fibrous GDLs [147,148]. Niu et al. [148] conducted a volume of fluids (VOF) study, indicating the Leverett J-function provides a good prediction under low pressures of 1000 and 2000 Pa but predict much smaller liquid saturations under 4000 and 6000 Pa, as shown in Fig. 10. In addition, superhydrophobicity and mixed wettability [149,150], perforated structure [151], and heterogeneity [152,153] will significantly impact liquid displacement in a porous structure. Machine learning and AI will be helpful in establishing the correlations for general or specific porous materials under various wettability and heterogeneity using the literature data obtained from experiment, pore-level modeling, and existing correlations.

Another major mechanism for liquid water transport is through the vapor-phase diffusion and phase change, driven by temperature gradients, which is conventionally referred to as heat pipe effect. In this mechanism, the vapor diffusive flux can be expressed by

$$D_g^{w,eff}(T, P)\nabla C^w = D_g^{w,eff}(T, P)\nabla C_{sat}(T) = D_g^{w,eff}(T, P)\frac{dC_{sat}}{dT}\nabla T \quad (3)$$

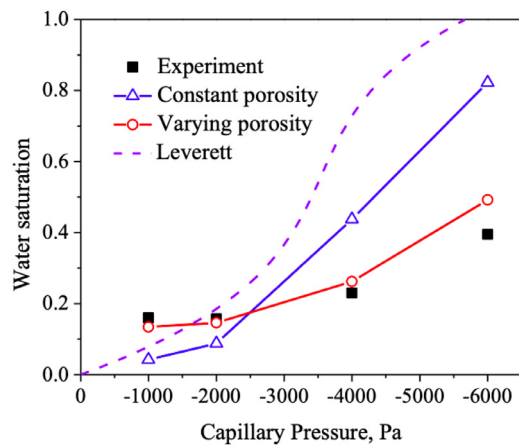
This flux can be as large as 40% of the water production rate by the ORR in a fuel cell. In addition, water vapor will diffuse toward the colder under-land region and will condense locally, thereby deteriorating the under-land flooding. A dimensionless parameter, *Damköhler* number ( $Da$ ), is defined to compare the vapor-phase diffusion with the

ORR production rates:

$$Da = \frac{\text{Rate of water production}}{\text{Rate of water removal via vapor diffusion}} = \frac{IH_{GDL}}{2FD_g^{w,eff}\Delta C^w} \quad (4)$$

where  $H_{GDL}$  is the GDL thickness,  $F$  the Faraday constant,  $I$  current density, and  $\Delta C^w$  the difference between the vapor concentrations in the CL and GFC. Wang and Chen [155] indicated that a  $Da$  of less than 1 ensures liquid water under the GFC centerline to be completely vaporized by the waste heat, leading to a highly humidified GDL region which is free of liquid water.

Fundamental models, including macroscopic and pore-level models, have been proposed to investigate two-phase flow and its impacts on fuel cell performance. The multiphase mixture ( $M^2$ ) formulation [156] is a macroscopic model that is widely adopted in PEM fuel cells [157-160]. The key idea is to focus on the level of the multiphase mixture and treat the multiple phases as constituents of a multiphase mixture. The mixture properties are defined and the governing equations of mixture variables, such as the mixture density, velocity, and species concentrations, are derived from the conservation laws. In addition, two-fluid models have been proposed as an alternative macroscopic approach, which resolves a separate liquid flow equation [139,161-164]. A phase change rate is added to each water equation of the two phases, which is determined by the interfacial area between the two phases, vapor concentration difference, and mass transfer coefficient [161,163]. In porous components of PEMFCs, this phase change rate can be assumed to be adequately rapid;



**Fig. 10.** Comparison of  $P_c$ - $s$  curves obtained from VOF simulations [148] (both constant porosity and varying porosity) with experiments [154] and standard Leverett capillary pressure function model. Operating conditions: fiber contact angle  $\theta = 109^\circ$ , 20 wt% PTFE in GDL. Parameters for the Leverett capillary pressure function model: Permeability  $K = 4.24 \times 10^{-12} \text{ m}^2$ , porosity  $\epsilon = 0.79$ , contact angle  $\theta = 109^\circ$

thus, local equilibrium applies [162]. The macroscopic method is suitable for direct coupling with other physical and electrochemical reaction kinetics to predict the fuel cell performance. To investigate the impacts of pore structure, the pore network model (PNM), lattice Boltzmann model (LBM), and VOFs have been employed to study two-phase flow by considering the detailed microstructures of GDLs and MPLs, reconstructed by either stochastic models [148,165,166] or X-ray computed tomography (CT) [154,167,168]. The PNM method involves mapping the complex pore network onto a regular or irregular lattice with local pore characteristics including size, wettability, and throat connection. A major advantage of the PNM is that it effectively incorporates important local microscopic properties of a porous medium and can analyze a sample much larger than the other two. LBM is a powerful technique for investigating transport and fluid flows involving interfacial dynamics and complex geometries. It considers a flow to be composed of a collection of pseudo-particles residing on the nodes of a lattice structure and uses distribution functions to represent the probability of finding a fluid particle [169]. LBMs are advantageous in eliminating the explicit interface tracking because of their inherent ability to incorporate particle interactions to yield phase segregation. VOF methods track the interface between two immiscible fluids by resolving an equation of the phase volume fraction  $\gamma$ : the cells fully occupied by liquid water and gas are marked as  $\gamma = 1$  and 0, respectively, while those with a phase fraction  $\gamma$  between 0 and 1 have a gas-water interface. The interfacial force is converted to a source term in the momentum equation of the cells at the interface. These pore-level methods are extremely useful to study micro/mesoscopic flow physics, impacts of material heterogeneity, and flow-microstructure correlations. However, they are usually computationally intense and difficult to couple with other physics for full-cell simulation [11].

To probe the in-situ liquid water content in PEM fuel cells, high-resolution neutron and X-ray radiographies have been employed in recent years. Neutron radiography is a promising method to detect liquid water because of the extreme sensitivity of neutron beams to water relative to other fuel cell materials. Recently, Mishler et al. [170] employed in-situ neutron radiography to quantify the liquid distribution from the inlet to outlet under various RH values, PTFE loadings in GDLs and MPLs, flow fields, and flow configurations, as shown in Fig. 11. They showed that a high water content is present at low current density under constant stoichiometry and liquid water emerges downstream at low RH and rapidly increases after the onset. Markötter et al. [171] studied 3D water distribution in PEM fuel cells using a quasi in-situ tomogra-

phy technique and analyzed water distribution after switch-off. They demonstrated that the technique enables the study of water content in individual flow fields of three-fold stacks. X-ray CT resolves the internal structure and inhomogeneity of a sample using an X-ray beam which is attenuated as it goes through the sample [172]. Flückiger et al. [154] employed synchrotron-based X-ray CT to probe the 3D distribution of liquid water in Toray carbon paper GDLs of various PTFE loadings. A resolution of  $1.48 \mu\text{m}$  was employed to distinguish the fibers and most pores in GDLs. They also analyzed liquid water distribution from 1D to 3D and the relationship between the capillary pressure and water saturation. Zenyuk et al. [167] evaluated the porosity, tortuosity, and PSD of a large set of commercially available GDLs under varying compression. They observed bimodal PSDs for most of the GDLs, which approach unimodal distributions under high compression, and also indicated that a domain of  $1 \times 1 \text{ mm}$  in-plane and full thickness in through-plane directions accurately represents GDL properties. Fishman et al. [168] studied the spatially varying porosity in GDLs, which was input to a PEMFC model to study its impact on liquid water distribution [153]. Ge et al. [173] observed liquid water breakthrough events in crack-free MPLs using in-situ synchrotron X-ray radiography. They also measured water thicknesses, which were used as input for 1D model analysis.

The two-phase flow images and results can be analyzed using machine learning and AI, as proposed by Raissi et al. [174] for general fluid problems. They developed hidden fluid mechanics (HFM), a physics-informed deep-learning framework, to encode the Navier-Stokes equations into neural networks. Fig. 12 displays the flow contours over a liquid droplet in a GFC and fluid flows predicted by HFM machine learning. In addition, AI technology can help improve the current 3D two-phase models of PEM fuel cells via machine learning of visualization data and VOF/LBM simulation results. The mechanisms of two-phase flow and associated dimensionless parameters can be input for a physics-informed deep-learning framework to encode the flow equations, droplet dynamics, and capillary action into the neural networks.

### 3.3. Dynamic operation

Dynamic operation is frequently encountered in applications of portables and FCEVs. For example, startup operation requires a PEM fuel cell to operate and increase its temperature from room to operating temperature (usually  $\sim 80^\circ\text{C}$ ) within minutes, during which both the thermal and water conditions will greatly change [94,176]. In addition, power loss has been observed during transience due to temporary dehydration of the anode [177]. The reaction rate or current density may undergo undershoot due to delays in oxygen supply to the cathode CL [178].

In PEM fuel cells, dynamic operation is affected by various multi-timescale processes, including charging/discharging of the electrochemical double-layer at the reaction interface (with a time constant of  $\tau_{dl} = \delta_{CL}^2 aC(1/\kappa + 1/\sigma)$ ), gaseous reactant diffusion in GDLs, MPLs, and CLs (e.g.  $\tau_D = \delta_{GDL}^2 / D_g^{eff}$ ), membrane water dynamics including diffusion, electroosmosis drag, and storage ( $\tau_m = \frac{\rho_m \Delta \lambda}{EW} / \frac{I}{2F}$ ) [178,179], phase change [180,181], and liquid drainage in GFCs [182,183]. In terms of timescale, the former two take place fairly fast at a timescale of less than 0.1 s. Water dynamics in the Nafion<sup>®</sup> membrane varies greatly in timescale ranged from 0 to 100 s. The time constants of phase change and liquid drainage are dependent on the specific process. These time constants characterize the response of each physical process and together shape the multi-timescale characteristics of PEMFC systems. Fundamental analysis of the time constants is also important to explain fuel cell signals observed in practice and reduce noises and develop machine learning schemes to predict dynamic behaviors and optimize control strategy.

One of the most complex phenomena in PEM fuel cells is transient operation involving non-isothermal two-phase flow and hence the heat



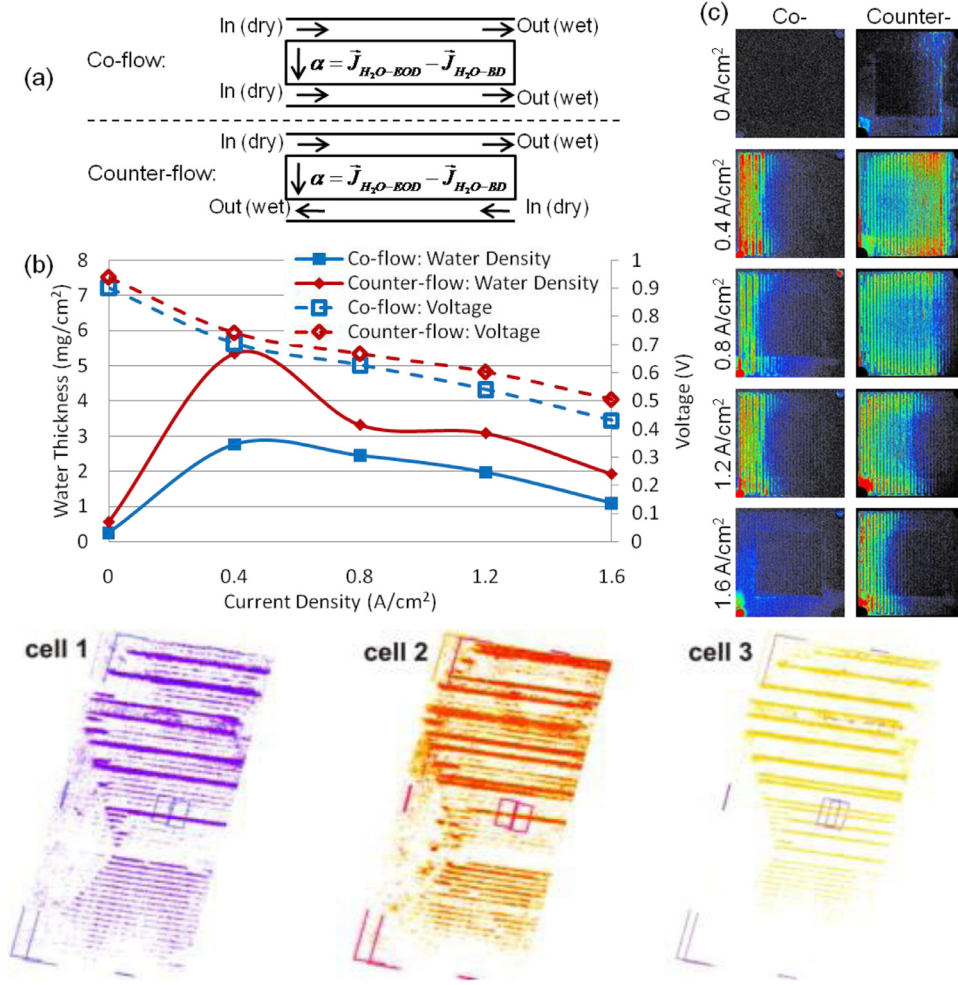


Fig. 11. (above) Water thickness and performance of a PEM fuel cell with a serpentine-flow field at 50% inlet RH and the corresponding colored neutron images [170]; (below) separated water distribution for each single cell in a three-cell stack [171].

release/absorption during water condensation/evaporation  $S_{fg}$ :

$$S_{fg} = h_{fg} \dot{m}_{fg} \text{ and } \dot{m}_{fg} = \rho_l \frac{\partial s}{\partial t} + \nabla \cdot (\rho_l \vec{u}_l) \quad (5)$$

where  $h_{fg}$  is the latent heat of vapor-liquid phase change and  $\dot{m}_{fg}$  is the phase change rate. A practical operation is the dry gas purge technique to remove excess liquid water for electrode flooding mitigation. In this operation, excess water in GDLs and the membrane will be vaporized by dry reactants. Wang and Wang [181] elucidated four de-wetting processes and corresponding output voltage responses in the ohmic polarization regime. They delineated the GDL de-wetting by two through- and in-plane processes, as shown in Fig. 13(a) and mathematically derived the evolution of the vaporization fronts. It was shown that these two elementary processes follow the same equation after normalization. Schneider et al. [183] conducted I-distribution measurements and in-plane neutron radiography in voltage step experiments to investigate the local flooding and cell performance, as shown in Fig. 13(b). They indicated that oxygen depletion leads to a strong performance loss under the ribs before the onset of notable liquid water accumulation. Their results also indicated a timescale of 10–100 s for water buildup in the fuel cell, consistent with the time constant analysis. Cho et al. [184,185] investigated the effects of MPL and GDL design on PEMFC transient responses. Their results showed that the transient response is determined by the capillary pressure gradient through GDLs. The trade-off relation for PEMFC performance under low and high RHs is mitigated by designing a reverse capillary pressure gradient in MPLs. As to machine learning, dynamic operation of PEMFCs and real-time monitoring will generate a large amount of data, which is suitable for machine learning and

AI to design proper control strategies to achieve load demand and quick startup, optimize efficiency and performance, and mitigate degradation. The physics of two-phase transient, membrane hydration/dehydration, time constants, transport dynamics, and electrochemical double-layer behaviors can be encoded to the neural networks for effective deep learning.

### 3.4. Cold start

PEM fuel cells must be able to survive and startup from subfreezing temperatures, also called cold start, for the FCEV application [186–188]. In freezing environments, water product has a tendency to freeze in the cathode CL, making it difficult to remove and thus creating mass transport limitation which may eventually end the ability for operation. In practice, the capability of unassisted cold-start is determined by two competing processes governed by the fuel cell's water/heat co-production, namely ice production to occupy the cathode CL pores (with a time constant  $\tau_{s_{ice}} = \frac{2F\delta_{CL}}{(1+2\alpha)I} (\frac{\rho_m \epsilon_m (14-\lambda_0)}{EW} + \frac{\epsilon_{CL} \rho_{ice}}{M^w})$ ) and PEMFC temperature increase to overcome 0 °C ( $\tau_{T,1} = \frac{\rho_{BP} C_{pBP} \delta_{BP}}{I(E_o - V_{cell})} (273.15 - T_o)$ ). The ratio of the two time constants,  $\beta_2 = \frac{\tau_{T,1}}{\tau_{s_{ice}}}$ , then provides a basic criterion to evaluate the cold-start capability, which are determined by the PEMFC design and operation condition [189]. In general, a large CL thickness ( $\delta_{CL}$ ), ionomer fraction ( $\epsilon_m$ ), porosity ( $\epsilon_{CL}$ ), or small BP thickness ( $\delta_{BP}$ ) and thermal capacity ( $\rho_{BP} C_{pBP}$ ) help cold-start capability. In addition, supercooled water under subfreezing conditions was observed to flow to GDL and GFC, which will benefit cold-start capability. Ko et al.



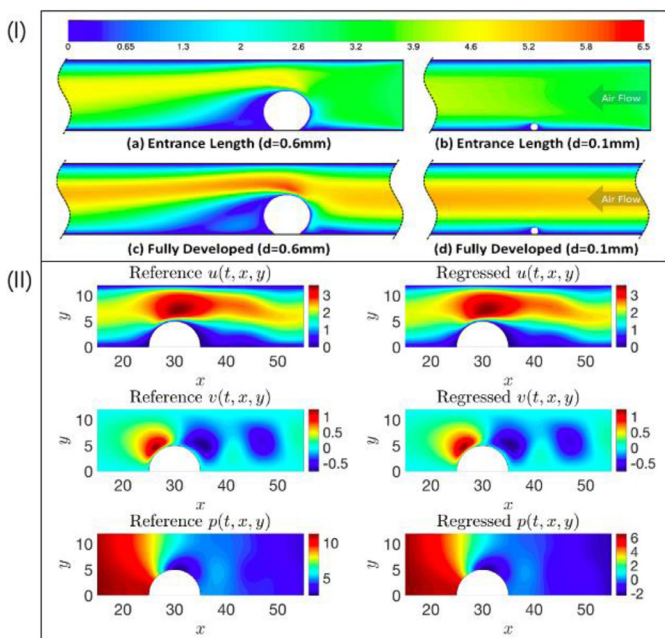


Fig. 12. (I) Velocity contours of flow over a liquid droplet at the GDL surface in a GFC at an inlet velocity of 3.0 m/s [137,138,175] [RR16]; (II) 2D channel flow over an obstacle using machine learning: the outputs from the regressed velocity  $u$  and  $v$  and pressure  $p$  fields shown on the right column. Reference velocity and pressure fields are plotted for comparison on the left column [174]. Note that the flow directions are opposite in (I) and (II).

[190] proposed using part of the cathode MPL for the ORR to improve cold-start capability.

In cold start, ice formation may vary spatially in PEMFCs, even across a thin CL [178,191-193]. Analysis of the non-uniformity factor  $\tilde{h}$  of the reaction indicated that the ORR rate considerably varies in a CL from

the membrane to GDL sides under subfreezing temperature because of the small ionic conductivity of membranes, as given by the following correlation for  $-30-0^\circ\text{C}$ :

$$\sigma_m = (0.01862\lambda - 0.02854) \exp \left[ 4029 \left( \frac{1}{303} - \frac{1}{T} \right) \right] \text{ for } \lambda \leq 7.22 \quad (6)$$

$$\sigma_m = \sigma_m(\lambda = 7.22) \text{ for } \lambda > 7.22$$

For a water content  $\lambda > 7.22$ , part of the water in the ionomer phase freezes and thus makes little contribution to the ionic conductivity. In practice or CL design, the number of coulombs of charge  $Q_c$  transferred before the output voltage drops to 0.0 V was introduced as a measure of cold-start capability [105,188]. CL composition, cold-start temperature, membrane hydration, and CL thickness all affect this parameter.

At the electrocatalyst surface, ice formation may follow two consequent morphologies—initial isolated ice nucleates and then film formation, as depicted by Fig. 14. The former imposes a much less impact on the catalyst activity than the latter. In addition, two major mechanisms are proposed for the effects of ice on the ORR activities — catalyst surface coverage and oxygen diffusion resistance [189,194,195]. Furthermore, it has been proposed that ice formation in CLs is fundamentally similar to LiOx deposit in lithium-air batteries [196,197] in terms of impacts on both surface coverage and oxygen diffusion on the ORR reaction. Two regimes are defined in both fuel cell [198] and battery [199,200], based on the dominant mechanism of voltage loss. Fig. 14 shows the evolutions of PEMFC voltages and HFR under subfreezing operation. The initial sharp drops are the starting points which impose the electric load, and the output voltage decreases initially, which is dominated by the catalyst surface coverage by ice product, followed by a fast drop which is dominated by oxygen blockage due to ice formation in pores. Du et al. [201] indicated that under the maximum power mode, the cold-start current density is at high levels and the performance improvement caused by membrane hydration and temperature increment may not be observable. Therefore, before the melting point, the performance drops continuously. Another critical issue related to cold start is CL degradation including the electrochemical surface area (ECSA) loss. GDLs may lose their hydrophobicity and break the fiber

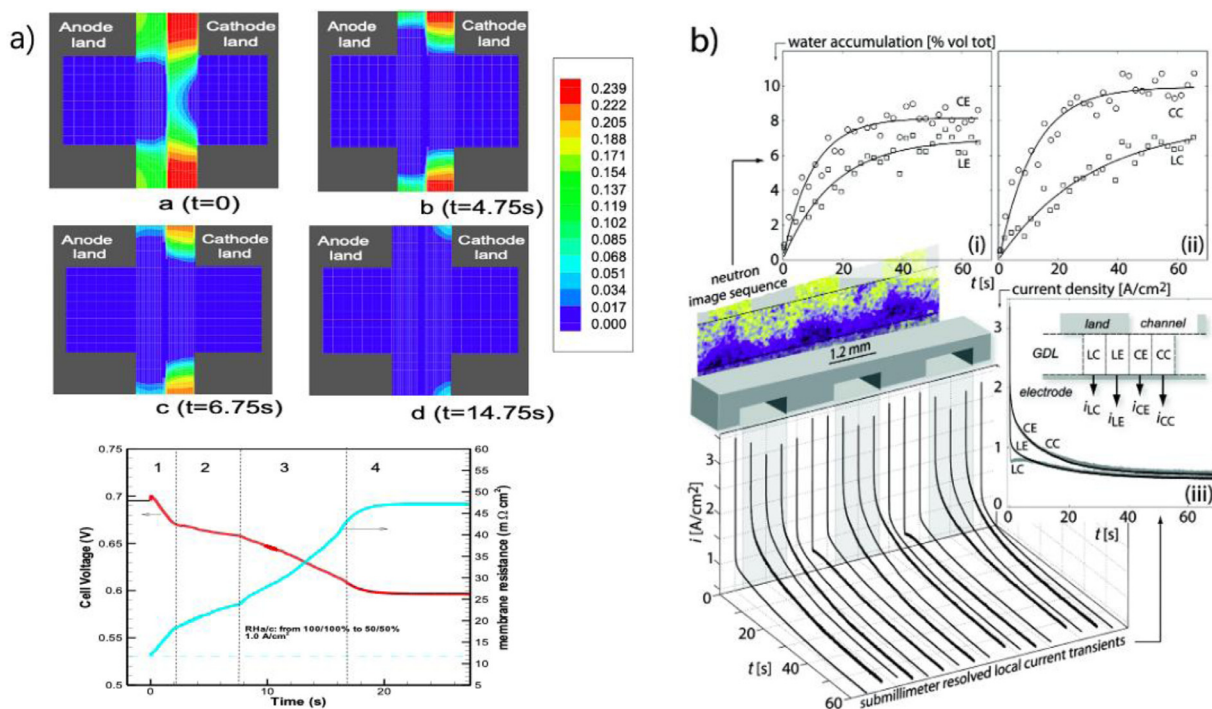


Fig. 13. (a) GDL de-wetting in a PEM fuel cell: (above) evolution of liquid saturation distribution; (below) responses of output cell voltage and membrane ionic resistance [181]; (b) characteristic positions of the cathode flow field used for the evaluation of (i, ii) local water accumulation and (iii) local current density [183].

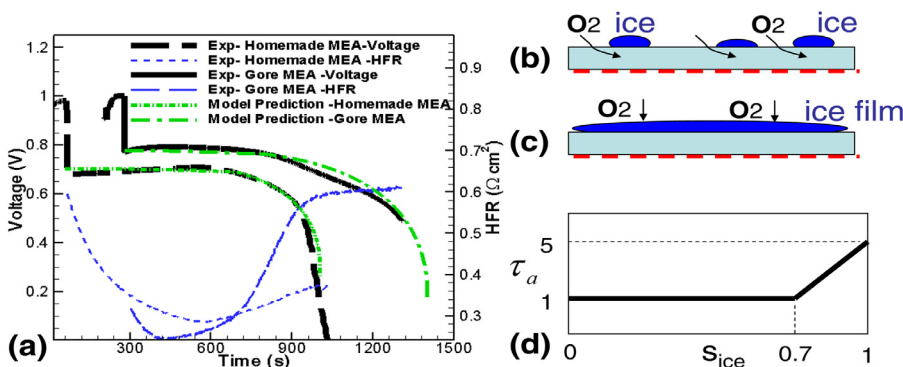


Fig. 14. (a) Evolution of PEMFC output voltage and HFR under 0.02 A/cm<sup>2</sup> and -10 °C; (b) ice nucleation at the ionomer film covering the catalyst (dashed line); (c) connection of ice islands, forming a thin ice film and blocking the access to oxygen underneath catalyst; and (d) the ice surface coverage factor  $\tau_a$  to describe the two mechanisms; the ice film formation starts at  $s_{ice}=0.7$  [198].

linkage during freeze/thaw cycles [202]. Similarly, machine learning can be applied to predict ice formation, ice volume content, and temperature status during cold start by encoding the ORR kinetics, ice morphology and impacts at the reaction surface, ionic conductivity at freezing temperature, and time constants to the neural networks. The physics-informed deep learning will facilitate the development of proper control strategies, including external heating, for successful degradation-free cold-starts from various complex environments in practice.

### 3.5. Durability

Further development of PEM fuel cells requires not only cost reduction, but also durability improvement. Durability is usually measured in terms of the voltage loss per hour under a fixed current, which is directly attributed to fuel cell material degradation. It is usually associated with the electrochemical, mechanical, and chemical stability of its components, specifically, the MEAs. The electrochemical/chemical degradation is mainly associated with catalyst dissolution or ripening, carbon oxidation, and attack by radicals or ionic species; mechanical degradation results from a mechanical stressor, such as cyclic compression, material expansion, or membrane crack formation. ECSA loss is frequently used to measure the degradation of electrocatalyst activity caused by catalyst ripening/instability and carbon support corrosion [112]. PEMFC degradation often occurs over a long period of time and is therefore expensive to investigate experimentally. ASTs are usually defined, following DOE protocols, to investigate material durability in a relatively short period of time [203]. PEMFC durability has been reviewed extensively in the literature [95,204,205].

For membranes, chemical degradation is often due to attacks by radicals or ionic species; mechanical failure originates from changes in the membrane structure, such as pinhole formation and crystallinity change. Cyclic hydration/dehydration and compression of a fuel cell over its lifetime are the main causes of membranes losing their structural integrity. Pinhole formation, due to cyclic membrane shrinkage and swelling, causes crossover of reactant gasses. Degradation due to chemical stresses may reduce proton conductivity or membrane thickness, which promotes crossover of reactant gasses. Chemical degradation is often caused by formation of attacking species that damage the membrane structure. Carboxylic acid and other H-containing end groups can form during membrane polymerization or as a result of a chemical reaction, and are usually vulnerable to attack [206,207]. Hence, degradation can occur due to free radical attack on the reactive end groups [208,209]. The attack eventually leads to membrane unzipping and conductivity loss. In addition, presence of cation impurities may reduce proton conductivity because the sulfonic sites have a higher affinity to foreign cations than H<sup>+</sup> [210]. These ions catalyze hydrogen peroxide following the reactions in Eqs. (7)-(10) to form different types of radicals [211-213].

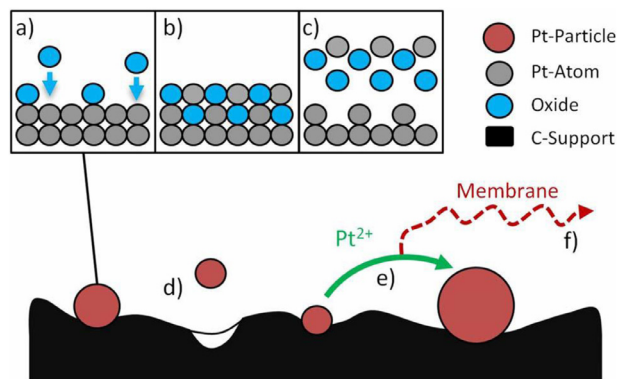
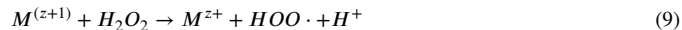
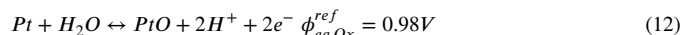


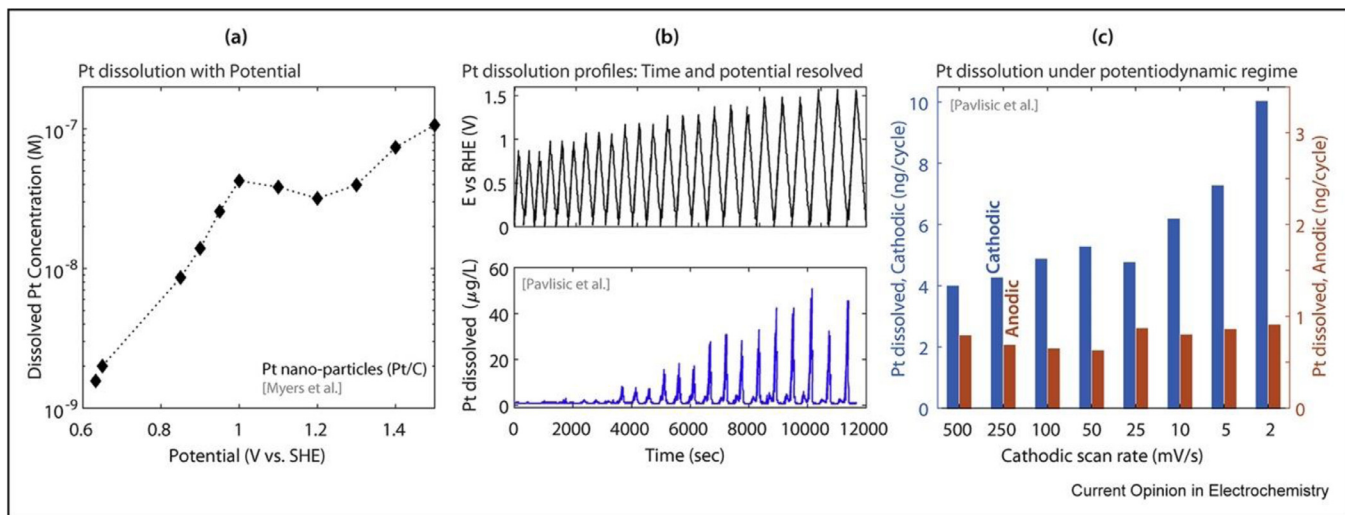
Fig. 15. Pt degradation mechanisms: (a) Pt oxidation and PtO surface coverage, (b) Place exchange between Pt lattice and adsorbed O atoms, (c) Oxide reduction and cathodic dissolution of exchanged Pt, (d) Carbon corrosion, (e) Electrochemical Ostwald ripening, (f) Pt<sup>2+</sup> ion dissolution into the membrane [112].



The effect of single cations on degradation from high to low is: Fe > Cu > Cr > Al, with iron having the highest catalytic effect on radical formation [211, 212,214]. This type of degradation is often investigated ex-situ by the Fenton test [212,215] or peroxide vapor test [97].

Electrochemical degradation is mainly governed by ECSA loss due to electrocatalyst and/or carbon support degradation. Electrocatalyst morphology changes are the main driver for this kind of degradation, and may be associated with dynamic operation, for example, the cathode potential cycles between 0.6 V and 0.95 V or rises temporarily above 1.35 V during startup and shutdown [204]. Under such conditions, Pt becomes electrochemically unstable and may be subject to dissolution. As the potential voltage increases, Pt<sup>2+</sup> ions dissolve from the cathode CL into the electrolyte. They can diffuse into the membrane because of the increasing concentration gradient, preventing re-deposition in the CL. A high potential voltage may lead to carbon support corrosion. In addition, Pt oxidation may occur, as shown in Fig. 15 and Eqs. (11)-(13), which list a few main Pt degradation mechanisms.





**Fig. 16.** (a) Steady-state concentration of dissolved Pt as a function of potential for Pt nanoparticles (Pt/C), (b) Pt dissolution profiles: time and potential-resolved dissolution profiles of 3 nm Pt catalyst (experimental conditions: 0.1 M HClO<sub>4</sub>, potential window: 0.05 to different UPL (0.9 V–1.6 V), scan rate: 5 mV/s), (c) Pt dissolution for cathodic and anodic portions of potential cycle as a function of cathodic scan rate (potential window: 0.05 V–1.6 V) [217].

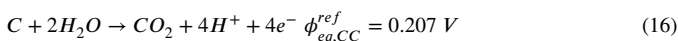


The ECSA loss due to Pt dissolution is mainly associated with a PSD change of electrocatalyst particles, which occurs via four main mechanisms: (i) Pt grain migration on the carbon support, (ii) Pt dissolution and re-deposit on larger particles (Ostwald ripening), (iii) Pt dissolution and migration into the membrane, and (iv) detachment of Pt particles due to carbon corrosion [206–216].

Another mechanism of Pt dissolution is place exchange [218], as shown in Fig. 15(b). During the anodic Pt dissolution in Eq. (11), an oxide layer forms on the catalyst, which reduces the Pt dissolution rate. A further increase in the voltage potential or holding the potential constant for a sufficient period of time subjects the adsorbed oxygen atoms to place exchange from the surface to sub-surface positions. The place exchange exposes the Pt atoms and permits the absorption of new oxides. In the place exchange process, oxides penetrate the Pt lattice [218]. Thus, subsequent potential sweeps not only reduce the formed oxides, but also lead to the cathodic dissolution of the exchanged Pt. The place exchange mechanism is described in Eqs. (14) and (15).



Fig. 16 shows the dissolved Pt concentration and rate as a function of the potential and cathodic scan rate. In the event of jump to a high potential, such as in startup/shutdown operation, carbon corrosion may occur, leading to losses of the electrical conductivity and supported Pt catalyst [219]. The dissolution mechanism follows Eq. (16) [107],



Pt dissolution and carbon support corrosion will cause changes in the CL microstructure and thickness. Fig. 17 shows SEM images of the CLs in the Mirai FCV after AST testing, indicative of a significant decrease in the CL thickness after the carbon support AST testing (c).

## 4. Machine learning in PEMFC development

### 4.1. Machine learning overview

Machine learning, an important area in artificial intelligence (AI), is a scientific discipline involving algorithms that learn from data. The

learning process occurs as the program forms a pattern from existing data that is then valid for new data. Machine learning has been applied to promote new technologies, such as image recognition, natural language processing, and autopiloting, and is used to reexamine traditional disciplines for revolutionary changes. According to learning style, machine learning algorithms can be generally classified into three types: supervised learning, unsupervised learning, and reinforcement learning, as shown in Table 9. Owing to its accuracy and efficiency, supervised learning is commonly used in energy-related fields [221–224]. Table 10 lists popular supervised learning algorithms and their characteristics. Unsupervised learning algorithms, such as principal component analysis (PCA), singular value decomposition (SVD), and k-means clustering, are also used in energy and material studies.

Among many machine learning methods, the rapid development of deep learning in recent years has pushed it to the forefront of the field of AI. Deep learning is the ANN with deep structures or multi-hidden layers [229–232]. It can achieve good performance with the support of big data and complex physics, and has a much simpler mathematical form than many traditional machine learning algorithms. The relationship between AI, machine learning, and deep learning is shown in Fig. 2, along with the number of US patent applications per year [20]. We can expect that deep learning, such as physics-informed learning, will become the most important path to AI. However, deep learning relies on big data, and thus traditional machine learning still has strong applications, especially for interdisciplinary studies, and can solve problems with reasonable amounts of data. Many open-source machine learning frameworks have been developed and made available to the general public, including Scikit-Learn, Caffe2, H2O, PyTorch (for neural networks), TensorFlow (for neural networks), and Keras (for neural networks).

### 4.2. Machine learning for performance prediction

PEMFC performance is characterized by the polarization curve, also called the I-V curve, which is determined by a number of factors including fuel cell dimensions, material properties, operation conditions, and electrochemical/physical processes [233–236]. Various physical models and experimental methods have been proposed to predict or directly measure the I-V curve, which are reviewed by many other works [158,160,202,237]. As an alternative approach, machine learning is capable of establishing the relationship between inputs and output performance through proper training of existing data, as shown in Fig. 18.



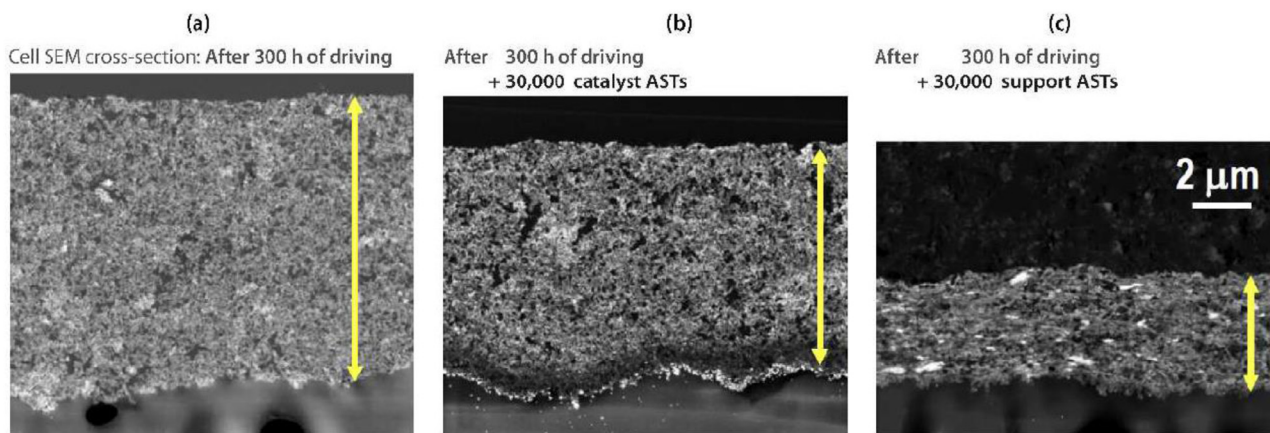


Fig. 17. SEM cross-section images of cells from a Toyota Mirai after (a) 300 h of driving, (b) 300 h of driving + 30,000 catalyst ASTs, and (c) 300 h of driving + 30,000 support ASTs [220].

Table 9  
Characteristics and typical tasks of supervised learning, unsupervised learning, and reinforcement learning.

	Characteristics	Typical tasks
<b>Supervised learning</b>	Dataset is labeled with input and output as ‘feature’ and ‘label’. Its algorithms generally aim to train the mapping between input and output. The obtained pattern can predict the “label” of new data from the “feature”. Dataset is not labeled.	<b>Regression:</b> The predictive output is a continuous value. <b>Classification:</b> The predictive output is discrete.
<b>Unsupervised learning</b>	Its algorithms are used to address problems impossible to manually label data due to lack of prior knowledge or cost.	<b>Clustering:</b> Samples of similar features are grouped to form clusters. <b>Dimensionality reduction:</b> Core features are collected and redundant information is reduced.
<b>Reinforcement learning</b>	It trains an agent by reward or punishment for a state change and interaction with the environment, allowing the agent to decide the best next action to maximize the reward.	<b>Q-learning:</b> It is a “model-free” algorithm, and can handle problems with stochastic transitions and rewards without requiring adaptations.

Table 10  
Popular supervised learning algorithms and characteristics [225-228].

Algorithms	Characteristics
Linear regression	It fits a linear model based on ordinary least squares. It is the common benchmark algorithm to evaluate the prediction performance of other regression algorithms.
k-nearest neighbor (kNN)	It is a simple algorithm that classifies a new point by a majority vote of its k nearest neighbors in the available dataset.
Logistic regression	It is a linear model for classification rather than regression, especially binary classification. A logistic function is used to calculate the probability of a single trail.
Decision tree	It can learn simple decision rules from data features to predict targets. It can solve both regression and classification problems.
Naïve Bayes	It is based on Bayes’ theorem with the assumption of conditional independence between the features.
Support vector machine (SVM)	It is based on the Vapnik-Chervonenkis dimension and structural risk minimization in statistical theory. It aims to construct the hyperplane in a high-dimensional space to classify the samples. It can solve regression problems, usually known as support vector regression.
Gaussian process	A generic supervised learning algorithm that can solve both regression and classification problems.
Artificial neural network (ANN)	It is based on modern neuroscience to process information by simulating the neural network processing in organic brains. Its structure is multi-layer perceptron, consisting of a large number of connected neurons.

Mehrpooya et al. [233] experimentally constructed a database of PEMFC performance under various inlet humidity, temperature, and oxygen and hydrogen flow rates. A two-hidden-layer ANN was then trained using the database to predict the performance under new conditions. Total 460 points are contained in the database with 400 for training and 60 for testing, and  $R^2$  of 0.982 (for the training) and 0.9723 (for the test) was achieved in their study. Han and Chung [234] developed data-driven models using ANN and SVM to predict fuel cell performance and compare their predictions, as shown in Fig. 19. Both models showed acceptable fitting with  $R^2 > 0.98$ , with the ANN performing better based on their database. Kheirandish et al. [235, 236, 238] compared ANN, SVM, and Hebbian learning algorithms using their database of the stack voltage and efficiency. They showed that all outperformed the linear regression with the SVM better than ANN. For regression tasks using a small database in a range of 100 s to 1000s data points, the ANN and SVM

are the most common algorithms for data-driven models, and generally show acceptable prediction for studying fuel cell performance.

In addition to steady-state performance, Chavez-Ramirez et al. [239] investigated the dynamics of PEM fuel cell using a two-hidden-layer ANN with experimental database. Bicer et al. [240] generated a database from the Matlab simulation of a physics-based model to train their two-hidden-layer ANN to predict fuel cell dynamics. Although predicting dynamic performance under various conditions, they ignored the time-series characteristics of the dynamic data with the inputs including only operating conditions without time. Thus, they only predicted the relationship between performance and operating conditions at a specific time, and no dynamic behaviors were analyzed. Using time-series data and proper algorithms for machine learning is still highly desirable for predicting/analyzing PEMFC dynamics and developing control strategies.



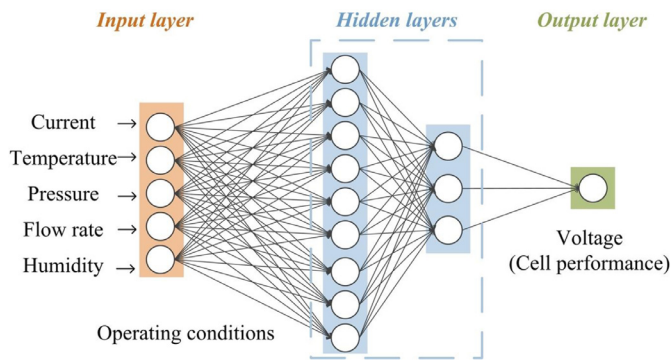


Fig. 18. ANN structure between inputs (operating conditions, including anode and cathode relative humidity (RH), temperature, current, and pressure, as examples) and output (fuel cell voltage).

Unlike physical models, the mapping between inputs and outputs constructed by machine learning models does not follow an actual physical process; thus, the machine learning approach is also called the black-box model. Machine learning has unique advantages in PEMFC modeling, which requires no prior knowledge, especially of the complex coupled transport and electrochemical processes occurring in PEMFC operation. This significantly reduces the level of modeling difficulty and also makes it possible to take into account any processes in which the physical mechanisms are not yet known or formulated. The machine learning method is also advantageous in terms of computational efficiency in the implementation process after proper training. This characteristic makes machine learning potentially extremely important in the practical PEMFC applications which usually involve a large-size multiple-cell system, dynamic variation, and long-term operation. For a complex physical model that takes multi-physics into account, the computational and time costs are usually too high; a simplified physical model lacks of high prediction accuracy. For even a small-scale stack of 5–10 cells, physics-model-based 3D simulation usually requires 10–100 million gridpoints and takes days or weeks for predicting one case of steady-state operation [158,160,241]. In this regard, machine learning could greatly help to broaden the application of complex physical models by leveraging on prediction accuracy and computational efficiency. Using the simulation data from complex physical models to train a machine learning model is a popular approach, usually referred to as surrogate modeling. A surrogate model can replace the complex physical model with similar prediction accuracy but higher computational efficiency. Wang et al. [242] developed a 3D fuel cell model with a CL agglomerate sub-model to construct a database of the PEMFC performance with various CL compositions. A data-driven surrogate model based on the SVM was then trained using the database, which exhibited comparable prediction capability to the original physical model with several-order higher com-

putational efficiency. It only took a second to predict an I-V curve using the surrogate model versus hundreds of processor-hours using the 3D physics-based model. Owing to its computational efficiency of the surrogate model, the surrogate model, coupled with a generic algorithm (GA), is suitable for CL composition optimization. Similarly, Khajeh-Hosseini-Dalasm et al. [243] combined a CL physical model and ANN to develop a surrogate model to predict the cathode CL performance and activation overpotential. For fast prediction of the multi-physics state of PEM fuel cell, Wang et al. [244] developed a data-driven digital twinning framework, as shown in Fig. 20. A database of temperature, gas reactant, and water content fields in a PEM fuel cell under various operating conditions was constructed using a 3D physical model. Both ANN and SVM were used to solve the multi-physics data with spatial distribution characteristics. The data-driven digital twinning framework mirrored the distribution characteristics of multi-physics fields, and ANN and SVM exhibited different prediction performances on different physics fields.

Application of machine learning in PEMFC performance prediction has many distinct advantages, and it will continue to be popular in the PEMFC community. However, as it does not require physical representation, skepticism remains that it may lose efficacy in scenarios that are not included in the test data set. Developing a hybrid model that combines physical process and machine learning, and encoding physical mechanisms into machine learning would improve the predictions of fuel cell performance, dynamic behaviors, and physical state in complex scenarios. There is a great potential to improve the current two-phase models (e.g. the two-fluid and mixture approaches) of PEM fuel cells by using AI technology, for example, machine learning analysis of visualization data and VOF/LBM simulation results. Physics-informed neural networks were recently proposed by Raissi et al. [174], known as hidden fluid mechanics (HFM), to encode the Navier-Stokes (NS) equation into deep learning for analyzing fluid flow images, as shown in Fig. 21. Such a strategy can be extended to the deep learning of two-phase flow and fuel cell performance by incorporating relevant physics, such as the capillary pressure correlation, Darcy's law, and the Butler-Volmer equation, into the neural networks. Table 11 summarizes the main physics in each PEMFC component that deep learning can incorporate to effectively achieve the design targets.

#### 4.3. Machine learning for material selection

Machine learning is widely used in the chemistry and material communities to discover new material properties and develop next-generation materials [245–247]. Experimental measurement, characterization and theoretical calculation are main traditional methods to diagnose or predict the properties of a material, which are usually expensive in terms of cost, time, and computational resources. Material properties are influenced by many intricate factors, which increases the difficulty level in the search for optimal material synthesis using only traditional methods. Machine learning can assist in material selection

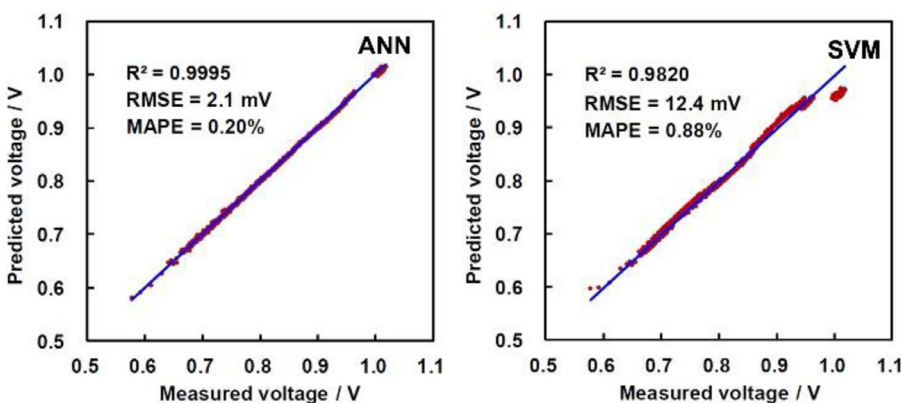


Fig. 19. Comparison of experimental database and ANN/SVM predictions [234].

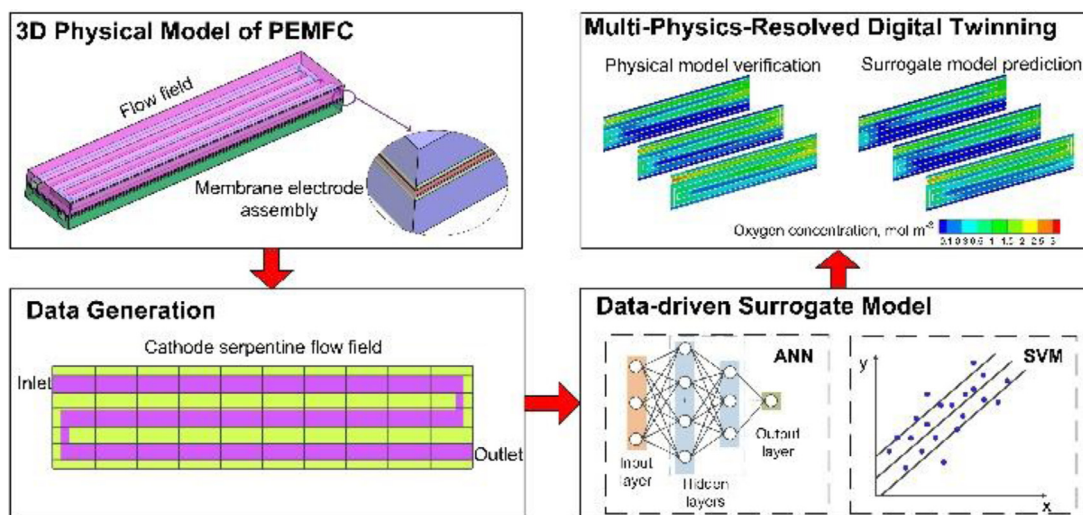


Fig. 20. Workflow of data-driven digital twinning framework [244].

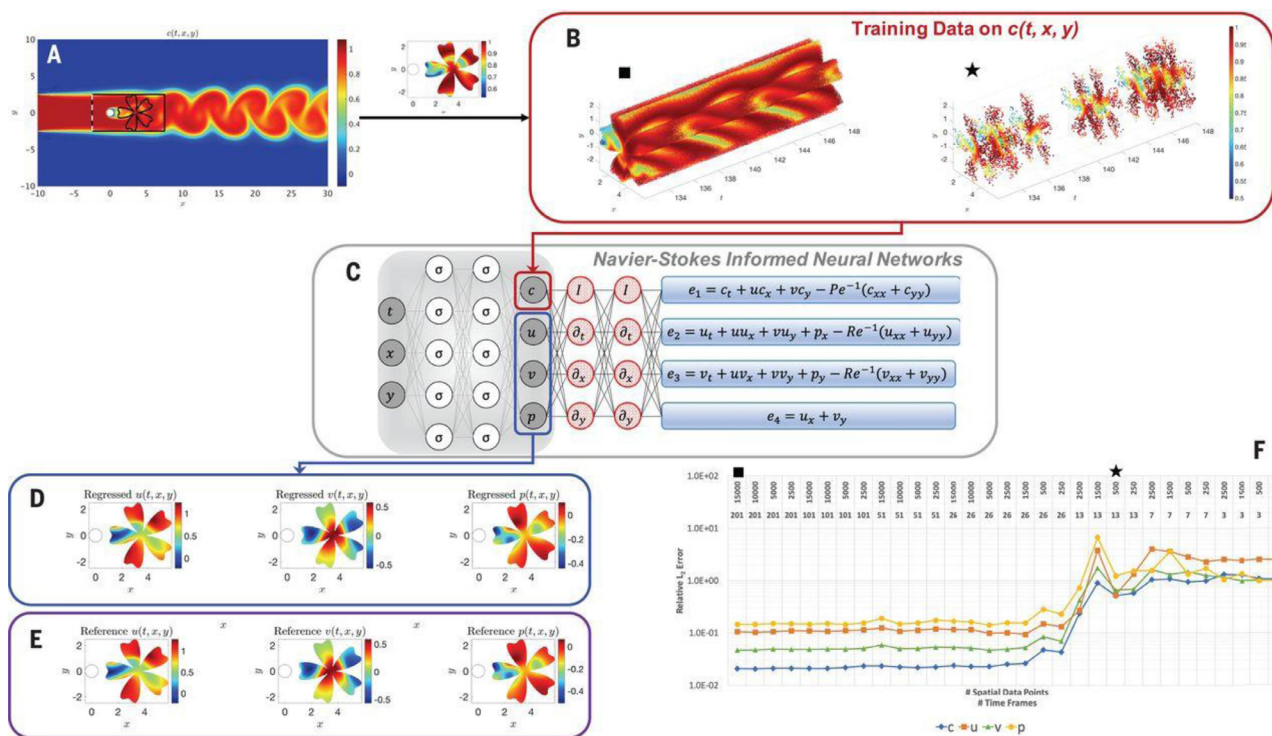


Fig. 21. Arbitrary training domain in the wake of a cylinder using Navier-Stokes (NS)-informed neural networks [174]: (A) Domain generating training data for concentration and reference data for velocity and pressure using direct numerical simulation. (B) Training data on concentration  $c(t, x, y)$  in an arbitrary domain in the shape of a flower located in the wake of the cylinder. The solid black square corresponds to a very refined point cloud of data, and the solid black star corresponds to a low-resolution point cloud. (C) A physics-uninformed neural network (left) takes the input variables  $t, x,$  and  $y$  and outputs  $c, u, v,$  and  $p$ . By applying automatic differentiation on the output variables, the transport and NS equations are encoded in the physics-informed neural networks  $e_i, i = 1, \dots, 4$  (right). (D) Velocity and pressure fields regressed by means of hidden fluid mechanics (HFM). (E) Reference velocity and pressure fields obtained by removing the arbitrary domain in (A), used for testing the performance of HFM. (F) Relative  $L_2$  errors estimated for various spatiotemporal resolutions of observations for  $c$ . On the top line, the spatial resolution for each case is listed; on the line below, the corresponding temporal resolution over 2.5 vortex shedding cycles is listed.

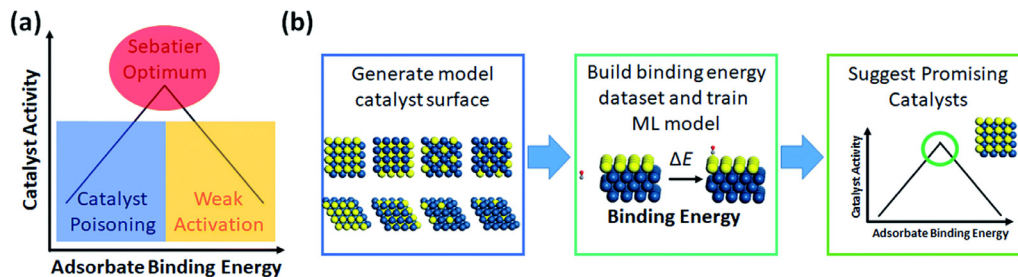
and property prediction using existing databases, which is advantageous in taking into account unknown physics and greatly increasing the efficiency. As example, in the catalyst design absorbate binding energy prediction by the empirical Sabatier principle is widely used for the optimization of activity in catalyst design (Fig. 22(a)) [247]. To remove the empirical equation, a database of binding energy for different catalyst structures constructed by characterization or theoretical calculation is used to train a machine learning model, which shows a great efficiency

in predicting the catalyst activity in a wide range to identify the optimal solution of the catalyst structure (Fig. 22(b)) [247]. Owing to the great potentials of machine learning in chemistry and materials science, professional tools have been developed, along with universal machine learning frameworks, and numerous structure and property databases for molecules and solids can be easily accessed to model training. Popular professional machine learning tools and databases are summarized in Table 12 [224].

**Table 11**  
Major physics in PEM fuel cell for physics-informed machine learning.

Component	Major Physics for Machine Learning	Design/Material Targets
PEM	Ion transport (i). Water transport and uptake and dynamics (ii). Subfreezing performance (ix). PEM degradation mechanisms (x). H <sub>2</sub> , O <sub>2</sub> , or N <sub>2</sub> transport (iv)	Improve durability, ionic conductivity, and mechanical robustness. Reduce cost and water dependence of ionic conductivity, and reduce cross-overs of H <sub>2</sub> , O <sub>2</sub> , and N <sub>2</sub> .
CL	Ion transport (i). Electrochemical reaction kinetics (iii). Oxygen/hydrogen transport in both pores and ionomer film (iv). Ice formation (ii), (viii). Electrocatalyst degradation mechanisms (x). Two-phase flow (ii), (vii), (viii).	Reduce PMG electrocatalyst loading and carbon corrosion. Improve electrocatalyst stability and durability, CL performance, water removal, oxygen transport, proton conductivity, and cold-start capability.
GDL/MPL	Two-phase flow (ii), (vii), (viii). Species transport (iv). Heat transfer (v), (viii). Electric current conduction (vi). Phase change and heat pipe effects (ii), (viii).	Improve water and thermal management. Reduce electric ohmic loss and gaseous reactant transport resistance.
GFCs	Two-phase flow (ii), (vii), (viii). Droplet dynamics at GDL surface (vii). Heat transfer/electric current conduction for porous media flow fields (v), (viii)/(vi).	Evenly distribute gaseous reactants. Mitigate fuel cell flooding. Reduce pumping power loss.
BPs	Heat transfer (v). Electric current conduction (vi). Corrosion mechanisms.	Reduce material/fabrication cost. Improve corrosion resistance. Prevent leakage. Reduce heat/electric resistance.

- i) The Nernst–Planck equation.
- ii) The water conservation equation, Eq. (3).
- iii) Butler-volmer equation, Tafel equation.
- iv) The conservation equation of O<sub>2</sub>, H<sub>2</sub>, and N<sub>2</sub>; Molecular Dynamics (MD) equations.
- v) The energy conservation equation.
- vi) Ohm's law.
- vii) Darcy's law, Navier stokes equations, VOF, PNM, LBM, and Eq. (1-2)
- viii) Phase change or Eq. (5).
- ix) Eq. (6).
- x) Eq. (7-16).



**Fig. 22.** (a) Traditional method for predicting optimal catalyst activity by the empirical Sabatier principle, and (b) workflow of catalyst screening via machine learning [247].

For catalyst optimization, Zhu et al. [248] combined the density functional theory (DFT) computation and machine learning to efficiently screen the property of dual-metal-site catalyst (DMSC) that increases the ORR activity. They conducted DFT computation to predict a series of catalysts, simplified these features, reserved the most relevant features for the database, and trained the fitting equation between the ORR activity and catalyst property. The basic workflow is shown in Fig. 23(a). Gradient-boosted regression (GBR) was used as the machine learning algorithm. Fig. 23(b) compares the values of reaction free energies of OH\* by the machine learning prediction and DFT computation, with a low RMSE of 0.036 and a high R<sup>2</sup> of 0.993, demonstrating that the GBR algorithm effectively trained the model to achieve accurate prediction. As shown in Fig. 23(c), seven features most related to catalytic performance in order of importance were given, including the electron affinity of two metal atoms (EA1 and EA2), the sum of the vdW radius of two metal atoms (R1 + R2), the difference in the Pauling electronegativity between two metal atoms (|P1 - P2|), the product of ionization energy of TM1 (IE1), the distance between two metal atoms (IE1 × L), the

sum of Pauling electronegativity of two metal atoms (P1 + P2), and the average distance between TM1/TM2 atoms and the surrounding N atoms ((d1 + d2 + d3 + d4 + d5 + d6)/6). In addition, machine learning was also applied to material selection of battery electrodes [249], but rarely to PEMFC materials of electrodes and membrane, which could be a future research direction for the PEMFC community.

#### 4.4. Machine learning for durability

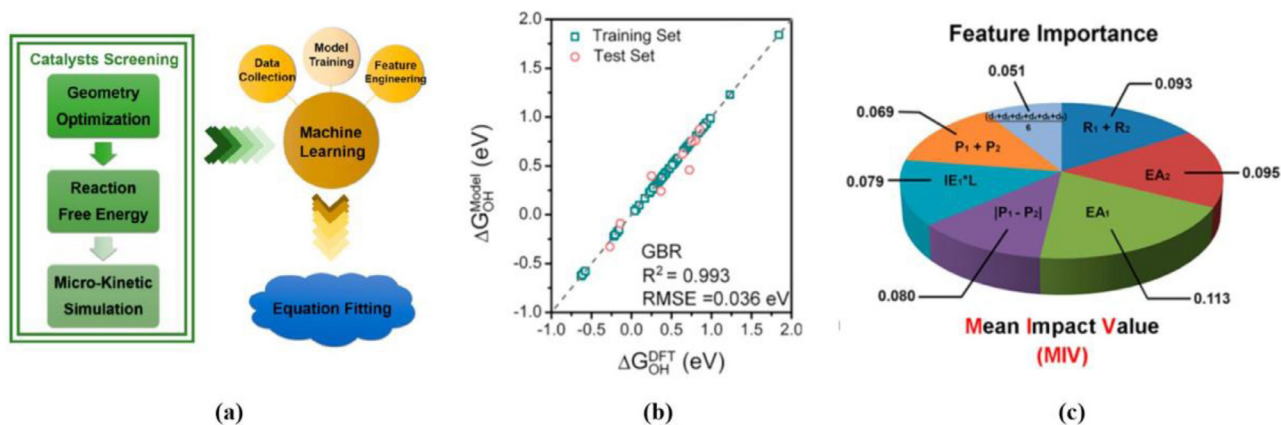
A durable and stable PEM fuel cell that is reliable for the entire life of the system is crucial for its commercialization. Thus, it is important to predict the state of health (SoH), the remaining useful life (RUL), and durability of PEM fuel cell using the data generated from monitoring units [112, 250,251]. The cell voltage is the most important indicator of fuel cell performance and thus is a popular output parameter in the machine learning. In recent years, machine learning has been employed to predict fuel cell durability and SoH, which can generally be classified as model-based and data-driven approaches. The former method relies



**Table 12**

Publicly accessible professional machine-learning tools for chemistry and material, and structure and property databases for molecules and solids. The table is developed following the format of that in Ref. [224] by adding additional information.

Name	Description	URL
<b>Machine learning tools for chemistry and material</b>		
Amp	Package to facilitate machine learning for atomistic calculations	<a href="https://bitbucket.org/andrewpeterson/amp">https://bitbucket.org/andrewpeterson/amp</a>
ANI	Neural-network potentials for organic molecules with Python interface	<a href="https://github.com/isayev/ASE_ANI">https://github.com/isayev/ASE_ANI</a>
COMBO	Python library with emphasis on scalability and efficiency	<a href="https://github.com/tsudalab/combo">https://github.com/tsudalab/combo</a>
DeepChem	Python library for deep learning of chemical systems	<a href="https://deepchem.io">https://deepchem.io</a>
GAP	Gaussian approximation potentials	<a href="http://libatoms.org/Home/Software">http://libatoms.org/Home/Software</a>
MatMiner	Python library for assisting machine learning in materials science	<a href="https://hackingmaterials.github.io/matminer">https://hackingmaterials.github.io/matminer</a>
NOMAD	Collection of tools to explore correlations in materials datasets	<a href="https://analytics-toolkit.nomad-coe.eu">https://analytics-toolkit.nomad-coe.eu</a>
PROPhet	Code to integrate machine-learning techniques with quantum-chemistry approaches	<a href="https://github.com/bikloost/PROPhet">https://github.com/bikloost/PROPhet</a>
TensorMol	Neural-network chemistry package	<a href="https://github.com/jparkhill/TensorMol">https://github.com/jparkhill/TensorMol</a>
<b>Computed structure and property databases</b>		
AFLOWLIB	Structure and property repository from high-throughput ab initio calculations of inorganic materials	<a href="http://aflowlib.org">http://aflowlib.org</a>
Computational Materials Repository	Infrastructure to enable collection, storage, retrieval and analysis of data from electronic-structure codes	<a href="https://cmr.fysik.dtu.dk">https://cmr.fysik.dtu.dk</a>
GDB	Databases of hypothetical small organic molecules	<a href="http://gdb.unibe.ch/downloads">http://gdb.unibe.ch/downloads</a>
Harvard Clean Energy Project	Computed properties of candidate organic solar absorber materials	<a href="https://cepdb.molecularspace.org">https://cepdb.molecularspace.org</a>
Materials Project	Computed properties of known and hypothetical materials carried out using a standard calculation scheme	<a href="https://materialsproject.org">https://materialsproject.org</a>
NOMAD	Input and output files from calculations using a wide variety of electronic structure codes	<a href="https://nomad-repository.eu">https://nomad-repository.eu</a>
Open Quantum Materials Database	Computed properties of mostly hypothetical structures carried out using a standard calculation scheme	<a href="http://oqmd.org">http://oqmd.org</a>
NREL Materials Database	Computed properties of materials for renewable-energy applications	<a href="https://materials.nrel.gov">https://materials.nrel.gov</a>
TEDesignLab	Experimental and computed properties to aid the design of new thermoelectric materials	<a href="http://tedesignlab.org">http://tedesignlab.org</a>
ZINC	Commercially available organic molecules in 2D and 3D formats	<a href="https://zinc15.docking.org">https://zinc15.docking.org</a>
<b>Experimental structure and property databases</b>		
ChEMBL	Bioactive molecules with drug-like properties	<a href="https://www.ebi.ac.uk/chembl">https://www.ebi.ac.uk/chembl</a>
ChemSpider	Royal Society of Chemistry's structure database, featuring calculated and experimental properties from a range of sources	<a href="https://chemspider.com">https://chemspider.com</a>
Citration	Computed and experimental properties of materials	<a href="https://citration.com">https://citration.com</a>
Crystallography Open Database	Structures of organic, inorganic, metal-organic compounds and minerals	<a href="http://crystallography.net">http://crystallography.net</a>
CSD	Repository for small-molecule organic and metal-organic crystal structures	<a href="https://www.ccdc.cam.ac.uk">https://www.ccdc.cam.ac.uk</a>
ICSD	Inorganic Crystal Structure Database	<a href="https://icsd.fiz-karlsruhe.de">https://icsd.fiz-karlsruhe.de</a>
MatNavi	Multiple databases targeting properties such as superconductivity and thermal conductance	<a href="http://mits.nims.go.jp">http://mits.nims.go.jp</a>
MatWeb	Datasheets for various engineering materials, including thermoplastics, semiconductors and fibres	<a href="http://matweb.com">http://matweb.com</a>
NIST Chemistry WebBook	High-accuracy gas-phase thermochemistry and spectroscopic data	<a href="https://webbook.nist.gov/chemistry">https://webbook.nist.gov/chemistry</a>
NIST Materials Data Repository	Repository to upload materials data associated with specific publications	<a href="https://materialsdata.nist.gov">https://materialsdata.nist.gov</a>
PubChem	Biological activities of small molecules	<a href="https://pubchem.ncbi.nlm.nih.gov">https://pubchem.ncbi.nlm.nih.gov</a>



**Fig. 23.** (a) Workflow of activity prediction and design of DMSC, and (b) comparison of the reaction free energy values of OH\* by machine learning prediction and DFT computation in the training set and test set, and (c) feature importance based on the mean impact value in Zhu et al.'s study [248].

**Table 13**  
Machine learning methods and their characteristics for PEMFC prognostics.

Method	Characteristics	References
Neural network (NN)	Data-driven. Interconnected neurons are linked using weights. The weights are optimized during training. The unknown functions are determined using a large number of data. Its prediction is accurate but computationally expensive.	[252,253,260]
Adaptive neuro-fuzzy interface system (ANIFS)	Data-driven. Similar to the NN method. The membership functions and rules are used to connect different layers. Computation is efficient. Prediction is reliable.	[252,262]
Grid long short-term memory (G-LSTM)	Data-driven. Compared to NN, LSTM avoids exploding gradients and vanishing problems and is suitable for long-term prediction. Prediction accuracy can be optimized.	[253]
recurrent neural network (RNN)		
Summation-wavelet extreme learning machine (SW-ELM)	Data-driven. SW-ELM is the combination of NN and wavelet theory. It doesn't require big data and is suitable for prediction at frequent intervals.	[254,266]
Istm rnn with auto-regressive integrated moving average (arima)	data-driven. combination with arima enables effective tracking of degradation tendency and reduces influence of the recovery phenomenon. its algorithm is simple and easy for online application.	[255]
gray neural network model (gnnm)	data-driven. coupling with the gray theory enables use of limited historical data and is suitable for degradation involving nonlinear changes and many influencing factors.	[257]
Particle filtering (PF)	Model-based. Monte-Carlo technique is used to solve nonlinear Bayesian tracking for the probability distribution. It is time-consuming but addresses complex conditions.	[252,265]
Sparse auto encoder (SAE) NN	Model-based and data-driven combination. SAE can extract prediction features automatically and NN is used to predict the RUL. It can predict dynamic conditions.	[260]
Moving window method	Model-based and data-driven combination. Both the fade trend and non-linear features are captured. It can iteratively update the prediction when newly measured data become available	[256]
Self-organizing maps (SOMs)	Unsupervised learning. Monitoring data are automatically visualized into a 2D space, thus it is easy and intuitive. It can be used to monitor the fuel cell SoH.	[258]
Echo State Network (ESN)	Supervised learning based on the principle of recurrent neural networks (RNNs). A nonlinear response signal is induced by driving random, large and fixed RNNs. A trainable combination of all these response signals is then used to obtain a desired output signal. Such a method can reduce the error associated with the prediction of remaining life.	[261,264]

on physical or semi-empirical models, which can be computationally expensive. The data-driven method uses historical data of a system to predict the SoH and RUL. In the literature, both types of methods have been investigated for the SoH and RUL prediction, including some studies that compare various algorithms. A summary of various ML methods employed for PEMFC prognostic and their characteristics is given in Table 13.

Mao and Jackson [252] compared the ANN, the adaptive neuro-fuzzy inference system (ANFIS), and the particle filtering (PF) method in the PEMFC voltage and SoH prediction. It was shown that the ANFIS provides an accurate forecast at a low computation cost, and the PF is suitable for complex situations, such as fuel cell faults. Ma et al. [253] developed a novel data-driven deep learning model for degradation prognostics using the grid long short-term memory (G-LSTM) recurrent neural network (RNN). Compared to traditional neural networks, the proposed model effectively avoided exploding gradients and optimized prediction accuracy. It is also easy to implement online due to its simple structure and can be used for improving durability when coupled with a proper control strategy. Javed et al. [254] presented a constraint-based summation-wavelet extreme learning machine (SW-ELM) algorithm to improve the robustness and applicability of data-driven prognostics. A new SoH indicator was introduced to characterize the dynamic behaviors of a stack voltage and to further improve prediction accuracy. The model also showed promise in estimating the RUL. Ma et al. [255] proposed a LSTM RNN and an auto-regressive integrated moving average (ARIMA) fusion method to predict fuel cell SoH. LSTM enabled efficient prediction of long-term degradation, while the fusion with ARIMA tracks degradation tendency. The model was validated against aging experimental datasets from two PEM fuel cells and showed promise in facilitating management strategy design and performance prediction before experimental tests. Zhou et al. [256] combined the model-based and data-driven prognostic methods and used the moving window method to train the models, update the weight factors, and further fuse the pre-

diction iteratively. The model-based approach predicted the aging trend over a long period while the data-driven approach was used to describe the local non-linear characteristics of voltage degradation. Thus, the proposed hybrid prognostic approach simultaneously described the long-term degradation and short-term voltage variation characteristics. Chen et al. [257] proposed a gray neural network model (GNNM) method in combination with the particle swarm optimization (PSO) and the moving window method. The effects of current density, inlet temperature, inlet hydrogen pressure, and inlet RH were taken into account in the model to better forecast degradation under various operating conditions. They also investigated the influence of different moving window sizes on degradation prediction. Onanena et al. [258] proposed an unsupervised model to monitor fuel cell SoH via the electrochemical impedance spectroscopy (EIS) data. Compared to supervised methods, the model does not require a large amount of labeled data, and is efficient and easy to implement. The model is based on self-organizing maps (SOMs), which can be used to visually identify the main clusters in datasets and correct eventual data mislabeling. Mayur et al. [259] coupled an FCEV model with a cell-level catalyst degradation model to estimate durability and provide insights into spatially resolved cell performance. The effect of transient loading was investigated in terms of the cathode potential, water/oxygen concentration, and spatial variation in the Pt dissolution rate in the cathode CL. It was found that the Pt dissolution rate is high under low power demand and exhibits highly dynamic behavior during a driving cycle. Liu et al. [260] developed a RUL prediction technique for PEM fuel cells based on the sparse autoencoder (SAE) and deep neural network (DNN). The SAE was used to extract the prediction features automatically, while the DNN was applied to predict the RUL. The Gaussian-weighted moving average filter was adopted to smooth noisy data. The model prediction was compared with a total of 127,369 experimental data points, indicating an accuracy as high as 99.68%. In addition, the model is capable of predicting the RUL under dynamic conditions. Morando et al. [261] proposed a data-driven algorithm to

**Table 14**  
Summary of recent machine learning studies on performance, dynamics, durability, SoH, and RUL of PEM fuel cells.

Machine Learning	Targets for PEM fuel cells	Remarks	Reference
ANN	Fuel cell performance (output voltage) prediction	i Data points: 460 ii Data sources: experiment iii Two-hidden-layer ANN.	[233]
ANN and SVM	Fuel cell performance (output voltage) prediction	i Data points:1377 ii Data sources: experiment iii One-hidden-layer ANN iv ANN ( $R^2$ of 0.999) outperforms SVM ( $R^2$ of 0.980)	[234]
Linear regression; ANN	Output voltage and efficiency prediction	i Data points: 723 ii Data sources: experiment iii Two-hidden-layer ANN	[235]
ANN; SVM	Output voltage and efficiency prediction	i Data points: 9527 ii Data sources: experiment iii One-hidden-layer ANN iv SVM ( $R^2$ of 0.99) outperforms ANN ( $R^2$ of 0.97)	[236]
Hebbian learning	Output voltage and efficiency prediction	i Data points: 1000 ii Data sources: experiment	[238]
ANN	Dynamic voltage prediction	i Data sources: experiments ii Two-hidden-layer ANN	[239]
ANN	Dynamic voltage prediction	i Data sources: Matlab simulation using physics-based model ii Two-hidden-layer ANN	[240]
SVM	Output voltage prediction at various CL compositions.	i Data points: 65 ii Data sources: 3D physics-based simulation	[242]
ANN	Activation overpotential at various CL compositions.	i Data sources: 1D homogenous agglomerate simulation ii One-hidden-layer ANN	[243]
ANN; SVM	Multi-physics fields of PEM fuel cells.	i 100 case scenarios, and 7000 data points ii Data sources: 3D physics-based simulation iii Two-hidden-layer ANN	[244]
Gradient-boosted regression	ORR activity prediction of catalysts.	i Data sources: simulation (DFT)	[248]
ANN; Adaptive neuro-fuzzy inference system (ANFIS)	Fuel cell performance (output voltage) prediction with time for prognostics.	i Data sources: experiments ii One-hidden-layer ANN iii ANFIS has highest efficiency in computation time	[252]
Grid long short-term memory recurrent neural network (G-LSTM-RNN)	Fuel cell performance (output voltage) prediction and degradation.	i Data sources: experiments (from three fuel cells) from 400 h testing each. ii One-hidden-layer RNN iii Sliding window size update	[253]
Summation-wavelet extreme learning machine (SW-ELM)	Fuel cell output voltage with time for degradation and RUL prognostics.	i Data sources: stack experiments ii 70 A and 1155 h. iii Hourly voltage as a health indicator. iv RUL is carried out in two groups, a prognostic task at initial 650 h and updates every 10 h as new data.	[254]

(continued on next page)



Table 14 (continued)

Machine Learning	Targets for PEM fuel cells	Remarks	Reference
Long short-term memory recurrent neural network (LSTM-RNN)	Fuel cell output voltage with time for degradation	<ul style="list-style-type: none"> <li>i Data sources: experiments</li> <li>ii 1000 h aging data at <math>0.7 \text{ Acm}^{-2}</math>.</li> <li>iii The voltage as an indicator of health.</li> </ul>	[255]
a hybrid method which combines a degradation empirical model and non-linear autoregressive neural network (narnn)	fuel cell output voltage with time for degradation	<ul style="list-style-type: none"> <li>i data sources: experiments</li> <li>ii the empirical model for long-term aging prediction and the narnn for nonlinear characteristics prediction of degradation.</li> <li>iii a moving window method for the hybrid prognostic approach.</li> <li>iv 400 h aging data for training and testing.</li> </ul>	[256]
gray neural network (gnn)	fuel cell output voltage with time for degradation	<ul style="list-style-type: none"> <li>i data sources: experiments</li> <li>ii a moving window method for iterative training.</li> <li>iii 800 h aging data for studying different moving window sizes &amp; prediction capability.</li> <li>iv 550 h data at 70 a for predicting degradation.</li> </ul>	[257]
Self-organizing maps (SOMs)	Fuel cell SoH monitor using the EIS data	<ul style="list-style-type: none"> <li>i An unsupervised method to visually identify the main clusters in datasets and correct eventual data mislabeling</li> <li>ii 11 data points are used</li> </ul>	[258]
Sparse autoencoder (SAE) and deep neural network (DNN)	Remaining life prediction (RUL)	<ul style="list-style-type: none"> <li>i i.-100k data for validation</li> <li>ii Experimental stack data (V &amp; I) per hour.</li> <li>iii SAE extracts the prediction features automatically, and DNN realizes the RUL prediction.</li> </ul>	[260]
Echo State Network (ESN)	Fuel cell output voltage with time for degradation	<ul style="list-style-type: none"> <li>i Data sources: experiments</li> <li>ii 1000 h aging data</li> <li>iii Data is smoothed prior to use</li> <li>iv 900 h data for training.</li> </ul>	[261]
Adaptive neuro-fuzzy inference system	Fuel cell output voltage with time for degradation	<ul style="list-style-type: none"> <li>i Data sources: experiments</li> <li>ii Hurst coefficient and the wavelet transform were used to filter the signals.</li> <li>iii The algorithm is divided into two parts, filtering and prognosis</li> <li>iv 1700 h data are used for prediction and testing.</li> </ul>	[262]
Echo State Network (ESN)	RUL prognostics.	<ul style="list-style-type: none"> <li>i Data sources: experiments</li> <li>ii 1000 h aging data.</li> <li>iii Direct and parallel forecasts are used.</li> </ul>	[264]
Summation-wavelet extreme learning machine (SW-ELM)	RUL prognostics.	<ul style="list-style-type: none"> <li>i Data sources: stack experiments</li> <li>ii Two sets of data including dynamic and stationary operations with 1000 h data each.</li> <li>iii 168 h data for learning; the rest for testing.</li> <li>iv 4 predictive models were tested.</li> </ul>	[266]

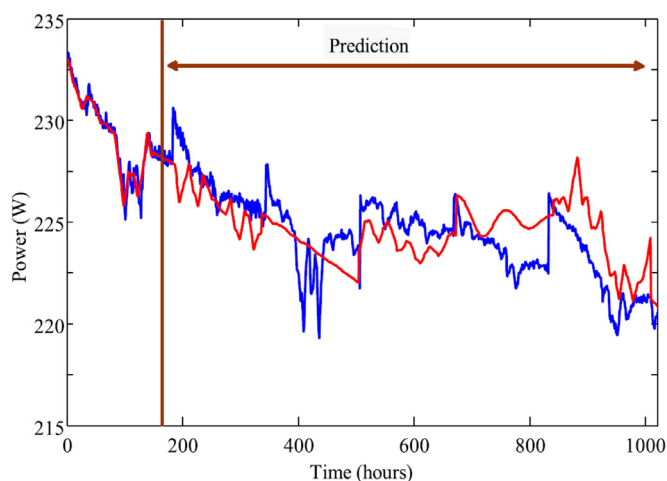


Fig. 24. Prediction of the PEMFC power signal. The red and blue lines represent the prediction and the actual signal, respectively [266].

predict evolution of PEMFC performance and occurrence of a fault. The echo state network was applied in the model to reduce prediction error. Silva et al. [262] developed an algorithm based on ANFIS to forecast the voltage decay due to degradation. The algorithm architecture and parameter selection were investigated for prediction accuracy and applicability. Input signal data were divided into normal operation and external perturbations. The latter were unpredictable, and therefore were not used to train the ANFIS. It was shown that the ANFIS is well adapted to time-series prediction, particularly to degradation. Javed et al. [263] reported that prediction accuracy is determined by the features extracted from raw data, and the usefulness of the data is highly dependent on the variability of phenomena. A new processing method was proposed by applying trigonometric functions and cumulative transformation to better extract and select data. Morando et al. [264] applied a reservoir computing tool, the echo state network (ESN), as a prognostics system to quickly and accurately estimate the RUL. The ESN has the same modeling capability as a RNN with high computation efficiency. The accuracy and complexity of the network were found to be dependent on the ESN parameters and design. Jouin et al. [265] built a prognostics framework that can accurately estimate the RUL without assumptions on PEMFC behaviors. The framework is based on the particle filtering approach with an accuracy of  $\pm 90$  h in a 1000-h lifetime. They also showed that a model with both a logarithmic and a linear component is more efficient than a simple linear model. Ibrahim et al. [266] proposed a discrete wavelet transform (DWT)-based univariate prognostic model to provide an online prediction without exogenous data. The main advantage is that the prediction only used past information from a univariate time series and is therefore easy to implement in practice. Fig. 24 shows an example of the model prediction of fuel cell power evolution in comparison with actual data. Table 14 briefly summarizes the machine learning studies in PEM fuel cells in this review.

## 5. Summary and concluding remarks

In this review, we summarize the latest status of PEM fuel cells in portable, small stationary, and transportation power applications, discuss important fundamentals related to fuel cell materials, design, control, and durability, and explain machine learning, physics-informed deep learning, and artificial intelligence (AI) in energy applications and their great potentials in advancing PEMFC technology.

As of December 2019, more than 19,000 commercial FCEVs have been deployed in the U.S., Japan, South Korea, Europe, and China, and over 340 HFRs were available to serve these FCEVs. The Hyundai Nexo

and Toyota Mirai are two models of FCEVs and account for about 63% and 32% of total sales, respectively, in 2019. By 2030, Japan, South Korea, and China plan to deploy  $\sim 0.85$ , 0.8, and 1 million FCEVs, and build  $\sim 1200$ , 900, and 1000 HFRs, respectively. In the U.S., more than 30 FVEBs are operated, serving approximately 17 million passengers by 2017. Most of them have achieved or nearly met the ultimate target of 25,000 h. In Europe, about 100 FCEB demonstrations have been completed across the continent, with the achievement of 35,000 h by a Ballard fuel cell stack. In the portable sector, PEM fuel cell units have been developed as electric charger and power sources for drones, wearables, and military purposes. The backup power and small stationary power generation of PEM fuel cells have been rapidly growing in recent years. Co-gen fuel cell units can reach over 80% efficiency for power and thermal energy utilization.

Despite great progress in commercialization, cost and durability are still the two main barriers to worldwide deployment. It is challenging to achieve the durability target under the PGM loading target by set by the DOE. Although FCEVs and FCEBs have met the 3000 h real-world driving test and ultimate target of 25,000 h, respectively, they are still more expensive than conventional fossil-fuel based vehicles. The Toyota Mirai costs 100–200% more than a common gasoline vehicle, even after large governmental incentives. The current cost for an FCEV is approximately \$45/kW, almost 50% higher than the ultimate DOE target (\$30/kW). A FCEB currently costs approximately 1 million dollars, even at a production volume of 40.

Fundamentals are crucial in overcoming major barriers and further advancing PEM fuel cell technology for high performance. New PEM materials, low PGM-loading, and non-PGM catalysts are important for reducing fuel cell cost. Two-phase flow in porous components such as CLs, GDLs, and GFCs must be effectively managed to ensure high performance and durability. Fuel cell dynamics must be understood in practice for control strategy and health monitoring. Cold-start capability is important for transportation and portable applications in freezing environments, requiring physics of ice production and thermal behaviors involving phase change, and their interaction with the electrochemical reaction.

Machine learning and artificial intelligence (AI) are powerful tools for energy and material R&D, and have been growing rapidly in recent years. Machine learning and AI have great potential to advance PEMFC technology to reduce cost and improve durability/performance, and are advantageous in computation efficiency and taking into account the effects of physics that are yet unknown or formulated, but contained in training databases. They have been applied to predict PEMFC performance, optimize cell design, and selection/optimization of catalyst, and showed a great promise in developing fundamental correlations for two-phase flow and material properties, analyzing ex-/in-situ images of PEMFC operation, and facilitating advanced model development using imaging data or physics-informed deep learning that encodes flow equations, capillary pressure correlations, and dimensionless parameters into the neural networks. They can also be applied to predict fuel cell dynamics, SoH/RUL monitoring, and durability enhancement through analysis of real-time data and incorporation of dynamic characteristics and key parameters in neural network learning, and assist in developing control strategies to meet loading requirements, enable cold start, optimize operation based on real-time monitoring, and mitigate material degradation. Main physics and fundamentals in PEM fuel cells were summarized for physics-informed deep learning, along with the major public resources of machine learning databases and tools for materials and chemistry.

## Declaration of Competing Interest

None

## Acknowledgements

NZ would like to acknowledge the financial support of the State of Baden-Wuerttemberg via the BWPlus Program under the HyFab-BW project, L7520113. YW gratefully acknowledges the support of the National Science Foundation, USA (CBET-1336873) and industry sponsors on this study. YW also thanks Dongyang Li and Pengjie Tian in the lab for their assistance in the paper preparation. NZ would also like to thank Yuze Hou for his assistance in the preparation of the section related to machine learning and durability.

## References

- [1] Satyapal S. Overview of DOE Hydrogen and Fuel Cells Program. US Department of Energy Annual Merit Review 2019.
- [2] Debe MK. Electrocatalyst approaches and challenges for automotive fuel cells. *Nature* 2012;486:43–51.
- [3] EG&G Technical Services Inc. Fuel Cell Handbook 7th ed. U.S. Department of Energy 2004.
- [4] Basu S. Recent trends in fuel cell science and technology. Springer & Anamaya Publishers; 2007.
- [5] Abderezzak B. Introduction to transfer phenomena in pem fuel cells. 1st ed. Elsevier; 2018.
- [6] AFC Energy. [www.afcenergy.com](http://www.afcenergy.com); 2020.
- [7] Doosan Fuel Cell. [www.doosanfuelcellamerica.com](http://www.doosanfuelcellamerica.com); 2020.
- [8] FuelCell Energy. [www.fuelcellenergy.com](http://www.fuelcellenergy.com); 2020.
- [9] Bloom Energy. <https://www.bloomenergy.com>; 2020.
- [10] Hart D, Lehner F, Jones S, et al. The fuel cell industry review. E4tech 2019.
- [11] Wang Y, Diaz DFR, Chen KS, et al. Materials, technological status, and fundamentals of PEM fuel cells: a review. *Materials Today* 2020;32:178–203.
- [12] US Department of Energy. DOE Technical targets for fuel cell backup power systems. <https://www.energy.gov/eere/fuelcells/doe-technical-targets-fuel-cell-backup-power-systems>; 2020.
- [13] Ballard Power System. [www.ballard.com](http://www.ballard.com); 2020.
- [14] The National Renewable Energy Laboratory (NREL). Current fuel cell system low volume price by application. [www.nrel.gov/hydrogen/assets/images/cdp\\_lab\\_15.jpg](http://www.nrel.gov/hydrogen/assets/images/cdp_lab_15.jpg); 2018.
- [15] US Department of Energy. DOE Technical targets for fuel cell systems for stationary (combined heat and power) applications. [www.energy.gov/eere/fuelcells/doe-technical-targets-fuel-cell-systems-stationary-combined-heat-and-power](http://www.energy.gov/eere/fuelcells/doe-technical-targets-fuel-cell-systems-stationary-combined-heat-and-power); 2020.
- [16] Panasonic Corporation. [panasonic.biz/appliance/FC/lineup/house03.html](http://panasonic.biz/appliance/FC/lineup/house03.html).
- [17] Arias J. Hydrogen and fuel cells in japan. EU-Japan Centre for Industrial Cooperation 2019. [https://www.eu-japan.eu/sites/default/files/publications/docs/hydrogen\\_and\\_fuel\\_cells\\_in\\_japan.pdf](https://www.eu-japan.eu/sites/default/files/publications/docs/hydrogen_and_fuel_cells_in_japan.pdf).
- [18] SFC Energy. [www.sfc.com/en](http://www.sfc.com/en); 2020.
- [19] US Department of Energy. DOE Technical targets for fuel cell systems for portable power and auxiliary power applications. [www.energy.gov/eere/fuelcells/doe-technical-targets-fuel-cell-systems-portable-power-and-auxiliary-power](http://www.energy.gov/eere/fuelcells/doe-technical-targets-fuel-cell-systems-portable-power-and-auxiliary-power); 2020.
- [20] US Department of Energy. Spotlight: artificial intelligence. [https://www.energy.gov/sites/prod/files/2019/10/f67/2019-09-30\\_Spotlight-Artificial\\_Intelligence\\_0.pdf](https://www.energy.gov/sites/prod/files/2019/10/f67/2019-09-30_Spotlight-Artificial_Intelligence_0.pdf); 2019.
- [21] Wang Y, Chen KS, Mishler J, et al. A review of polymer electrolyte membrane fuel cells: technology, applications, and needs on fundamental research. *Appl Energy* 2011;88:981–1007.
- [22] Carter D, Ryan M, Wing J. The fuel cell industry review 2012. *Fuel Cell Today* 2012.
- [23] Carter D, Wing J. The fuel cell industry review 2013. *Fuel Cell Today* 2013.
- [24] Hart D, Lehner F, Rose R, et al. The fuel cell industry review 2017. E4tech 2017.
- [25] MyFC. [www.myfcpower.com](http://www.myfcpower.com); 2019.
- [26] Intelligent Energy. [www.intelligent-energy.com](http://www.intelligent-energy.com); 2018.
- [27] SerEnergy. [www.serenenergy.com](http://www.serenenergy.com); 2020.
- [28] Siqens. [www.siqens.de](http://www.siqens.de); 2020.
- [29] BOC. [www.boconline.co.uk](http://www.boconline.co.uk); 2020.
- [30] Biebuyck B. FCH-JU initiatives towards realization of a hydrogen society. Conference at the Tokyo FC Expo; 2020.
- [31] Private sector Road map to a US hydrogen economy. The Fuel Cell and Hydrogen Energy Association 2019. [www.fchea.org/us-hydrogen-study](http://www.fchea.org/us-hydrogen-study).
- [32] Kan S. South Korea's hydrogen strategy and industrial perspectives. [www.ifri.org/sites/default/files/atoms/files/sichao\\_kan\\_hydrogen\\_korea\\_2020\\_1.pdf](http://www.ifri.org/sites/default/files/atoms/files/sichao_kan_hydrogen_korea_2020_1.pdf); 2020.
- [33] Yoon Y. Current status of the Korean hydrogen economy. Austrian Chamber of Commerce Event: Future of Hydrogen Technologies in Korea and Japan; 2020.
- [34] Ministry of Trade. Industry and energy of South Korea, hydrogen economy roadmap of Korea. [www.motie.go.kr/motie/ne/presse/press2/bbs/bbsView.do?bbs\\_cd\\_n=81&cate\\_n=1&bbs\\_seq\\_n=161262](http://www.motie.go.kr/motie/ne/presse/press2/bbs/bbsView.do?bbs_cd_n=81&cate_n=1&bbs_seq_n=161262); 2019.
- [35] Ministry of Trade. Trade and industry of japan, the strategic road map for hydrogen and fuel cells. [www.meti.go.jp/english/press/2019/0312\\_002.html](http://www.meti.go.jp/english/press/2019/0312_002.html); 2019.
- [36] Private sector represented by Hydrogen Europe Hydrogen roadmap Europe: a sustainable pathway for the European energy transition. Fuel Cells and Hydrogen Joint Undertaking 2019. [www.fch.europa.eu/news/hydrogen-roadmap-europe-sustainable-pathway-european-energy-transition%20](http://www.fch.europa.eu/news/hydrogen-roadmap-europe-sustainable-pathway-european-energy-transition%20).
- [37] Brasington L. Hydrogen in China. [www.cleantech.com/hydrogen-in-china](http://www.cleantech.com/hydrogen-in-china); 2019.
- [38] Carr J. Chinese fuel cell industry developments. The Fuel cell and Hydrogen Energy Association 2019. [www.fchea.org/in-transition/2019/2/4/chinese-fuel-cell-industry-developments](http://www.fchea.org/in-transition/2019/2/4/chinese-fuel-cell-industry-developments).
- [39] Kane M. Hydrogen fuel cell car sales in 2019 improved to 7,500 globally. [www.insideevs.com/news/397240/hydrogen-fuel-cell-sales-2019-7500-globally](http://www.insideevs.com/news/397240/hydrogen-fuel-cell-sales-2019-7500-globally); 2020.
- [40] Information Trends. Hydrogen fuel cell vehicles: a global analysis; 2018.
- [41] Deloitte and Ballard. Fueling the future of mobility; 2020.
- [42] Alternative Fuels Data Center. Hydrogen laws and incentives in California. [www.afdc.energy.gov/fuels/laws/HY?state=ca](http://www.afdc.energy.gov/fuels/laws/HY?state=ca); 2020.
- [43] California Fuel Cell Partnership. [www.cafcp.org](http://www.cafcp.org); 2020.
- [44] Uribe FA, Gottesfeld S, Zawodzinski TA. Effect of ammonia as potential fuel impurity on proton exchange membrane fuel cell performance. *J Electrochem Soc* 2002;149:A293–6.
- [45] The International Energy Agency. The future of hydrogen. Report for the G20 meetings in Japan; 2019.
- [46] Gielen D, Taibi E, Miranda R. Hydrogen: a renewable energy perspective. International Renewable Energy Agency; 2019.
- [47] United States Environmental Protection Agency. Explaining electric & plug-in hybrid electric vehicles. [www.epa.gov/greenvehicles/explaining-electric-plug-hybrid-electric-vehicles](http://www.epa.gov/greenvehicles/explaining-electric-plug-hybrid-electric-vehicles); 2020.
- [48] Hyundai News. 2019 Hyundai NEXO: the next-generation fuel cell SUV. [www.hyundai.com/models/hyundai-nexo-2019-nexo](http://www.hyundai.com/models/hyundai-nexo-2019-nexo); 2018.
- [49] Hyundai News. Hyundai motor group reveals 'FCEV Vision 2030' [www.hyundai.com/brand/hyundai-motor-group-reveals-fcev-vision-2030](http://www.hyundai.com/brand/hyundai-motor-group-reveals-fcev-vision-2030); 2018.
- [50] Fuel Cell Works. Milestone: toyota's 10,000th fuel cell Mirai comes off the assembly line. [www.fuelcellworks.com/news/milestone-toyotas-10000th-fuel-cell-mirai-comes-off-the-assembly-line](http://www.fuelcellworks.com/news/milestone-toyotas-10000th-fuel-cell-mirai-comes-off-the-assembly-line); 2019.
- [51] Yoshida T, Kojima K. Toyota MIRAI fuel cell vehicle and progress toward a future hydrogen society. *Electrochem Soc Interface* 2015;24(2):45–9.
- [52] Toyota News. Second generation Mirai. [www.toyota-europe.com/world-of-toyota/articles-news-events/2019/new-mirai-concept](http://www.toyota-europe.com/world-of-toyota/articles-news-events/2019/new-mirai-concept); 2019.
- [53] Toyota News. Toyota moves to expand mass-production of fuel cell stacks and hydrogen tanks towards ten-fold increase post-2020. [www.global.toyota/en/newsroom/corporate/22647198.html](http://www.global.toyota/en/newsroom/corporate/22647198.html); 2018.
- [54] Honda News. Honda commences Japanese sales of Honda clarity fuel cell. [www.hondanews.eu/lt/cars/media/pressreleases/72430/honda-commences-japanese-sales-of-honda-clarity-fuel-cell](http://www.hondanews.eu/lt/cars/media/pressreleases/72430/honda-commences-japanese-sales-of-honda-clarity-fuel-cell); 2016.
- [55] General Motors News. GM, Honda to collaborate on next-generation fuel cell technologies. [media.gm.com/media/us/en/gm/news.detail.html/content/Pages/news/us/en/2013/Jul/0702-gm-honda.html](http://media.gm.com/media/us/en/gm/news.detail.html/content/Pages/news/us/en/2013/Jul/0702-gm-honda.html); 2013.
- [56] General Motors News. GM and Honda to establish industry-first joint fuel cell system manufacturing operation in Michigan. [media.gm.com/media/us/en/gm/news.detail.html/content/Pages/news/us/en/2017/jan/0130-tunein.html](http://media.gm.com/media/us/en/gm/news.detail.html/content/Pages/news/us/en/2017/jan/0130-tunein.html); 2017.
- [57] Pollet BG, Kocha SS, Staffell I. Current status of automotive fuel cells for sustainable transport. *Curr Opin Electrochem* 2019;16:90–5.
- [58] Yasuda T, Nakamura S, Honda Y, et al. Effects of polymer structure on properties of sulfonated polyimide/protic ionic liquid composite membranes for nonhumidified fuel cell applications. *ACS Appl Mater Interfaces* 2012;4:1783–90.
- [59] Kia Motors Corp. Fuel cell electric vehicle, changing the history. [http://m.kia.com/worldwide/about\\_kia/eco\\_dynamics/hydrogen\\_fuel\\_cell\\_cars.do](http://m.kia.com/worldwide/about_kia/eco_dynamics/hydrogen_fuel_cell_cars.do); 2015.
- [60] Doran M. Engineering the extreme capability of the colorado ZH2. [media.chevrolet.com/media/us/en/chevrolet/news.detail.html/content/Pages/news/us/en/2016/oct/1101-zh2.html](http://media.chevrolet.com/media/us/en/chevrolet/news.detail.html/content/Pages/news/us/en/2016/oct/1101-zh2.html); 2016.
- [61] Swan T. 2017 Chevrolet colorado ZH2: gm's military role fuel cell bows. [www.kbb.com/car-news/all-the-latest/2017-chevrolet-colorado-zh2-gm-military-role-fuel-cell-bows/2100001203](http://www.kbb.com/car-news/all-the-latest/2017-chevrolet-colorado-zh2-gm-military-role-fuel-cell-bows/2100001203); 2016.
- [62] Herdlitschka M. Mercedes-Benz F-Cell: market launch of the world's first electric vehicle featuring fuel cell and plug-in hybrid technology. [media.daimler.com/marsMediaSite/en/instance/ko/Mercedes-Benz-GLC-F-CELL-Market-launch-of-the-worlds-first-electricvehicle-featuring-fuel-cell-and-plug-in-hybrid-technology.xhtml?oid=41813012](http://media.daimler.com/marsMediaSite/en/instance/ko/Mercedes-Benz-GLC-F-CELL-Market-launch-of-the-worlds-first-electricvehicle-featuring-fuel-cell-and-plug-in-hybrid-technology.xhtml?oid=41813012); 2018.
- [63] Hyundai News. All-new Hyundai NEXO: technical specifications. [www.hyundai.com/press-kits/all-new-hyundai-nexo-technical-specifications](http://www.hyundai.com/press-kits/all-new-hyundai-nexo-technical-specifications); 2018.
- [64] Satyapal S. Hydrogen and fuel cells program overview. US Department of Energy Annual Merit Review; 2018.
- [65] Eudy L. Technology validation: fuel cell bus evaluations (No. NREL/PR-5400-66177). National Renewable Energy Laboratory 2018.
- [66] Fuel Cell Electric Buses. [www.fuelcellbuses.eu](http://www.fuelcellbuses.eu); 2020.
- [67] MacEwen R. Future of E-mobility. Liberm Conference 2019.
- [68] Van Hool News. [www.vanhool.be/en/news/van-hool-to-present-three-world-premieres-and-18-vehicles-at-busworld-europe-2019](http://www.vanhool.be/en/news/van-hool-to-present-three-world-premieres-and-18-vehicles-at-busworld-europe-2019); 2019.
- [69] Busworld Europe. [www.busworldeurope.org/exhibition/awards/busworld-awards-for-bus-coach/winners-2019](http://www.busworldeurope.org/exhibition/awards/busworld-awards-for-bus-coach/winners-2019); 2019.
- [70] H2Bus Europe. [www.h2bus.eu](http://www.h2bus.eu); 2020.
- [71] Van Hool to Build 40 Buses for Cologne and Wuppertal, with Order for Ballard Fuel Cells. *Fuel Cells Bull* 2018;2018:2–3.
- [72] Van Hool orders 20 Ballard modules for Dutch fuel cell buses. *Fuel Cells Bull* 2020;2020:3–4.
- [73] Sustainable Bus Van Hool towards the Launch of the New A330 FC and Exqui.City 18 FC. A fuel cell future. 2019. <https://www.sustainable-bus.com/news/van-hool-launch-new-a330-fc-and-exqui-fuel-cell-future>.



- [74] FuelCellsWorks. The First Fuel Cell Buses in Operation in Denmark!. <https://fuelcellworks.com/news/the-first-fuel-cell-buses-in-operation-in-denmark/>; 2020.
- [75] Businova. Hydrogen. <http://www.businova.com/en/range/hydrogen.html>; 2020.
- [76] Businova. Launch of the First Businova Hydrogen. <http://www.businova.com/en/home/breaking-news/artois-2019.html>; 2019.
- [77] Fleet Transport. StreetDeck Fuel Cell Electric Vehicle (FCEV) Premiered at Euro Bus Expo. <https://fleet.ie/streetdeck-fuel-cell-electric-vehicle-fcev-premiered-at-euro-bus-expo>; 2018.
- [78] T.E. Transport Engineer. Hydrogen Fuel Cell Drivetrains. <http://www.transportengineer.org.uk/transport-engineer-features/hydrogen-fuel-cell-drivetrains/219902>; 2019.
- [79] Ballard News. Ballard Announces Order From Wrightbus For 20 Fuel Cell Modules to Power London Buses. <https://www.ballard.com/about-ballard/newsroom/news-releases/2019/05/13/ballard-announces-order-from-wrightbus-for-20-fuel-cell-modules-to-power-london-buses>; 2019.
- [80] Ballard News. Ballard Announces Order From Wrightbus For 15 Fuel Cell Modules to Power Aberdeen Buses. <https://www.ballard.com/about-ballard/newsroom/news-releases/2019/07/24/ballard-announces-order-from-wrightbus-for-15-fuel-cell-modules-to-power-aberdeen-buses>; 2019.
- [81] CaetanoBus. H2.City Gold. <https://caetanobus.pt/en/buses/h2-city-gold>; 2020.
- [82] CaetanoBus. Here is H2.City Gold, the new Caetano hydrogen-powered bus. <https://caetanobus.pt/en/esta-ai-o-h2-city-gold-o-novo-autocarro-caetano-a-hidrogenio>; 2019.
- [83] Solaris. DIRECTION Hydrogen: even more clean kilometers. <https://www.solarisbus.com/en/vehicles/zero-emissions/urbino-electric>; 2020.
- [84] Ballard News. Ballard Announces Order From Solaris For 25 Fuel Cell Modules to Power Buses in Germany. <https://www.ballard.com/about-ballard/newsroom/news-releases/2020/03/12/ballard-announces-order-from-solaris-for-25-fuel-cell-modules-to-power-buses-in-germany>; 2020.
- [85] Sustainable Bus. A Fleet of 25 Solaris Hydrogen Buses Headed to Germany. <https://www.sustainable-bus.com/fuel-cell/a-fleet-of-25-solaris-hydrogen-buses-headed-to-germany>; 2020.
- [86] MarketWatch. Stationary fuel cells market 2020: SWOT analysis, top countries data, definition, market size, growth factors, segmentation and forecast to 2024. <https://www.marketwatch.com/press-release/stationary-fuel-cells-market-2020-swt-analysis-top-countries-data-definition-market-size-growth-factors-segmentation-and-forecast-to-2024-2020-04-13>; 2020.
- [87] FuelCellStore. Stationary fuel cell power applications. <https://www.fuelcellstore.com/blog-section/stationary-fuel-cell-power-applications>; 2019.
- [88] US Department of Energy. Fuel cells for stationary power applications. [https://www.energy.gov/sites/prod/files/2018/01/f46/ftco\\_fc\\_stationary\\_power\\_apps.pdf](https://www.energy.gov/sites/prod/files/2018/01/f46/ftco_fc_stationary_power_apps.pdf); 2017.
- [89] Fuel Cell Technologies Office. State of the states: fuel cells in America 2016. [https://www.energy.gov/sites/prod/files/2016/11/f34/ftco\\_state\\_of\\_states\\_2016.pdf](https://www.energy.gov/sites/prod/files/2016/11/f34/ftco_state_of_states_2016.pdf); 2016.
- [90] Chaben J. Japan fuel cell developments. FCHEA, <http://www.fchea.org/in-transition/2019/3/11/japan-fuel-cell-developments>; 2019.
- [91] Zamel N, Li X. Effect of contaminants on polymer electrolyte membrane fuel cells. *Prog Eng Combust* 2011;37:292–329.
- [92] Shabani B, Haftanani M, Khamani S, et al. Poisoning of proton exchange membrane fuel cells by contaminants and impurities: review of mechanisms, effects, and mitigation strategies. *J Power Sources* 2019;427:21–48.
- [93] Jiao K, Li XG. Water transport in polymer electrolyte membrane fuel cells. *Prog Eng Combust* 2011;37:221–91.
- [94] Wang Y, Chen KS. *pem fuel cells: thermal and water management fundamentals*. Momentum Press; 2013.
- [95] Wu JF, Yuan XZ, Martin JJ, Wang HJ, Zhang JJ, Shen J, Wu SH, Merida W. A review of PEM fuel cell durability: degradation mechanisms and mitigation strategies. *J Power Sources* 2008;184:104–19.
- [96] Venkatesan SV, Hannach ME, Holdcroft S, et al. Probing nanoscale membrane degradation cells through electron tomography. *J Membr Sci* 2017;539:138–43.
- [97] Ghassemzadeh LG, Kreuer KD, Maier J, et al. Chemical degradation of Nafion membranes under mimic fuel cell conditions as investigated by solid-state NMR spectroscopy. *J Phys Chem C* 2010;114:14635–45.
- [98] Zaidi S.M.J., Matsuura T. *Polymer membranes for fuel cells*. Springer; 2009.
- [99] Shi S, Weber AZ, Kusoglu A. Structure/property relationship of Nafion XL composite membranes. *J Membr Sci* 2016;516:123–34.
- [100] Kraysberg A, Ein-Eli Y. Review of advanced materials for proton exchange membrane fuel cells. *Energy Fuel* 2014;28:7303–30.
- [101] Mehta V, Cooper JS. Review and analysis of PEM fuel cell design and manufacturing. *J Power Sources* 2003;114:32–53.
- [102] Zamel N. The catalyst layer and its dimensionality - A look into its ingredients and how to characterize their effects. *J Power Sources* 2016;309:141–59.
- [103] Holdcroft S. Fuel Cell Catalyst Layers: a polymer science perspective. *Chem Mater* 2014;26:381–93.
- [104] Hatzell KB, Dixit MB, Berlinger SA, et al. Understanding inks for porous-electrode formation. *J Mater Chem A* 2017;5:20527–33.
- [105] Mishler J, Wang Y, Lujan R, et al. An experimental study of polymer electrolyte fuel cell operation at sub-freezing temperatures. *J Electrochem Soc* 2013;160:F514–21.
- [106] van der Vliet DF, Wang C, Tripkovic D, et al. Mesostuctured thin films as electrocatalysts with tunable composition and surface morphology. *Nat Mater* 2012;11:1051–8.
- [107] Kinoshita K. *Carbon: electrochemical and physicochemical properties*. Wiley; 1988.
- [108] Soboleva T, Zhao XS, Mallek K, et al. On the micro-, meso- and macroscopic structures of polymer electrolyte membrane fuel cell catalyst layers. *ACS Appl Mater Interfaces* 2010;2:375–84.
- [109] Liu YX, Ji CX, Gu WB, et al. Effects of catalyst carbon support on proton conduction and cathode performance in PEM fuel cells. *J Electrochem Soc* 2011;158:B614–21.
- [110] Kim M, Park JN, Kim H, et al. The preparation of Pt/C catalysts using various carbon materials for the cathode of PEMFC. *J Power Sources* 2006;163:93–7.
- [111] Wu G, More KL, Johnston CM, et al. High-performance electrocatalysts for oxygen reduction derived from polyaniline, iron, and cobalt. *Science* 2011;332:443–7.
- [112] Schneider P, Sadeler C, Scherzer AC, et al. Fast and reliable state-of-health model of a PEM cathode catalyst layer. *J Electrochem Soc* 2019;166:F322–33.
- [113] Biesdorf J, Zamel N, Kurz T. Influence of air contaminants on planar, self-breathing hydrogen PEM fuel cells in an outdoor environment. *J Power Sources* 2014;247:339–45.
- [114] Prass S, Friedrich KA, Zamel N. Tolerance and recovery of ultralow-loaded platinum anode electrodes upon carbon monoxide and hydrogen sulfide exposure. *Molecules* 2019;24:3514.
- [115] Wang Y, Feng XH. Analysis of the reaction rates in the cathode electrode of polymer electrolyte fuel cells II. Dual-layer electrodes. *J Electrochem Soc* 2009;156:B403–9.
- [116] Feng XH, Wang Y. Multi-layer configuration for the cathode electrode of polymer electrolyte fuel cell. *Electrochim Acta* 2010;55:4579–86.
- [117] Banham D, Ye SY. Current status and future development of catalyst materials and catalyst layers for proton exchange membrane fuel cells: an industrial perspective. *ACS Energy Lett* 2017;2:629–38.
- [118] Othman R, Dicks AL, Zhu ZH. Non precious metal catalysts for the PEM fuel cell cathode. *Int J Hydrogen Energ* 2012;37:357–72.
- [119] Wang Y, Yu JL, Wu JT, et al. Rapid analysis of platinum and Nafion loadings using laser induced breakdown spectroscopy. *J Electrochem Soc* 2017;164:F1294–F1300.
- [120] Mathias MF, Roth J, Fleming L, et al. *Diffusion media materials and characterisation Handbook of fuel cells-fundamentals, technology and applications*. John Wiley and Sons; 2010.
- [121] Zamel N, Litovsky E, Shakhshir S, et al. Measurement of in-plane thermal conductivity of carbon paper diffusion media in the temperature range of -20 °C to +120 °C. *Appl Energ* 2011;88:3042–50.
- [122] Qi ZG, Kaufman A. Improvement of water management by a microporous sublayer for PEM fuel cells. *J Power Sources* 2002;109:38–46.
- [123] Wargo EA, Schulz VP, Cecen A, et al. Resolving macro- and micro-porous layer interaction in polymer electrolyte fuel cells using focused ion beam and X-ray computed tomography. *Electrochim Acta* 2013;87:201–12.
- [124] Malekian A, Salari S, Stumper J, et al. Effect of compression on pore size distribution and porosity of PEM fuel cell catalyst layers. *Int J Hydrogen Energ* 2019;44:23396–405.
- [125] Weber AZ, Newman J. Effects of microporous layers in polymer electrolyte fuel cells. *J Electrochem Soc* 2005;152:A677–88.
- [126] Alink R, Gerteisen D. Coupling of a continuum fuel cell model with a discrete liquid water percolation model. *Int J Hydrogen Energ* 2014;39:8457–73.
- [127] Deng H, Hou Y, Jiao K. Lattice Boltzmann simulation of liquid water transport inside and at interface of gas diffusion and micro-porous layers of PEM fuel cells. *Int J Heat Mass Tran* 2019;140:1074–90.
- [128] Markotter H, Haussmann J, Alink R, et al. Influence of cracks in the microporous layer on the water distribution in a PEM fuel cell investigated by synchrotron radiography. *Electrochem Commun* 2013;34:22–4.
- [129] Alink R, Gerteisen D. Modeling the liquid water transport in the gas diffusion layer for polymer electrolyte membrane fuel cells using a water path network. *Energies* 2013;6:4508–30.
- [130] Atiyeh HK, Karan K, Peppley B, et al. Experimental investigation of the role of a microporous layer on the water transport and performance of a PEM fuel cell. *J Power Sources* 2007;170:111–21.
- [131] Gostick JT, Ioannidis MA, Fowler MW, et al. On the role of the microporous layer in PEMFC operation. *Electrochem Commun* 2009;11:576–9.
- [132] Cetinbas FC, Ahluwalia RK, Shum AD, et al. Direct simulations of pore-scale water transport through diffusion media. *J Electrochem Soc* 2019;166:F3001.
- [133] Simon C, Kartouzian D, Muller D, et al. Impact of microporous layer pore properties on liquid water transport in PEM fuel cells: carbon black type and perforation. *J Electrochem Soc* 2017;164:F1697–711.
- [134] Nagai Y, Eller J, Hatanaka T, et al. Improving water management in fuel cells through microporous layer modifications: fast operando tomographic imaging of liquid water. *J Power Sources* 2019;435:226809.
- [135] Gao PP, Xie ZY, Wu XB, et al. Development of Ti bipolar plates with carbon/PtFE/TiN composites coating for PEMFCs. *Int J Hydrogen Energ* 2018;43:20947–58.
- [136] de Oliveira MCL, Ett G, Antunes RA. Materials selection for bipolar plates for polymer electrolyte membrane fuel cells using the Ashby approach. *J power sources* 2012;206:3–13.
- [137] Cho SC, Wang Y, Chen KS. Droplet dynamics in a polymer electrolyte fuel cell gas flow channel: forces, deformation, and detachment. I: theoretical and numerical analyses. *J Power Sources* 2012;206:119–28.
- [138] Cho SC, Wang Y, Chen KS. Droplet dynamics in a polymer electrolyte fuel cell gas flow channel: forces, Deformation and detachment. II: comparisons of analytical solution with numerical and experimental results. *J Power Sources* 2012;210:191–7.
- [139] Wang Y. Porous-media flow fields for polymer electrolyte fuel cells II. Analysis of channel two-phase flow. *J Electrochem Soc* 2009;156:B1134–41.
- [140] Wang Y. Porous-media flow fields for polymer electrolyte fuel cells I. Low humidity operation. *J Electrochem Soc* 2009;156:B1124–33.

- [141] Park JE, Hwang W, Lim MS, et al. Achieving breakthrough performance caused by optimized metal foam flow field in fuel cells. *Int J Hydrogen Energy* 2019;44:22074–84.
- [142] Afshari E, Mosharaf-Dehkordi M, Rajabian H. An investigation of the PEM fuel cells performance with partially restricted cathode flow channels and metal foam as a flow distributor. *Energy* 2017;118:705–15.
- [143] Zhang, et al. Optimization of porous media flow field for proton exchange membrane fuel cell using a data-driven surrogate model. Submitted to *Energy Conversion and Management* 2020.
- [144] U.S. DRIVE Fuel Cell Tech Team. DOE Technical Targets for Polymer Electrolyte Membrane Fuel Cell Components. <https://www.energy.gov/eere/fuelcells/doe-technical-targets-polymer-electrolyte-membrane-fuel-cell-components>; 2017.
- [145] Leverett M. Capillary behavior in porous solids. *Transactions of the AIME* 1941;142:152–69.
- [146] Liu XL, Peng FY, Lou GF, et al. Liquid water transport characteristics of porous diffusion media in polymer electrolyte membrane fuel cells: a review. *J Power Sources* 2015;299:85–96.
- [147] Gostick JT, Ioannidis MA, Pritzker MD, et al. Impact of liquid water on reactant mass transfer in PEM fuel cell electrodes. *J Electrochem Soc* 2010;157:B563–71.
- [148] Niu ZQ, Wang Y, Jiao K, et al. Two-phase flow dynamics in the gas diffusion layer of proton exchange membrane fuel cells: volume of fluid modeling and comparison with experiment. *J Electrochem Soc* 2018;165:F613–20.
- [149] Randive P, Dalal A, Mukherjee PP. Probing the influence of superhydrophobicity and mixed wettability on droplet displacement behavior. *Microfluid Nanofluid* 2014;17:657–74.
- [150] Niu ZQ, Bao ZM, Wu JT, et al. Two-phase flow in the mixed-wettability gas diffusion layer of proton exchange membrane fuel cells. *Appl Energy* 2018;232:443–50.
- [151] Niu ZQ, Wu JT, Bao ZM, et al. Two-phase flow and oxygen transport in the perforated gas diffusion layer of proton exchange membrane fuel cell. *Int J Heat Mass Tran* 2019;139:58–68.
- [152] Park J, Oh H, Lee YI, et al. Effect of the pore size variation in the substrate of the gas diffusion layer on water management and fuel cell performance. *Appl Energy* 2016;171:200–12.
- [153] Wang Y, Chen KS. Effect of spatially-varying GDL properties and land compression on water distribution in PEM fuel cells. *J Electrochem Soc* 2011;158:B1292–9.
- [154] Fluckiger R, Marone F, Stapanoni M, et al. Investigation of liquid water in gas diffusion layers of polymer electrolyte fuel cells using X-ray tomographic microscopy. *Electrochim Acta* 2011;56:2254–62.
- [155] Wang Y, Chen KS. Advanced control of liquid water region in diffusion media of polymer electrolyte fuel cells through a dimensionless number. *J Power Sources* 2016;315:224–35.
- [156] Wang CY, Cheng P. Multiphase flow and heat transfer in porous media. *Adv Heat Trans* 1997;30:93–196.
- [157] Ferreira RB, Falcao DS, Oliveira VB, et al. Numerical simulations of two-phase flow in proton exchange membrane fuel cells using the volume of fluid method - A review. *J Power Sources* 2015;277:329–42.
- [158] Song GH, Meng H. Numerical modeling and simulation of PEM fuel cells: progress and perspective. *Acta Mech Sinica-Prc* 2013;29:318–34.
- [159] Gurau V, Mann JA. A critical overview of computational fluid dynamics multiphase models for proton exchange membrane fuel cells. *SIAM J Appl Math* 2009;70:410–54.
- [160] Demuren A, Edwards RL. Modeling proton exchange membrane fuel cells—A Review. In: 50 years of CFD in engineering sciences. Springer; 2020. p. 513–47.
- [161] Berning T, Djilali N. A 3D, multiphase, multicomponent model of the cathode and anode of a PEM fuel cell. *J Electrochem Soc* 2003;150:A1589–98.
- [162] Adroher XC, Wang Y. Ex situ and modeling study of two-phase flow in a single channel of polymer electrolyte membrane fuel cells. *J Power Sources* 2011;196:9544–51.
- [163] Zhang GB, Wu JT, Wang Y, et al. Investigation of current density spatial distribution in PEM fuel cells using a comprehensively validated multi-phase non-isothermal model. *Int J Heat Mass Tran* 2020;150:119294.
- [164] Qin CZ, Rensink D, Fell S, et al. Two-phase flow modeling for the cathode side of a polymer electrolyte fuel cell. *J Power Sources* 2012;197:136–44.
- [165] Wang Y, Cho SC, Thiedmann R, et al. Stochastic modeling and direct simulation of the diffusion media for polymer electrolyte fuel cells. *Int J Heat Mass Tran* 2010;53:1128–38.
- [166] Fadzillah DM, Rosli MI, Talib MZM, et al. Review on microstructure modelling of a gas diffusion layer for proton exchange membrane fuel cells. *Renew Sust Energy Rev* 2017;77:1001–9.
- [167] Zhenyuk IV, Parkinson DY, Connolly LG, et al. Gas-diffusion-layer structural properties under compression via X-ray tomography. *J Power Sources* 2016;328:364–76.
- [168] Fishman Z, Hinebaugh J, Bazylak A. Microscale tomography investigations of heterogeneous porosity distributions of PEMFC GDLs. *J Electrochem Soc* 2010;157:B1643–50.
- [169] Alrwashdeh SS, Manke I, Markotter H, et al. Neutron radiographic in operando investigation of water transport in polymer electrolyte membrane fuel cells with channel barriers. *Energy Convers Manage* 2017;148:604–10.
- [170] Mishler J, Wang Y, Mukundan R, et al. Probing the water content in polymer electrolyte fuel cells using neutron radiography. *Electrochim Acta* 2012;75:1–10.
- [171] Markotter H, Manke I, Kuhn R, et al. Neutron tomographic investigations of water distributions in polymer electrolyte membrane fuel cell stacks. *J Power Sources* 2012;219:120–5.
- [172] Dierolf M, Menzel A, Thibault P, et al. Ptychographic X-ray computed tomography at the nanoscale. *Nature* 2010;467:436–82.
- [173] Ge N, Chevalier S, Lee J, et al. Non-isothermal two-phase transport in a polymer electrolyte membrane fuel cell with crack-free microporous layers. *Int J Heat Mass Tran* 2017;107:418–31.
- [174] Raissi M, Yazdani A, Karniadakis GE. Hidden fluid mechanics: learning velocity and pressure fields from flow visualizations. *Science* 2020;367:1026–30.
- [175] Benner J, Mortazavi M, Santamaria AD. Numerical simulation of droplet emergence and growth from gas diffusion layers (GDLs) in proton exchange membrane (PEM) fuel cell flow channels. ASME 2018 international mechanical engineering congress and exposition. American Society of Mechanical Engineers Digital Collection; 2018.
- [176] Verma A, Pitchumani R. Effects of operating parameters on the transient response of proton exchange membrane fuel cells subject to load changes. *Int J Hydrogen Energy* 2014;39:19024–38.
- [177] Wang Y, Wang CY. Dynamics of polymer electrolyte fuel cells undergoing load changes. *Electrochim Acta* 2006;51:3924–33.
- [178] Wang Y, Wang CY. Transient analysis of polymer electrolyte fuel cells. *Electrochim Acta* 2005;50:1307–15.
- [179] Arias IKP, Trinke P, Hanke-Rauschenbach R, et al. Understanding PEM fuel cell dynamics: the reversal curve. *Int J Hydrogen Energy* 2017;42:15818–27.
- [180] Rasheed RKA, Ehteshami SMM, Chan SH. Analytical modelling of boiling phase change phenomenon in high-temperature proton exchange membrane fuel cells during warm-up process. *Int J Hydrogen Energy* 2014;39:2246–60.
- [181] Wang Y, Wang CY. Two-phase transients of polymer electrolyte fuel cells. *J Electrochem Soc* 2007;154:B636–43.
- [182] Klages M, Enz S, Markotter H, et al. Investigations on dynamic water transport characteristics in flow field channels using neutron imaging techniques. *J Power Sources* 2013;239:596–603.
- [183] Schneider IA, von Dahlen S, Bayer MH, et al. Local transients of flooding and current in channel and land areas of a polymer electrolyte fuel cell. *J Phys Chem C* 2010;114:11998–2002.
- [184] Cho J, Park J, Oh H, et al. Analysis of the transient response and durability characteristics of a proton exchange membrane fuel cell with different micro-porous layer penetration thicknesses. *Appl Energy* 2013;111:300–9.
- [185] Cho J, Oh H, Park J, et al. Effect of the micro porous layer design on the dynamic performance of a proton exchange membrane fuel cell. *Int J Hydrogen Energy* 2014;39:459–68.
- [186] Meng H, Ruan B. Numerical studies of cold-start phenomena in PEM fuel cells: a review. *Int J Energy Res* 2011;35:2–14.
- [187] Wan Z, Chang H, Shu S, et al. A review on cold start of proton exchange membrane fuel cells. *Energies* 2014;7:3179–203.
- [188] Luo YQ, Jiao K. Cold start of proton exchange membrane fuel cell. *Prog Energy Combust* 2018;64:29–61.
- [189] Wang Y. Analysis of the key parameters in the cold start of polymer electrolyte fuel cells. *J Electrochem Soc* 2007;154:B1041–8.
- [190] Ko J, Kim WG, Lim YD, et al. Improving the cold-start capability of polymer electrolyte fuel cells (PEFCs) by using a dual-function micro-porous layer (MPL): numerical simulations. *Int J Hydrogen Energy* 2013;38:652–9.
- [191] Wang Y, Mukherjee PP, Mishler J, et al. Cold start of polymer electrolyte fuel cells: three-stage startup characterization. *Electrochim Acta* 2010;55:2636–44.
- [192] Ko J, Ju H. Comparison of numerical simulation results and experimental data during cold-start of polymer electrolyte fuel cells. *Appl Energy* 2012;94:364–374.
- [193] Ko J, Ju H. Effects of cathode catalyst layer design parameters on cold start behavior of polymer electrolyte fuel cells (PEFCs). *Int J Hydrogen Energy* 2013;38:682–91.
- [194] Santamaria AD, Bachman J, Park JW. Cold-start of parallel and interdigitated flow-field polymer electrolyte membrane fuel cell. *Electrochim Acta* 2013;107:327–38.
- [195] Siegwart M, Huang F, Cochet M, et al. Spatially resolved analysis of freezing during isothermal PEFC cold starts with time-of-flight neutron imaging. *J Electrochem Soc* 2020;167:064510.
- [196] Wang Y. Modeling discharge deposit formation and its effect on lithium-air battery performance. *Electrochim Acta* 2012;75:239–46.
- [197] Yuan JL, Yu JS, Sundén B. Review on mechanisms and continuum models of multi-phase transport phenomena in porous structures of non-aqueous Li-Air batteries. *J Power Sources* 2015;278:352–69.
- [198] Mishler J, Wang Y, Mukherjee PP, et al. Subfreezing operation of polymer electrolyte fuel cells: ice formation and cell performance loss. *Electrochim Acta* 2012;65:127–33.
- [199] Yuan H, Read JA, Wang Y. Capacity loss of non-aqueous Li-air battery due to insoluble product formation: approximate solution and experimental validation. *Mater Today Energy* 2019:14100360.
- [200] Wang Y, Yuan H. Discharge precipitate's impact in Li-air battery: comparison of experiment and model predictions. *J Electrochem Soc* 2017;164:A2283–9.
- [201] Du Q, Jia B, Luo YQ, et al. Maximum power cold start mode of proton exchange membrane fuel cell. *Int J Hydrogen Energy* 2014;39:8390–400.
- [202] Macauley N, Lujan RW, Spornjak D, et al. Durability of polymer electrolyte membrane fuel cells operated at subfreezing temperatures. *J Electrochem Soc* 2016;163:F1317–29.
- [203] U.S. DRIVE Fuel Cell Tech Team. Cell component accelerated stress test and polarization curve protocols for PEM fuel cells. [https://www.energy.gov/eere/fuelcells/durability-working-group#accelerated\\_stress\\_tests](https://www.energy.gov/eere/fuelcells/durability-working-group#accelerated_stress_tests); 2013.
- [204] de Bruijn FA, Dam VAT, Janssen GJM. Durability and degradation issues of PEM fuel cell components. *Fuel Cells* 2008;8:3–22.
- [205] Knights SD, Colbow KM, St-Pierre J, et al. Aging mechanisms and lifetime of PEFC and DMFC. *J Power Sources* 2004;127:127–34.
- [206] Curtin DE, Lousenberg RD, Henry TJ, et al. Advanced materials for improved PEMFC performance and life. *J Power Sources* 2004;131:41–8.
- [207] Pianca M, Barchiesi E, Esposto G, et al. End groups in fluoropolymers. *J Fluor Chem* 1999;95:71–84.

- [208] Collier A, Wang HJ, Yuan XZ, et al. Degradation of polymer electrolyte membranes. *Int J Hydrogen Energy* 2006;31:1838–54.
- [209] Schiraldi DA. Perfluorinated polymer electrolyte membrane durability. *Polym Rev* 2006;46:315–27.
- [210] Vielstich W, Arnold L, Gasteiger HA. *Handbook of fuel cells: fundamentals, technology, applications*. John Wiley and Sons; 2003.
- [211] Zaton M, Roziere J, Jones DJ. Current understanding of chemical degradation mechanisms of perfluorosulfonic acid membranes and their mitigation strategies: a review. *Sustain Energy Fuels* 2017;1:409–38.
- [212] Healy J, Hayden C, Xie T, et al. Aspects of the chemical degradation of PFSA ionomers used in PEM fuel cells. *Fuel Cells* 2005;5:302–8.
- [213] Tsuneda T, Singh RK, Iiyama A, et al. Theoretical investigation of the H<sub>2</sub>O<sub>2</sub>-induced degradation mechanism of hydrated nafion membrane via ether-linkage dissociation. *ACS Omega* 2017;2:4053–64.
- [214] Gubler L. Polymer design strategies for radiation-grafted fuel cell membranes. *Adv Energy Mater* 2014;4:1300827.
- [215] Haber JWF. The catalytic decomposition of hydrogen peroxide by iron salts. *P Roy Soc A* 1934;147:332–51.
- [216] Shao-Horn Y, Sheng WC, Chen S, et al. Instability of supported platinum nanoparticles in low-temperature fuel cells. *Top Catal* 2007;46:285–305.
- [217] Borup RL, Kusoglu A, Neyerlin KC, et al. Recent developments in catalyst-related PEM fuel cell durability. *Curr Opin Electrochem* 2020;21:192–200.
- [218] Topalov AA, Cherevko S, Zeradjanin AR, et al. Towards a comprehensive understanding of platinum dissolution in acidic media. *Chem Sci* 2014;5:631–8.
- [219] Buchi FN, Inaba M, Schmidt TJ. *Polymer electrolyte fuel cell durability*. Springer; 2009.
- [220] Borup RL, Weber AZ. FC-PAD: fuel cell performance and durability consortium. In: DOE Hydrogen and Fuel Cells Program. *2018 Annual Merit Review Proceedings*; 2018.
- [221] Ahmad T, Chen H. A review on machine learning forecasting growth trends and their real-time applications in different energy systems. *Sustain Cities Soc* 2020;54:102010.
- [222] Barrett DH, Aderemi H. Artificial intelligence and machine learning for targeted energy storage solutions. *Curr Opin Electrochem* 2020;21:160–6.
- [223] Salcedo-Sanz S, Cornejo-Bueno L, Prieto L, et al. Feature selection in machine learning prediction systems for renewable energy applications. *Renew Sust Energy Rev* 2018;90:728–41.
- [224] Butler KT, Davies DW, Cartwright H, et al. Machine learning for molecular and materials science. *Nature* 2018;559:547–55.
- [225] Hosmer Jr DW, Lemeshow S. *Applied logistic regression*. Wiley; 2000.
- [226] Breiman L, Friedman J, Stone C, et al. *Classification and regression trees (Wadsworth statistics/probability)*. 1st ed. Chapman and Hall/CRC; 1984.
- [227] Cortes C, Vapnik V. Support-vector networks. *Mach Learn* 1995;20:273–97.
- [228] Scikit-learn. <https://scikit-learn.org/>.
- [229] Rumelhart DE, Hinton GE, Williams RJ. Learning internal representations by back-propagating errors. *Nature* 1986;323(99):533–6.
- [230] Hinton GE, Dayan P, Frey BJ, et al. The wake-sleep algorithm for unsupervised neural networks. *Science* 1995;268:1158–61.
- [231] Hinton GE, Salakhutdinov RR. Reducing the dimensionality of data with neural networks. *Science* 2006;313:504–7.
- [232] LeCun Y, Bengio Y, Hinton G, et al. Deep learning. *Nature* 2015;521:436–44.
- [233] Mehrpooya M, Ghorbani B, Jafari B, et al. Modeling of a single cell micro proton exchange membrane fuel cell by a new hybrid neural network method. *Therm Sci Eng Prog* 2018;7:8–19.
- [234] Han IS, Chung CB. Performance prediction and analysis of a PEM fuel cell operating on pure oxygen using data-driven models: a comparison of artificial neural network and support vector machine. *Int J Hydrogen Energy* 2016;41:10202–11.
- [235] Kheirandish A, Motlagh F, Shafiabady N, et al. Dynamic modelling of PEM fuel cell of power electric bicycle system. *Int J Hydrogen Energy* 2016;41:9585–94.
- [236] Kheirandish A, Shafiabady N, Dahari M, et al. Modeling of commercial proton exchange membrane fuel cell using support vector machine. *Int J Hydrogen Energy* 2016;41:11351–8.
- [237] Wu HW. A review of recent development: transport and performance modeling of PEM fuel cells. *Appl Energy* 2016;165:81–106.
- [238] Kheirandish A, Motlagh F, Shafiabady N, et al. Dynamic fuzzy cognitive network approach for modelling and control of PEM fuel cell for power electric bicycle system. *Appl Energy* 2017;202:20–31.
- [239] Chavez-Ramirez AU, Munoz-Guerrero R, Duron-Torres SM, et al. High power fuel cell simulator based on artificial neural network. *Int J Hydrogen Energy* 2010;35:12125–33.
- [240] Bicer Y, Dincer I, Aydin M. Maximizing performance of fuel cell using artificial neural network approach for smart grid applications. *Energy* 2016;116:1205–17.
- [241] Zhang GB, Yuan H, Wang Y, et al. Three-dimensional simulation of a new cooling strategy for proton exchange membrane fuel cell stack using a non-isothermal multiphase model. *Appl Energy* 2019;255:113865.
- [242] Wang BW, Xie B, Xuan J, et al. AI-based optimization of PEM fuel cell catalyst layers for maximum power density via data-driven surrogate modeling. *Energy Convers Manage* 2020;205:112460.
- [243] Khajeh-Hosseini-Dalasm N, Ahadian S, Fushinobu K, et al. Prediction and analysis of the cathode catalyst layer performance of proton exchange membrane fuel cells using artificial neural network and statistical methods. *J Power Sources* 2011;196:3750–6.
- [244] Wang B, Zhang G, Wang H, et al. Multi-physics-resolved digital twinning of proton exchange membrane fuel cells with a data-driven surrogate model. *Energy and AI* 2020;1:100004.
- [245] Fanourgakis GS, Gkagkas K, Tylianakis E, et al. A universal machine learning algorithm for large-scale screening of materials. *J Am Chem Soc* 2020;142:3814–22.
- [246] Krishnamurthy D, Weiland H, Farimani AB, et al. Machine learning based approaches to accelerate energy materials discovery and optimization. *ACS Energy Lett* 2019;4:187–91.
- [247] Gu GH, Noh J, Kim I, et al. Machine learning for renewable energy materials. *J Mater Chem A* 2019;7:17096–117.
- [248] Zhu XR, Yan JX, Gu M, et al. Activity origin and design principles for oxygen reduction on dual-metal-site catalysts: a combined density functional theory and machine learning study. *J Phys Chem Lett* 2019;10:7760–6.
- [249] Fujimura K, Seko A, Koyama Y, et al. Accelerated materials design of lithium superionic conductors based on first-principles calculations and machine learning algorithms. *Adv Energy Mater* 2013;3:980–5.
- [250] Fouquet N, Doulet C, Nouillant C, et al. Model based PEM fuel cell state-of-health monitoring via ac impedance measurements. *J Power Sources* 2006;159:905–13.
- [251] Sutharssan T, Montalvao D, Chen YK, et al. A review on prognostics and health monitoring of proton exchange membrane fuel cell. *Renew Sust Energy Rev* 2017;75:440–50.
- [252] Mao L, Jackson LM. Comparative study on prediction of fuel cell performance using machine learning approaches. *Proc Int Multi Conf Eng Comp Scientists* 2016.
- [253] Ma R, Yang T, Breaz E, et al. Data-driven proton exchange membrane fuel cell degradation prediction through deep learning method. *Appl Energy* 2018;231:102–15.
- [254] Javed K, Gouriveau R, Zerhouni N, et al. Data-driven prognostics of proton exchange membrane fuel cell stack with constraint based summation-wavelet extreme learning machine. In: 6th Int Conf Fundamentals Dev Fuel Cells (FDFC); 2015. p. 1–8.
- [255] Ma R, Li ZL, Breaz E, et al. Data-fusion prognostics of proton exchange membrane fuel cell degradation. *IEEE T Ind Appl* 2019;55:4321–31.
- [256] Zhou DM, Gao F, Breaz E, et al. Degradation prediction of PEM fuel cell using a moving window based hybrid prognostic approach. *Energy* 2017;138:1175–86.
- [257] Chen K, Laghrouche S, Djerdir A. Degradation prediction of proton exchange membrane fuel cell based on grey neural network model and particle swarm optimization. *Energy Convers Manage* 2019;195:810–18.
- [258] Onanena R, Oukhellou L, Come EE, et al. Fuel cell health monitoring using self organizing maps. *Chem Eng Trans* 2013;33:1021–6.
- [259] Mayur M, Gerard M, Schott P, et al. Lifetime prediction of a polymer electrolyte membrane fuel cell under automotive load cycling using a physically-based catalyst degradation model. *Energies* 2018;11:2054.
- [260] Liu JW, Li Q, Han Y, et al. PEMFC residual life prediction using sparse autoencoder-based deep neural network. *IEEE T Transp Electr* 2019;5:1279–93.
- [261] Morando S, Jemei S, Hissel D, et al. Proton exchange membrane fuel cell ageing forecasting algorithm based on Echo State Network. *Int J Hydrogen Energy* 2017;42:1472–80.
- [262] Silva RE, Gouriveau R, Jemei S, et al. Proton exchange membrane fuel cell degradation prediction based on Adaptive Neuro-Fuzzy Inference Systems. *Int J Hydrogen Energy* 2014;39:11128–44.
- [263] Javed K, Gouriveau R, Zerhouni N, et al. Enabling health monitoring approach based on vibration data for accurate prognostics. *IEEE T Ind Electron* 2015;62:647–56.
- [264] Morando S, Jemei S, Gouriveau R, et al. Fuel cells prognostics using Echo State Network. *IEEE Ind Elec* 2013:1632–7.
- [265] Jouin F, Gouriveau R, Hissel D, et al. Prognostics of PEM fuel cell in a particle filtering framework. *Int J Hydrogen Energy* 2014;39:481–94.
- [266] Ibrahim M, Steiner NY, Jemei S, et al. Wavelet-based approach for online fuel cell remaining useful lifetime prediction. *IEEE T Ind Electron* 2016;63:5057–68.